Electro-hydrostatic Actuator Fault Detection and Diagnosis

Electro-hydrostatic Actuator Fault Detection and Diagnosis

By

Yu Song, B.ENG

A Thesis
Submitted to the School of
Graduate Studies in Partial Fulfilment of the
Requirements for the Degree of Master of Applied Science in
the Department of Mechanical Engineering

Master of Applied Science (Mechanical Engineering)

McMaster University

Hamilton, Ontario

TITLE: Electro-hydrostatic Actuator Fault Detection and Diagnosis

AUTHOR: Yu Song, B.ENG (McMaster University)

SUPERVISOR: Dr. Saeid R. Habibi

NUMBER OF PAGES: xvii, 158

Abstract

As a compact, robust, and reliable power distribution method, hydraulic systems have been used for flight surface control for decades. Electro-hydrostatic Actuator (EHA) is increasingly replacing the conventional valve-controlled system for better performance, lighter weight and higher energy efficiency. The EHA is increasingly being used for flight control. As such its reliability is thereby critical important for flight safety. This research focuses on fault detection and diagnosis (FDD) for the EHA to enable predictive unscheduled maintenance when fault detected at its inception.

An EHA prototype previously built at McMaster University is studied in this research and modified to physically simulate two faults conditions pertaining to leakage and friction. Nine different working conditions including normal running and eight fault conditions are simulated. Physical model has been derived mathematically capable of numerically simulating the fault conditions. Furthermore, for comparison, parametric model was obtained through system identification for each fault condition. This comparison revealed that parametric models are not suitable for fault detection and diagnosis due to the computation complexity.

The FDD approach in this research uses model-based state estimation using filters. The filter based combined with the Interacting Multiple Model fault detection and diagnosis algorithm is introduced. Based on this algorithm, three FDD strategies are developed using a combination of the Extended Kalman Filter and IMM (IMM-EKF), the Smooth Variable Structure Filter with Varying Boundary and IMM (IMM-SVSF (VBL)), and the Smooth Variable Structure Filter with Fixed Boundary and IMM (IMM-SVSF (FBL)). All the three FDD strategies were implemented on the EHA prototype. Based on the results, the IMM-SVSF (VBL) provided the best performance. It detected and diagnosed faults correctly at high mode probabilities with excellent robustness to modeling uncertainties. It also was able to detect slow growing leakage fault, and predicted the changing trend of fault conditions.

Nomenclature

A_{sys}	System model
μ_i	Mode probability
μ_ij	Mixing probability
$A_{sys,max}$	Maximum error of the system model
B_{sys}	Input model
$B_{sys,max}$	Maximum error of the input model
C_{sys}	Measurement model
$d(k)$	Unknown input in Unknown Input Observer (UIO)
E	Estimation error vector
E_z	Measurement error vector
E	Unknown input matrix in UIO
F	Unknown fault matrix in UIO
f	Nonlinear system model
F_{sys}	Linearized system model
G	UIO design matrix
H	UIO design matrix
h	Nonlinear measurement model
H_{sys}	Linearized measurement model
$H_{sys,max}$	Maximum error of the measurement model
I	Identity matrix
J	UIO design matrix
k	k^{th} moment
K^{KF}	Kalman filter gain
K^{SVSF}	Smooth variable structure filter gain
KF	Kalman filter
L	Luenbeger observer design matrix
L_1	UIO design matrix
L_2	UIO design matrix

P	State error covariance
$p(k)$	Unknown fault in UIO
P_{0j}	Initial state error covariance
p_{ij}	Switching probability
Q	System noise covariance
r	Residual
R	Measurement noise covariance
S	Measurement error covariance
sat	Saturation function
sgn	Sign function
$SVSF$	Smooth variable structure filter
T_{UIO}	UIO design matrix
u	Input
UIO	Unknown Input Observer
v	measurement noise
w	System noise
x	System state
X	System state vector
x_0	State observation of UIO
X_{0j}	Initial state estimation vector
$\hat{X}$	State estimation vector
z	Measurement
Z	Measurement vector
$\hat{Z}$	Measurement estimation vector
γ	Memory convergence rate
Λ	Likely hood
ψ	Smooth boundary layer width
Q_{leak}	Leakage volumetric flow rate (m^3/s)
A	Effective piston area (m^2)
F_f	Friction force (N)

ΔP	Differential pressure (Pa)
D_p	Volumetric displacement (m^3/rad)
ω_p	Motor angular velocity (rad/s)
ξ	Pump cross-port leakage coefficient ($m^3/s/Pa$)
C_{ep}	Pump external leakage coefficient ($m^3/s/Pa$)
B	Effective bulk modulus (Pa)
V_a	Fluid volume associated with the inlet (m^3)
V_b	Fluid volume associated with the outlet (m^3)
Q_i	Flow rate at position I (m^3/s)
L_{in}	Internal leakage coefficient ($m^3/s/Pa$)
L_{out}	External leakage coefficient ($m^3/s/Pa$)
P_i	Pressure at position i (Pa)
V_0	Nominal volume of each EHA chamber (m^3)
L_t	Lump sum leakage coefficient ($m^3/s/Pa$)
Q_{L0}	Leakage offset (m^3/s)
a_1	Friction coefficient (Ns^2/m^2)
a_2	Friction coefficient (Ns/m)
a_3	Friction coefficient (N)
T	Sampling time (s)
M	Moving mass (kg)

Table of content

Contents

List of figures

List of tables

1 Introduction

Faults can be defined as abnormal events which impact the system's performance and dynamics when they occur. A fault may lead to control difficulties or even a catastrophic failure. Due to increasing demand for greater safety and reliability, a great deal of research is being conducted on fault detection and diagnosis. Fault detection and diagnosis (FDD) algorithms range in complexity from simple visual inspections to automatic model-based prognosis.

In this research, the fault detection and diagnosis on a high performance hydraulic actuating system referred as the Electro-hydrostatic Actuator (EHA) is investigated. As a closed-loop hydrostatic system, an EHA consists of a servo-motor, a bi-directional gear pump, a symmetrical actuator, connecting tubes and safety circuits. Compared to conventional centralized open circuit systems, they achieve higher energy efficiencies and have provided in up to 15% in weight savings [**1**]. EHAs are therefore increasingly being used, especially in aerospace industry for flight surface control, as they are overall lighter and able to offer better efficiency.

A hydraulic power device, such as EHA, uses high pressurized fluid and therefore can be dangerous when faults appear. Some of the common failures found in a hydraulic system are listed in Table 1-1 [**2**]. In the EHA, faults commonly cause the effect of leakage and friction. As the EHA is a device implemented for flight control, its reliability is critical for flight safety. Failure of the EHA can be catastrophic and resulting in loss of lives. This research focuses on fault detection and diagnosis for the EHA based on the changes of the leakage and friction coefficients. With an early detection and diagnosis of faults, the reliability of the EHA can be improved.

Table 1-1: Common failures found in hydraulic system. (Adapted from [2])

Feature of fluid power	Condition for failure	Failure Characteristics
Fluid pressure	Excessively high	Hose / Tubing / Pipes burst
		Wear in components such as pumps
	Excessively low	Cavitation and erosion
		Leaking seals
Fluid level	Low	Overheating and cessation of operation
Flow forces in valves	High / Concentrated	Jet erosion of spools and valves
Flow and pressure pules	Resonant	Fatigue
Filtration	Clogged or blocked with contaminant	Cavitation, erosion
		Filter bursts, hose burst, back pressure
Fluid / Containment material	Incompatible	Swelling of seals and corrosion of surfaces
Fluid borne contamination	High particulate concentration in fluid	Wear in sliding parts
		Blockage of ports
	Chemicals	Corrosion
Circuit design	Load excessive	Cracks and breakage

The FDD strategies developed in this research were tested on an EHA prototype built at McMaster [**3**] and is shown in Figure 1-1.

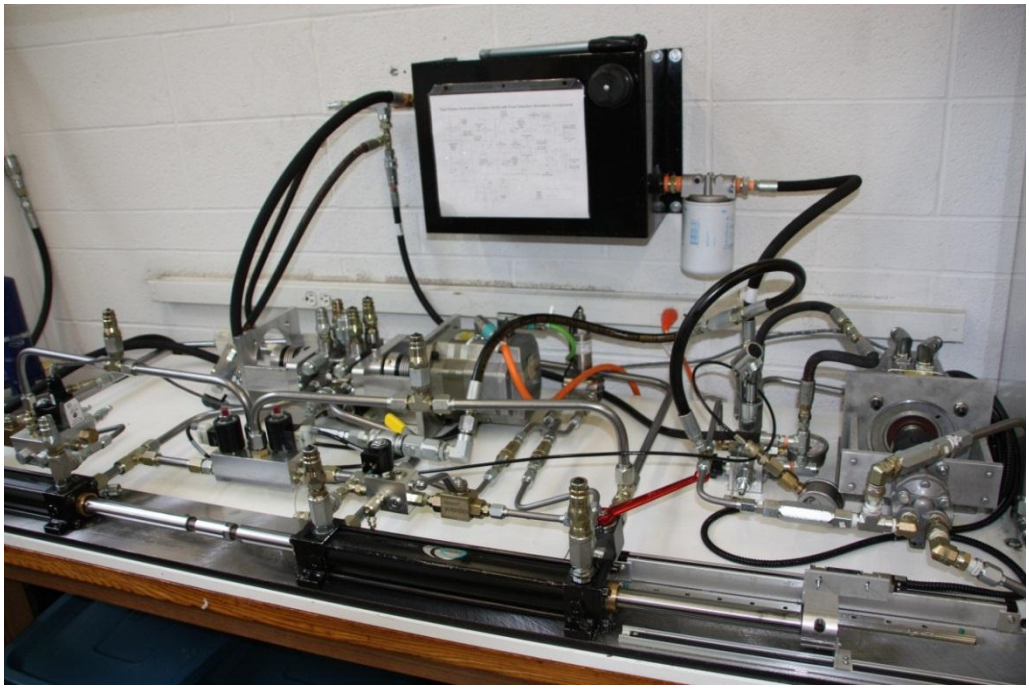

Figure 1-1: Electro Hydrostatic Actuator prototype

Matlab was used in this research for control, model validation, signal processing, data analysis, and implementation of fault detection and diagnosis on an EHA prototype.

1.1 Research objective

The research objectives were to develop a fault detection and diagnosis system for application on the EHA system. In order to achieve this goal, the research objectives were summarized as follows:

- To physically simulate varying leakage and friction faults on the EHA prototype.
- To develop a nonlinear model for the EHA, capable of accurately predicting the EHA's operation, under normal as well as different fault conditions (involving leakage and friction faults).
- To apply estimation techniques for parameter tracking.
- To implement a fault detection and identification strategy on the EHA prototype.

1.2 Thesis outline

The thesis is organized as follows:

Chapter 2 investigates the fault detection and diagnosis algorithms found in the literature; including visual inspections, observer-based approaches, and estimation methods. The estimation techniques considered involve the popular Kalman filter (KF) and the smooth variable structure filter (SVSF). This Chapter also introduces the Interacting Multiple Model concept and its application in fault detection and diagnosis.

Chapter 3 discusses the fault detection and diagnosis (FDD) strategies applied in this research, and presents their formulation.

Chapter 4 discusses hydrostatic actuation system and McMaster's EHA prototype. The instrumentation of the EHA prototype is described in detail. The mechanism for physically inducing fault conditions is explained.

Chapter 5 provides the derivation of a physical model capable of numerically simulating the EHA's operation under normal and various fault conditions. For comparison, parametric models were also obtained for each fault condition considered in this research through system identification. An EHA model library was obtained with validated models.

Chapter 6 presents experimental results from applications of the fault detection and diagnosis strategies, as applied on the EHA prototype. Conclusions and the main findings are summarized in Chapter 7.

2 Literature Review – Fault detection

A fault can be defined as an abnormal event which changes the system dynamics. A fault may lead to difficulties associated with control, performance degradation, or even catastrophic failure. Due to increasing demand for greater fault tolerance, higher performance and more reliable systems, great deal of research has been conducted on fault detection.

2.1 Visual Inspection

Visual inspection is perhaps the simplest fault detection approach [**4**]. For example, a detection solution offered by Advanced Engineering Ltd, is a fluorescent additive [Oil-Glo] that is added to hydraulic oil [**5**]. Since the additive is UV light sensitive, the leakage can be seen with a 100W inspection lamp. As an easy implementation method, fluorescent additives can be used for detecting leakage accurately with low cost.

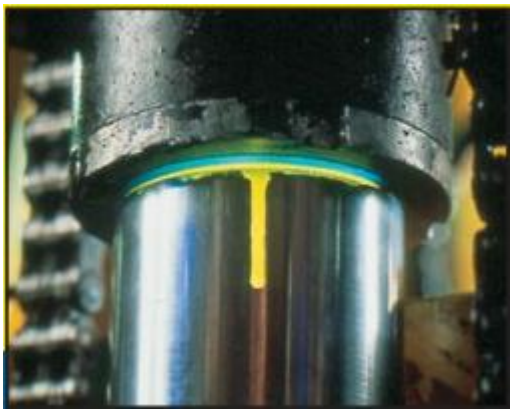

Figure 2-1: Advanced Engineering Ltd. Oil-Glo method of leakage detection (Taken from [5])

Visual inspection is also used for determining the contamination in hydraulic systems, but with limited accuracy. As a more appropriate approach, electronic particle-counter provides greater accuracy. These project a light beam on fluid passing through a transparent tube. A photocell senses the light density and an electronic counter counts light interruptions to quantify contamination [**6**].

Visual inspection is simple and low cost. However, it can only detect visible faults such as external leakage and obvious contamination. Besides, visual inspection of external leakage, such as fluorescent additives, relies on human operator, and it becomes increasingly difficult with complex devices. Human operators can make erroneous decisions and take actions which could make matters even worse [**7**]. Therefore this raises a challenge for control engineers to develop automated fault detection algorithms and integrate these with the control systems.

2.2 Quantitative Model-based Fault Detection and Diagnosis

Faults in systems change their dynamics and model. Given an accurate baseline model, the system state trajectory can be predicted. A fault condition changes the state trajectory and causes discrepancy between predictions and observations. This enables the detection of the fault. Fault detection using predictive models is classified under quantitative model-based methods [**7**].

The basic concept of model-based fault detection is to predict system output and generate a residual based on the difference between the predicted and the measured output. Fault is detected if the residual exceeds a predefined threshold. In practical implementations, uncertainties in the model and the measurement influence the fault detection performance severely and can cause false alarms or leave faults undetected. Therefore a main requirement of model-based fault detection is generating a residual that is stable and able to deal with uncertainties.

2.3 Observer Based Approach

As one of the most common ways of generating a residual, the observer was firstly designed to reconstruct missing-state-variables for control purpose. David G. Luenberger introduced a commonly used basic observer which was later named after him as Luenberger observer [**8**] [**9**].

The Luenberger observer assumes a linear time invariant system described by the following equations:

$$x(k+1) = A_{sys}x(k) + B_{sys}u(k)$$
$$z(k) = C_{sys}x(k) \tag{2-1}$$

where x denotes the system states, u is the input and z is the measurements; A_{sys}, B_{sys} and C_{sys} form the state space model. The Luenberger observer is formulated as:

$$\hat{x}(k+1) = A_{sys}\hat{x}(k) + L[z(k) - \hat{z}(k)] + B_{sys}u(k)$$
$$\hat{z}(k) = C_{sys}\hat{x}(k) \tag{2-2}$$

where $\hat{x}\ and\ \hat{z}$ denote the observer's estimation of the system state vector and the output. L is a gain matrix. The observer has the estimation error calculated as:

$$e(k+1) = x(k+1) - \hat{x}(k+1) \tag{2-3}$$

Substituting Eqn (2-1) and (2-2) to (2-3), and rearranging yields:

$$e(k+1) = \left(A_{sys} - LC_{sys}\right)e(k) \tag{2-4}$$

The Luenberger observer is stable if the estimation error $e(k)$ tends to zero as k approaches infinity. The observer is stable when $A - LC$ has all of its eigenvalues inside the unit circle.

Based on the observer structure developed by Luenberger, a number of approaches have been designed to reconstruct the state vector in a system with uncertainties. These include the Interval Observers and the Sliding Mode Observers. The observer is able to predict the system state that in turn is used to generate a residual. One of the most common ways of generating a residual is by using the Unknown Input Observer (UIO). The UIO treats the model and the measurement uncertainties as unknown inputs. UIO was designed to decouple the effects of the faults from the unknown inputs, so that faults can be detected. Assume a system described by the following discrete state-space equations.

$$x(k+1) = A_{sys}x(k) + B_{sys}u(k) + Ed(k) + Fp(k) \tag{2-5}$$

$$z(k) = C_{sys}x(k) \tag{2-6}$$

where, the input $u(k)$ and the measurement $z(k)$ are measurable. $x(k)$ denotes the system states. $d(k)$ and $p(k)$ stand for the unknown input and fault respectively. An Unknown Input Observer (UIO) is formulated with a modified model format as

$$x_0(k+1) = Hx_0(k) + Ju(k) + Gz(k) \tag{2-7}$$

where x_0 denotes the observer estimates of the system states which are formulated as:

$$x_0(k) = Tx(k) \tag{2-8}$$

The design of UIO involves choices of $T, H, J, and\ G$. The estimation error e and residual r are calculated as:

$$e(k+1) = x_0(k+1) - Tx(k+1) \tag{2-9}$$

$$r(t) = L_1x_0(k) + L_2z(k) \tag{2-10}$$

Substituting Eqn (2-5) and (2-7) into (2-9) yields,

$$\begin{aligned} e(k+1) = Hx_0(k) + \left(J - TB_{sys}\right)u(k) + Gz(k) - TA_{sys}x(k) \\ - TEd(k) - TFp(k) \end{aligned} \tag{2-11}$$

In order to decouple the unknown input which involves both the model and the measurement uncertainties, T is chosen such that $TE = 0$. The error in the estimation should be independent of the input $u(t)$. Matrix J is thereby chosen such that $J = TB$. Substituting $TE = 0, J = TB$ and Eqn (2-6) in (2-11) yields,

$$e(k+1) = Hx_0(k) + (GC_{sys} - TA_{sys})x(k) - TFp(k) \tag{2-12}$$

By choosing matrix G so that $GC_{sys} - TA_{sys} = -HT$, Eqn (2-12) yields,

$$e(k+1) = He(k) - TFp(k) \tag{2-13}$$

Substituting Eqn (2-6) in (2-10) yields:

$$r(k) = L_1 x_0(k) + L_2 C_{sys} x(k) \tag{2-14}$$

Let L_1, L_2 be chosen so that $-L_1 T = L_2 C_{sys}$. Eqn (2-14) can be rearranged as:

$$r(k) = L_1 x_0(k) - L_1 T x(k) = L_1 e(k) \tag{2-15}$$

When the system is operating without fault, $p(t) = 0$ and estimation becomes:

$$e(k+1) = He(k) \tag{2-16}$$

Choosing matrix H with absolute eigenvalues smaller than one yields:

$$\lim_{t \to \infty} e(t) = 0 \tag{2-17}$$

$$\lim_{t \to \infty} r(t) = 0$$

As a result, UIO is able to estimate the system states and track the process regardless of the unknown input (model and measurement uncertainties). With a system fault occurring, the estimation error is formulated as (2-13) and both the estimation error and the residual values carry the signature of fault $p(t)$. Details about generating the residual using UIO are provided in [**7**] [**10**].

The next step in fault detection is decision making based on the generated residuals. Ideally, the residual remains zero under normal operating conditions and perfect decoupling of system uncertainties ($T, H, J, G, L_1 \; and \; L_2$ are carefully chosen) Fault can thereby be detected with nonzero residuals. In fact, perfect decoupling of unknown input is not always achievable in complex systems. The residual can be non-zero because of uncertainties without fault.

A simple approach to identify faults is the fixed threshold. A fault is detected when residual exceeds the threshold. The choice of the fixed threshold depends on the system operating conditions and can vary with input. Figure 2-2 shows how a residual can vary

with input in time. Fault detection systems using a fixed threshold as in this case would cause a false alarm or could also miss the fault condition altogether [**10**].

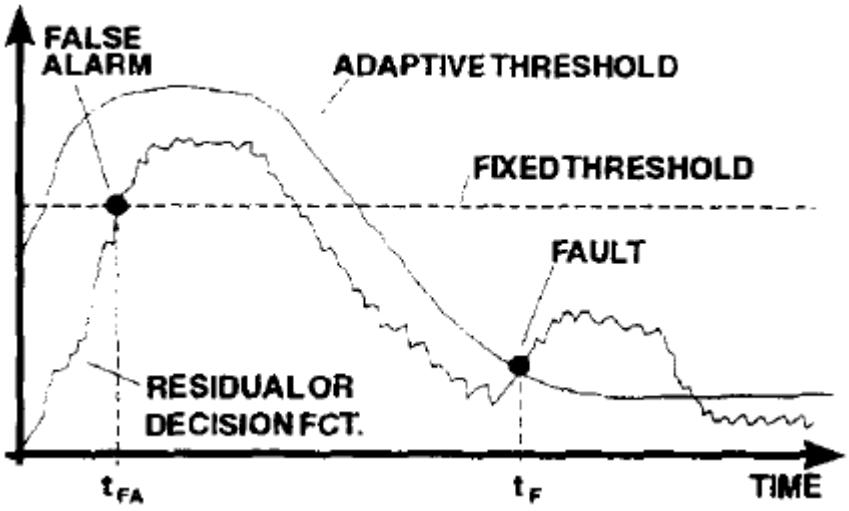

Figure 2-2: Adaptive threshold test of the residual or decision function (Taken from [10])

Patton et al introduced the concept of the adaptive threshold based on input in 1989 [**11**]. They proposed an evaluation function for calculating the threshold based on input. Emami-Naeini et al set the adaptive threshold as the root mean square of the residual in time [**12**]. Mάrton et al developed an observer-based fault detection system to detect faults due to overload on an Electro-Hydrostatic Actuator platform [**13**]. The maximum input disturbance was calculated based on actuator position. When the actuator was jammed due to an overloaded aerodynamic force, the UIO calculated an input disturbance higher than the threshold. Fault was thereby detected [**13**].

Khan et al developed a fault detection system that implemented nonlinear UIO to generate residuals, and Wald's sequential test for decision making [**14**]. In the experiments on an electro-hydraulic positioning system, Khan et. al successfully detected pump faults and position sensor faults by using velocity measurements only [**14**].

Sibar et al proposed a fault detection algorithm using the adaptive observer [**15**]. Instead of generating a residual based on the difference between the observation and the measurement only, the adaptive observer combined it with parameter estimation. Their

algorithm tracked parameters by developing a relationship between the parameter estimation error and the observation error. Fault detection was achieved when estimated parameters deviated from their pre-defined values.

Wang et al presented in detail the implementation of an adaptive observer-based fault detection strategy on both linear and nonlinear platforms in [**16**]. Computer simulations demonstrated that both sensor and actuator faults can be successfully detected. Although their adaptive observer provided excellent performance, the implementation was complicated, especially when a bank of observers were used to detect and diagnose different types of faults [**16**].

2.4 Filtering Based Approach

Another approach to generate the residual involves state and parameter estimation using filters such as the popular Kalman filter and the relatively new Smooth Variable Structure filter [**7**].

2.4.1 Kalman Filtering

Since Rudolph Kalman presented his new approach to linear filtering and prediction problems in 1960 [**17**], the Kalman filter has been widely used in industry and nominated as *one of the greater discoveries in statistical estimation history* [**18**]. It gives mankind the ability to estimate states and parameters of a linear system in real-time. The successful application of the Kalman filter in NASA's lunar and Apollo mission quickly made it become the most popular estimation technique [**19**] [**20**].

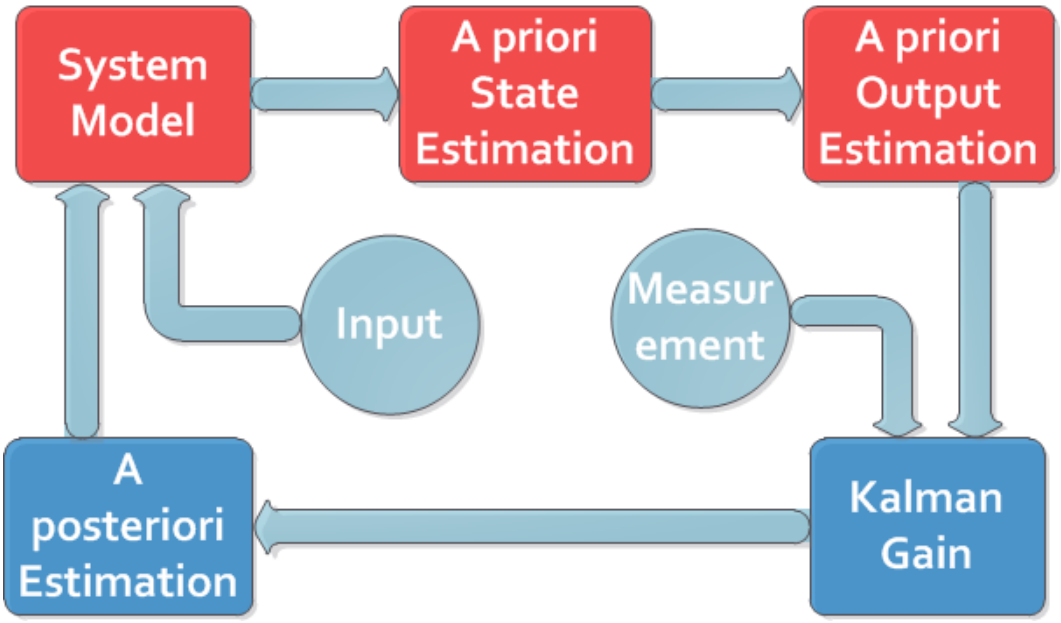

Figure 2-3: Predictor-corrector structure of Kalman Filter

The Kalman filter is applied to stochastic systems. The modeling and measurement uncertainties in the Kalman filter (KF) are characterized as zero mean Gaussian noise with time invariant covariance. As a recursive process, KF has a predictor-corrector structure as shown in Figure 2-3. It firstly obtains a prediction of the system states and outputs by using a model. It then compares the predicted and the measured output. Their difference is calculated and named as the innovation. A corrective gain named the Kalman gain is calculated using the innovation and applied to update the estimation of the a priori states.

2.4.1.1 Linear Approach

The implementation of the Kalman Filter in its discrete form for linear systems consists of five main steps. Consider the following linear system:

$$X_{k+1} = A_{sys}X_k + B_{sys}U_k + w_k$$
$$Z_{k+1} = C_{sys}X_{k+1} + v_k \quad (2\text{-}18)$$

where X denotes the state vector; U stands for the system input vector; and the subscripts k and $k+1$ represent the k^{th} and $k+1^{th}$ step of the recursive process. Matrixes A_{sys}, B_{sys}, and C_{sys} form the state space model. Z is the measurement vector.w_k and v_k are the system and measurement noise. They are assumed to be white and have probability distribution function as:

$$p(w_k) \sim \mathcal{N}(0, Q)$$
$$p(v_k) \sim \mathcal{N}(0, R) \tag{2-19}$$

As the first step of state estimation, the "a priori" predictions of states and outputs are calculated based on the system model and the previous estimates.

$$\hat{X}_{k+1|k} = A_{sys}\hat{X}_{k|k} + B_{sys}U_k$$
$$\hat{Z}_{k+1|k} = C_{sys}\hat{X}_{k+1|k} \tag{2-20}$$

The subscript $k+1|k$ represents a prediction at time iteration $k+1$ based on information from iteration$k$. $\hat{X}$ denotes system state prediction or estimation. The 'a priori' error covariance matrix $P_{k+1|1}$ is updated as:

$$P_{k+1|k} = A_{sys}P_{k|k}A_{sys}^T + Q \tag{2-21}$$

The Kalman gain K^{KF} is defined by Eqn (2-22), and is used to correct the 'a priori' estimate from Eqn (2-20) and update it to the "a posteriori" estimations form:

$$K_{k+1}^{KF} = P_{k+1|k}H_{sys}^T\left(C_{sys}^T P_{k+1|k}C_{sys}^T + R\right)^{-1} \tag{2-22}$$

$$\hat{X}_{k+1|k+1} = \hat{Z}_{k+1|k} + K_{k+1}^{KF}(Z_{k+1} - \hat{Z}_{k+1|k}) \tag{2-23}$$

The "a posteriori" estimation error covariance $P_{k+1|k+1}$ is then calculated by using Eqn (2-24) and then used in Eqn (2-21) for the next iteration.

$$P_{k+1|k+1} = \left(I - K_{k+1}^{KF} C_{sys}\right) P_{k+1|k} \tag{2-24}$$

Equations (2-20) to (2-24) are used recursively to estimate states at each iteration.

2.4.1.2 Nonlinear Approach

In practice, the target system is usually nonlinear. To apply the KF concept to non-linear systems, a number of algorithms have been developed. The Perturbation Kalman Filter and the Extended Kalman Filter (EKF) use linearization. The Unscented Kalman Filter (UKF) and the Cubature Kalman Filter (CKF) use data points to project the state probability distribution from one time iteration to the next [**21**]. In this research, the Extended Kalman Filter is chosen for nonlinear state estimation because of its simple implementation and relatively low computation cost.

The Extended Kalman Filter (EKF) has a similar structure as the KF. Assume a nonlinear system with the following model:

$$\begin{aligned} X_{k+1} &= f(x_k, u_k) + w_k \\ Z_{k+1} &= h(x_{k+1}) + v_k \end{aligned} \tag{2-25}$$

Similar to the KF, the EKF predicts the 'a priori' states and outputs using the model and the previous estimates as in Eqn (2-26).

$$\begin{aligned} \hat{X}_{k+1|k} &= f\left(\hat{X}_{k|k}, u_k\right) \\ \hat{Z}_{k+1|k} &= h\left(\hat{X}_{k+1|k}\right) \end{aligned} \tag{2-26}$$

The model is then linearized and the Jacobian matrices F_{sys} and H_{sys} are calculated as:

$$F_{sys} = \left.\frac{\partial f(x)}{\partial x}\right|_{x=\hat{x}_{k|k},u_k}$$
$$H_{sys} = \left.\frac{\partial h(x)}{\partial x}\right|_{x=\hat{x}_{k+1|k}} \quad (2\text{-}27)$$

The 'a priori' states error covariance $P_{k+1|k}$ and Kalman gain K are updated by using the linearized model:

$$P_{k+1|k} = F_{sys}P_{k|k}F_{sys}^T + Q \quad (2\text{-}28)$$

$$K_{k+1}^{KF} = P_{k+1|k}H_{sys}^T\left(H_{sys}^T P_{k+1|k}H_{sys}^T + R\right)^{-1} \quad (2\text{-}29)$$

The "a posteriori" state estimation and estimation error covariance are updated as:

$$\hat{X}_{k+1|k+1} = \hat{X}_{k+1|k} + K_{k+1}^{KF}(Z_{k+1} - \hat{Z}_{k+1|k}) \quad (2\text{-}30)$$

$$P_{k+1|k+1} = \left(I - K_{k+1}^{KF}H_{sys}\right)P_{k+1|k} \quad (2\text{-}31)$$

Note that, extra uncertainties are introduced by using linearization model and the EKF thereby loses its optimality [**21**].

2.4.1.3 Observability

A system is defined as observable when its state vector can be uniquely estimated from the system measurements. The observability matrix is formulated as Eqn (2-32):

$$observability\ matrix = \begin{bmatrix} C_{sys} \\ C_{sys}A_{sys} \\ \cdots \\ C_{sys}\left(A_{sys}\right)^{n-1} \end{bmatrix} \quad (2\text{-}32)$$

where n is the number of states. If the rank of the observability matrix equals to the number of states, a system is considered to be observable. For nonlinear systems, the observability is considered locally using a linearized model with the Jacobian matrices.

2.4.1.4 Fault Detection and Diagnosis using the Kalman Filter

The innovation can be used as a residual for fault detection as it quantifies the deviation of model predictions from measurements. When the system runs normally, the innovation is mainly due to system and measurement noise and is assumed to be white. With faults happening, the assumption of zero mean Gaussian noise is violated. The innovation becomes no longer normally distributed with zero mean. Okita et al presented foot slip detection with the Kalman filter and the Unscented Kalman filter (UKF) [**22**]. The experimental results showed a sharp increase of innovation when slip was present. By having innovation compared to a threshold, the slip fault was detected successfully. Sephasi developed a fault monitoring strategy for hydraulic actuators by using the UKF [**23**]. Instead of setting a fixed threshold, Sephasi calculated the moving average of errors (MAE). The MAE values with and without faults were compared. A sharp increase of the MAE was observed with the presence of a fault. Based on this finding, four individual faults (external leakages at two chambers, dynamic friction load, and sudden load change) were detected and diagnosed by observing changes in the innovation [**24**].

Faults modify system dynamics and cause model parameters to change. Therefore, faults can also be detected by tracking change in model parameters. Chinnah applied a fault detection strategy on an electro-hydrostatic actuator by using the Extended Kalman filter (EKF) [**25**]. The key parameters estimated were the effective bulk modulus and viscous damping coefficient. Two faults (entrapped air and change in viscous friction) were correctly identified by observing changes in the parameters.

2.4.2 Smooth Variable Structure Filter

The Kalman Filter achieves optimality by assuming that: [**19**].

- the target system is linear; and
- the system and measurement uncertainties result in white noise.

The Kalman filter loses its optimality when these assumptions are violated. Furthermore, it becomes unstable in extreme case of modeling uncertainties.

Based on the variable structure control and systems theory, Habibi proposed an estimation method referred to as the Smooth Variable Structure Filter (SVSF) in 2007 [**26**]. The estimation algorithm involves an inherent switching action that forces the estimated states to converge towards the true state trajectory and remain within a neighborhood of it referred to as the existence subspace [**26**].The SVSF is robust to disturbances and can guarantee stability given bounded uncertainties.

SVSF can be applied to both linear and nonlinear systems. The filter works with an assumption that the measurement model of the system is linear, pseudo diagonal, positive, and time invariant. In reality, this assumption is valid since most sensors are designed to be linear and accurately calibrated [**26**]. Besides, it is assumed that the absolute pressure sensors and the optical linear encoder have Gaussian noise with zero mean.

Similarly to the Kalman Filter, the SVSF has a predictor-corrector structure as shown in Figure 2-4.

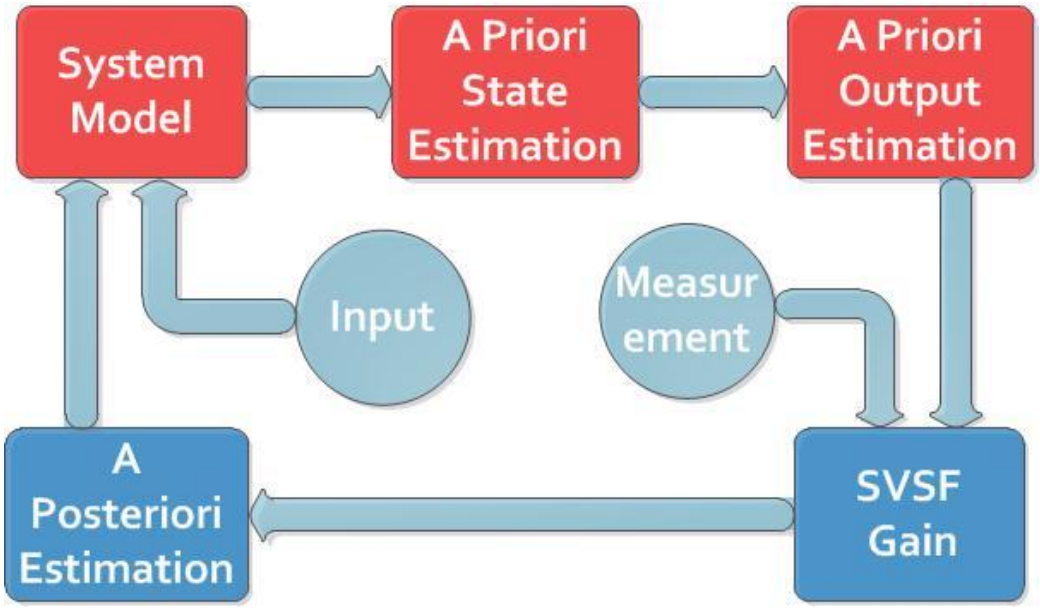

Figure 2-4: Predictor-corrector structure of SVSF

The SVSF assumes a system model formulated as in (2-33).

$$X_{k+1} = f(X_k, U_k) + w_k$$
$$Z_{k+1} = H_{sys} X_{k+1} + v_k \tag{2-33}$$

The formula f could be either linear or nonlinear while the measurement matrix H_{sys} is linear, positive, and pseudo diagonal. Similar to the KF, at each iteration the SVSF starts with the "a priori" estimation of states and outputs.

$$\hat{X}_{k+1|k} = f(X_{k|k}, U_k)$$
$$\hat{Z}_{k+1|k} = H_{sys} \hat{X}_{k+1|k} \tag{2-34}$$

After the "a priori" estimation is calculated, the "a posteriori" estimation is updated with a corrective gain K_{k+1}^{SVSF} as Eqn (2-35).

$$\hat{X}_{k+1|k+1} = \hat{X}_{k+1|k} + K_{k+1}^{SVSF}$$
$$\hat{Z}_{k+1|k+1} = H_{sys}\hat{X}_{k+1|k+1} \quad (2\text{-}35)$$

2.4.2.1 Fixed smooth boundary layer

The Kalman Filter achieves optimality by minimizing the "a posteriori" error covariance [**27**] and assuming a known model with zero-mean Gaussian noise. A different mechanism is used in the SVSF. Its concept is demonstrated in the Figure 2-5.

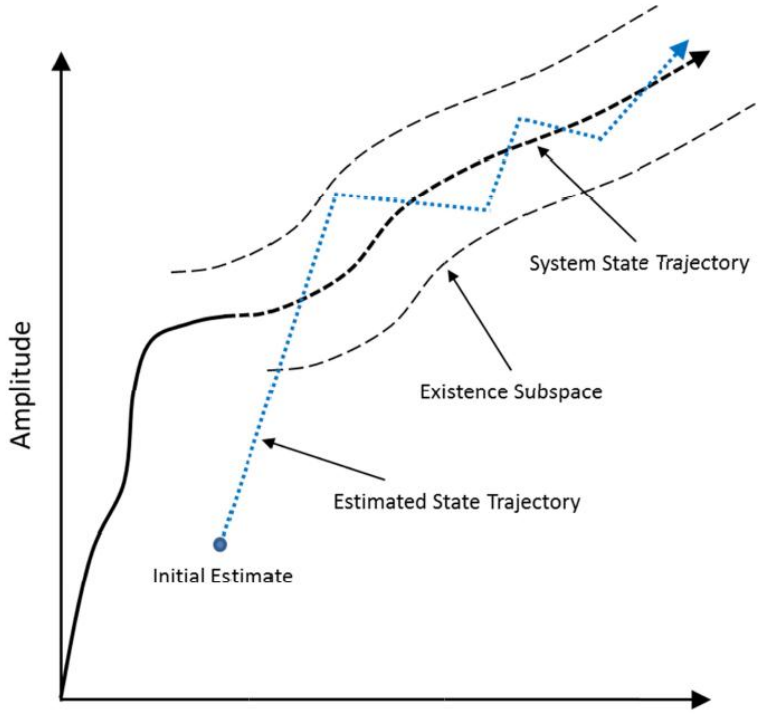

Figure 2-5: SVSF corrector concept [21]

The estimated state is forced towards the true state trajectory by a corrective gain (K^{SVSF}). The estimated state would chatter and slide along the true state trajectory while remaining within a neighbourhood referred to as the existence subspace. The existence subspace width is a function of uncertainties and is time varying. The stability and convergence of the estimation outside the existence subspace is achieved by Eqn (2-36).

$$|E_k| < |E_{k-1}| \tag{2-36}$$

where E is the state estimation error. Let by the measurement estimation error E_z be defined as:

$$E_{z,k+1|k} = Z_{k+1} - \hat{Z}_{k+1|k} \tag{2-37}$$

In order to satisfy the condition (2-36), the corrective gain is formulated as Eqn (2-38).

$$K_{k+1}^{SVSF} = H_{sys}^{-1}\left(\left|E_{z,k+1|k}\right| + \gamma\left|E_{z,k|k}\right|\right) \circ sgn(E_{z,k+1|k}) \tag{2-38}$$

where γ is the memory of convergence rate, with a value between 0 to 1. The detailed derivation of the SVSF gain can be found in [**26**]. The sign function $sgn(E_{z,k+1|k})$ causes chattering. In order to remove the chattering, the sign function is replaced with a saturation function defined as Eqn (2-40).

$$K_{k+1}^{SVSF} = H_{sys}^{+}\left(\left|E_{z,k+1|k}\right| + \gamma\left|E_{z,k|k}\right|\right) \circ sat\left(\frac{E_{z,k+1|k}}{\psi}\right) \tag{2-39}$$

$$sat\left(\frac{a}{\psi}\right) = \begin{cases} if\ |a| > \psi; sat\left(\frac{a}{\psi}\right) = sgn(a) \\ if\ |a| \leq \psi; sat\left(\frac{a}{\psi}\right) = \frac{a}{\psi} \end{cases} \tag{2-40}$$

where ψ denotes smooth boundary layer width.

The performance of SVSF is significantly affected by ψ [**21**]. If ψ is chosen too large, the SVSF gain would approach zero according to (2-39). The "a posteriori" estimation therefore simply equals to the model prediction. On the other hand, if ψ is chosen too small, the "a posteriori" estimation becomes the same as the measurement [**21**]. As a conservative choice, ψ can be chosen as the upper bound of the system uncertainty and calculated by using Eqn (2-41) [**26**].

$$\psi = \tilde{A}_{sys,max}\left(H^{-1}_{sys,max}(z_{max} - v_{max})\right) + \tilde{B}_{sys,max}u_{max} + w_{max} \qquad (2\text{-}41)$$

The parameters $\tilde{A}_{sys,max}$ $H_{sys,max}$ and $\tilde{B}_{sys,max}$are the maximum error of the system and the measurement models.

2.4.2.2 Varying boundary layer

With fixed ψ equal to the upper bound of uncertainty, the accuracy of the SVSF is limited as the uncertainty is over estimated. Inspired by the Kalman Filter, Gadsden proposed a time Varying Boundary Layer (VBL) to improve the SVSF estimation accuracy [**21**]. The VBL is calculated by minimizing the estimation error covariance as:

$$\frac{\partial\left(trace\left(P_{k+1|k+1}\right)\right)}{\partial\psi} = 0 \qquad (2\text{-}42)$$

Gadsden developed a process for the state using the estimation error covariance for the SVSF as follows:

$$K^{SVSF}_{k+1} = H^{+}_{sys}\left(\left|E_{z,k+1|k}\right| + \gamma\left|E_{z,k|k}\right|\right) \circ sat\left(\frac{E_{z,k+1|k}}{\psi}\right) diag\left(E_{z,k+1|k}\right)^{-1} \qquad (2\text{-}43)$$

$$X_{k+1|k+1} = X_{k+1|k} + K^{SVSF}_{k+1}E_{z,k+1|k}$$

$$P_{k+1|k} = F_{sys}P_{k|k}F^{T}_{sys} + Q_k$$

$$P_{k+1|k+1} = \left(I - K_{k+1}H_{sys}\right)P_{k+1|k}\left(I - K_{k+1}H_{sys}\right)^{T} + K_{k+1}R_{k+1}K^{T}_{k+1} \qquad (2\text{-}44)$$

where A_{sys} stands for the linear system model. When the system is nonlinear, A_{sys} can be obtained by linearization. From Eqn (2-43) and (2-44) to (2-42) :

$$S_{k+1} = H_{sys} P_{k+1|k} H_{sys}^T + R_{k+1}$$
$$\psi_{k+1} = \left(diag\left(\left| E_{z,k+1|k} \right| + \gamma \left| E_{z,k|k} \right| \right)^{-1} H_{sys} P_{k+1|k} H_{sys}^T S_{k+1}^{-1} \right)^{-1} \quad (2\text{-}45)$$

Gadsden's later research discovered that the SVSF with VBL yields the KF solution in linear system and loses its robustness to modeling uncertainty. To overcome this drawback, a saturation limit (ψ_{max}) is imposed to the VBL. The concept is shown in Figure 2-6.

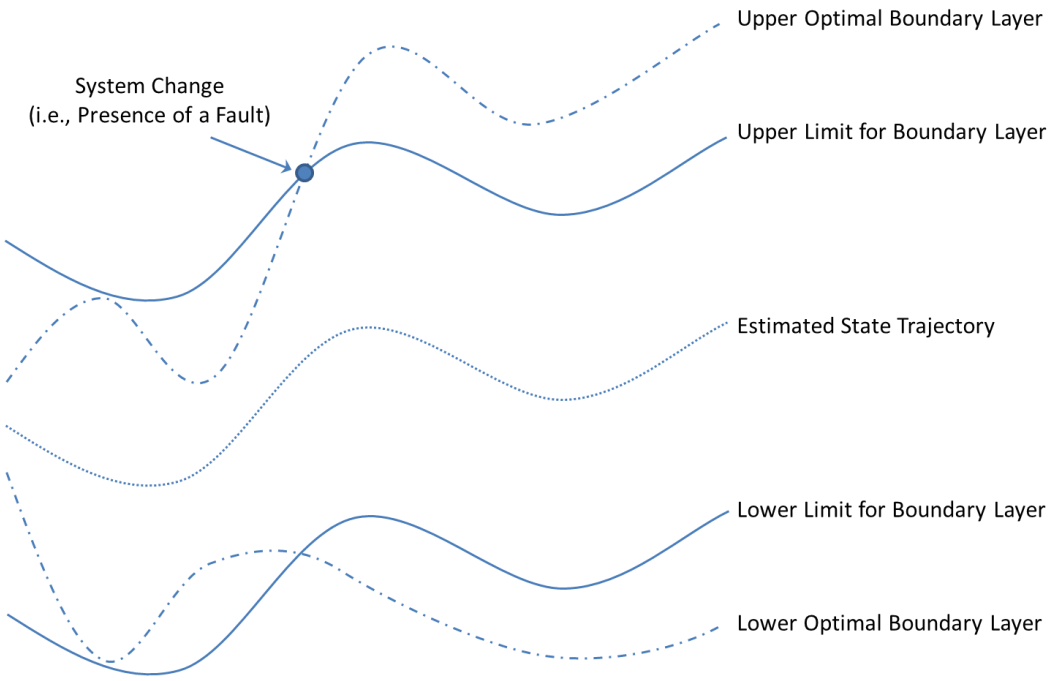

Figure 2-6: Concept of combined VBL (Taken from [21])

When the system model is accurate, the VBL varies within the saturation limit (ψ_{max}) and gives an optimal solutions. Once the system is subjected to uncertainties and disturbances, (e.g. presence of a fault), the VBL width goes outside the saturation limit due to increased uncertainty. The SVSF limits $\psi \; to \; \psi_{max}$ and forces the estimated trajectory to follow the true trajectory. The calculation of ψ with ψ_{max} is summarized as Eqn (2-46).

$$\psi_{k+1} = \left(diag\left(\left|E_{z,k+1|k}\right| + \gamma\left|E_{z,k|k}\right|\right)^{-1} H_{sys} P_{k+1|k} H_{sys}^{T} S_{k+1}^{-1}\right)^{-1}$$

$$\psi_{k+1} = \begin{cases} \psi_{max} \ if \ abs(\psi_{k+1}) \geq \psi_{max} \\ \psi_{k+1} \ if \ abs(\psi_{k+1}) < \psi_{max} \end{cases} \tag{2-46}$$

2.5 Multiple Model

With a residual generated using an estimator like the KF or the SVSF, faults can be detected. However, a complete fault detection system demands isolation and identification of faults. When multiple faults happen at the same time, a Multiple Model (MM) approach can be considered as one of the most effective fault detection methodologies [**28**] [**29**]. The idea is to run a bank of filters in parallel, each having a model associated with a particular fault condition (or mode). A probability is assigned to each filter based on its residual to indicate the correspondence of the filter to the system condition. At the end of each iteration an overall 'a posteriori' estimate is calculated as a weighted sum of all filter estimates based on their probabilities.

By using model switching during the estimation process, the MM approach can be implemented as static or dynamic. Static MM assumes no model switching during the estimation process. One of the models is assumed to be true and remaining true during the whole estimation process. Since it is not practical to neglect mode switching, the static MM is less accurate than the dynamic approach [**29**].

Dynamic MM involves model switching during estimation by considering predefined mode transition probability p_{ij}. p_{ij} is a time invariant parameter, the value of which relies on system design. One of the challenges to achieve dynamic MM is mode switching history. With 2 modes (A and B), there would be only two possible sequences at any time (either A or B). In the next time inverval, the number of possibilities increases to 4 (square of previous) and expands exponentially as the process moves forward. The calculation cost becomes unaffordable to provide estimation for each sequence [**30**].

In practice, a suboptimal algorithm is used to account for history. Generalized pseudo-Bayesian (GPB) uses a truncated history for model switching. Most of the time, a first or a second order GPB is chosen. With more information from the past, the second order GPB (or GPB2) has a higher accuracy than the first order GPB (or GPB1). But the computation cost of GPB2 grows significantly with an increase in the number of modes.

2.5.1.1 Interacting Multiple Model

Another approach for the dynamic MM is the Interacting Multiple Model (IMM). IMM mixes knowledge obtained at the previous time interval (such as the state estimations, the error covariance and the mode probabilities) to calculate the current mode and to expand that to improve estimation by mixing [**21**]. The mixing process combines the output of the models (state estimations) and takes place at the beginning of each estimation iteration.

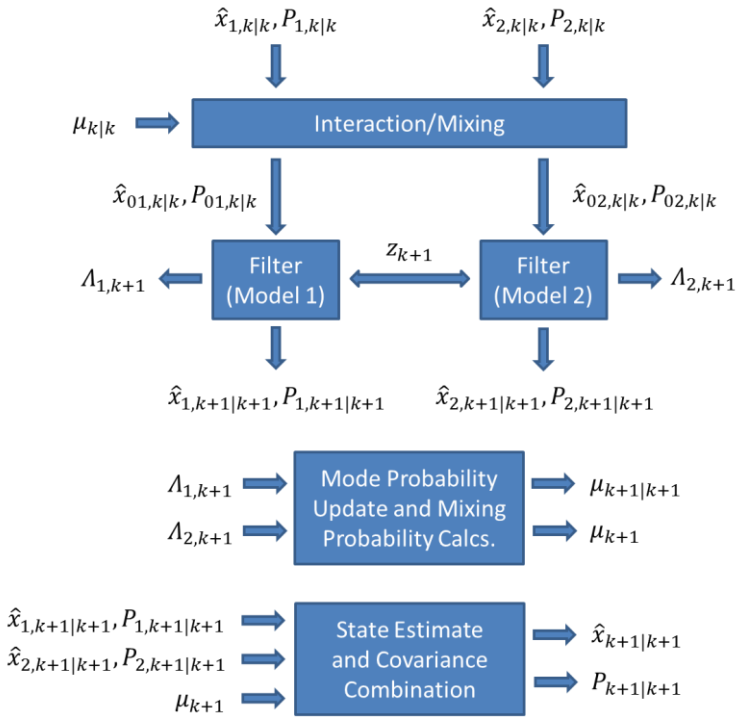

Figure 2-7: IMM strategy for two models (Taken from [21])

Figure 2-7 demonstrates the IMM concept for a system with two models. The IMM can be divided into four major steps. At the beginning, the interaction/mixing process

combines the information from previous estimation (using mode probabilities $\mu_{i,k|k}$, state estimates $\hat{x}_{i,k|k}$ and error covariance $P_{i,k|k}$) to calculate the initial values ($\hat{x}_{0j,k|k}, P_{0j,k|k}$) from the 'a posteriori' estimate of previous time interval for each filter.

The mixing probabilities denoted as $\mu_{i|j,k|k}$ are calculated at the beginning of each iteration step. Assume a system which consists of r models:

$$\mu_{i|j,k|k} = \frac{1}{\overline{c_j}} p_{ij} \mu_{i,k|k}$$
$$\overline{c_j} = \sum_{i=1}^{r} p_{ij} \mu_{i,k|k} \tag{2-47}$$

With the mixing probabilities, the initial values for each filter are calculated based on the 'a posteriori' estimate and error covariance from previous time interval as:

$$\hat{X}_{0j,k|k} = \sum_{i=1}^{r} \hat{X}_{i,k|k} \mu_{i|j,k|k}$$
$$P_{0j,k|k} = \sum_{i=1}^{r} \mu_{i|j,k|k} \left\{ P_{i,k|k} + \left(\hat{X}_{i,k|k} - \hat{X}_{0j,k|k}\right)\left(\hat{X}_{i,k|k} - \hat{X}_{0j,k|k}\right)^T \right\} \tag{2-48}$$

As the second step, filters with different models estimate states in parallel. The states estimations and the error covariances ($\hat{X}_{j,k+1|k+1}$and $P_{j,k+1|k+1}$) are updated.

The measurement innovations ($E_{j,z,k+1|k}$) are assume to be normal distributed with zero mean and a variance as the error covariances ($S_{j,k+1}$). A likelihood function $\Lambda_{j,k+1}$is calculated by using a normal distribution function as:

$$\Lambda_{j,k+1} = \frac{1}{\sqrt{\left|2\pi S_{j,k+1}\right|}} \exp\left(\frac{-\frac{1}{2} E_{j,z,k+1|k}^T E_{j,z,k+1|k}}{S_{j,k+1}} \right) \tag{2-49}$$

This likelihood function is used in conjunction with the innovations to indicate the fitness of each model during the estimation process. The mode probabilities ($\mu_{j,k+1}$) are updated based on the likelihood function to identify the fitness of a mode such that:

$$\mu_{j,k+1} = \frac{1}{c}\Lambda_{j,k+1}\sum_{i=1}^{r} p_{ij}\mu_{i,k}$$
$$c = \sum_{j=1}^{r}\Lambda_{j,k+1}\sum_{i=1}^{r} p_{ij}\mu_{i,k} \tag{2-50}$$

where c is a normalized term. As the end of the process, the 'a posteriori' state estimates and error covariance of the system are updated with the mode probabilities and estimate values of each filter as:

$$\hat{X}_{k+1|k+1} = \sum_{j=1}^{r}\hat{X}_{j,k+1|k+1}\mu_{j,k+1}$$
$$P_{k+1|k+1} = \sum_{j=1}^{r}\mu_{j,k+1}\Big\{P_{j,k+1|k+1} + \left(\hat{X}_{j,k+1|k+1} - \hat{X}_{k+1|k+1}\right)\left(\hat{X}_{j,k+1|k+1} - \hat{X}_{k+1|k+1}\right)^{T}\Big\} \tag{2-51}$$

2.5.1.2 Fault Detection and Diagnosis using Interacting Multiple Model

The MM approach was firstly applied for target tracking and has become a common tool in satellite surveillance, air defence and Air Traffic Control [**31**] [**32**]. Engineers quickly realized that this method could be used for fault detection [**29**]. Zhang et al applied the MM approach for both sensor and actuator fault detection on an F/A-18 flight control system [**29**]. According to the experimental results, their approach enhanced fault detection and identification performance. Although other methods implementing only a single model have the ability to achieve equivalent performance, they usually demand

specific adjustments and can not be broadly applied generally. In contrast, the MM approach is easy to implement and provides excellent fault detection and diagnosis performance. The IMM approach outperforms the other MM methods by having a higher estimation accuracy, requiring less computation and being more robust to transition probabilities [**29**]. Wang et. al successfully detected torque motor fault and effective bulk modulus faults with the Extended Kalman Filter using IMM. Gadsden et. al applied both the KF and the SVSF with IMM to detect and identify leakage and friction faults on McMaster's Electro-hydrostatic Actuator (EHA) prototype [**33**] [**21**]. The experimental results indicated that the IMM-SVSF outperforms IMM-KF by having a better estimation accuracy and higher probability of detecting the correct fault.

3 EHA fault detection and diagnosis strategies

Further to Gadsden's results [**21**] [**33**], the IMM approach was chosen for fault detection and diagnosis. The reasons are listed as follow.

1. The IMM approach can be applied for real-time fault detection.

2. MM approaches provide equivalent performance and easier implementation compared to other single model strategies [**29**]. Amongst the MM approaches, IMM is considered as the most suitable method because of its computational efficiency.

Two strategies, the IMM-EKF and the IMM-SVSF are considered. In the SVSF implementation, the choice of the fixed or varying smooth boundary layer results in another two strategies referred to as the IMM-SVSF (FBL) and the IMM-SVSF (VBL).

The formulations of these three FDD strategies are listed as follow.

Step 1: At mixing stage, the mixing probabilities ($\mu_{i|j,k|k}$) are calculated as Eqn (3-1).

$$\mu_{i|j,k|k} = \frac{1}{\bar{c}_j} p_{ij} \mu_{i,k|k}$$
$$\bar{c}_j = \sum_{i=1}^{r} p_{ij} \mu_{i,k|k} \tag{3-1}$$

Step 2: The mixing probabilities are then used to calculate the initial values ($\hat{x}_{0j,k|k}$, $P_{0j,k|k}$) which are fed to filters for states estimation as Eqn (3-2).

$$\hat{X}_{0j,k|k} = \sum_{i=1}^{r} \hat{X}_{i,k|k} \mu_{i|j,k|k}$$
$$P_{0j,k|k} = \sum_{i=1}^{r} \mu_{i|j,k|k} \left\{ P_{i,k|k} + \left(\hat{X}_{i,k|k} - \hat{X}_{0j,k|k}\right)\left(\hat{X}_{i,k|k} - \hat{X}_{0j,k|k}\right)^T \right\} \tag{3-2}$$

Step 3: When the EKF is implemented, the states are estimated as Eqns (3-3) to (3-9):

The "a priori" predictions of states and outputs are calculated based on the system model and the initial values as Eqn (3-3).

$$\hat{X}_{j,k+1|k} = f_j\left(\hat{X}_{0j,k|k}, u_k\right)$$
$$\hat{Z}_{j,k+1|k} = h_j\left(\hat{X}_{j,k+1|k}\right) \tag{3-3}$$

The model is then linearized and the Jacobian matrices F_{sys} and H_{sys} are calculated as Eqn (3-4).

$$F_{j,sys} = \left.\frac{\partial f_j(x)}{\partial x}\right|_{x=\hat{x}_{0j,k|k}, u_k}$$
$$H_{j,sys} = \left.\frac{\partial h_j(x)}{\partial x}\right|_{x=\hat{x}_{0j,k+1|k}} \tag{3-4}$$

The measurement innovation is updated as Eqn (3-5), and the 'a priori' error covariance and innovation covariance are calculated as Eqn (3-6).

$$E_{j,z,k+1|k} = Z_{k+1} - \hat{Z}_{j,k+1|k} \tag{3-5}$$

$$P_{j,k+1|k} = F_{j,sys} P_{oj,k|k} F_{j,sys}^T + Q$$
$$S_{j,k+1} = H_{j,sys} P_{j,k+1|k} H_{j,sys}^T + R \tag{3-6}$$

The corrective gain K is defined by Eqn (3-7), and is used to correct the 'a priori' estimate from Eqn (3-3) and update it to the "a posteriori" estimations form:

$$K_{j,k+1} = P_{j,k+1|k} H_{j,sys}^T \left(H_{j,sys}^T P_{j,k+1|k} H_{j,sys}^T + R\right)^{-1} \tag{3-7}$$

$$\hat{X}_{j,k+1|k+1} = \hat{X}_{j,k+1|k} + K_{j.k+1}(Z_{k+1} - \hat{Z}_{j,k+1|k}) \tag{3-8}$$

$$P_{j,k+1|k+1} = \left(I - K_{j,k+1} H_{j,sys}\right) P_{j,k+1|k} \tag{3-9}$$

Step 3: When the SVSF (FBL) is implemented, the states are estimated using Eqns(3-10) to (3-16). In the SVSF fixed boundary layer, the width of the boundary layer is estimated as the upper bound of the uncertainties.

The "a priori" predictions of states and outputs are calculated based on the system model and the initial values as Eqn (3-10).

$$\begin{aligned} \hat{X}_{j,k+1|k} &= f_j\left(\hat{X}_{0j,k|k}, u_k\right) \\ \hat{Z}_{j,k+1|k} &= h_j\left(\hat{X}_{j,k+1|k}\right) \end{aligned} \tag{3-10}$$

The measurement innovation is updated as Eqn (3-11), and the 'a priori' error covariance and innovation covariance are calculated as Eqn (3-12).

$$E_{j,z,k+1|k} = Z_{k+1} - \hat{Z}_{j,k+1|k} \tag{3-11}$$

$$P_{j,k+1|k} = F_{j,sys} P_{0j,k|k} F_{j,sys}^T + Q$$

$$S_{j,k+1} = H_{j,sys} P_{j,k+1|k} H_{j,sys}^T + R \tag{3-12}$$

The corrective gain K is defined by Eqn (3-13), and is used to correct the 'a priori' estimate from Eqn (3-10) and update it to the "a posteriori" estimations form:

$$K_{j,k+1} = H_{j,sys}^{-1}\left(\left|E_{j.z,k+1|k}\right| + \gamma\left|E_{j,z,k|k}\right|\right) \circ sat\left(\frac{E_{j,z,k+1|k}}{\psi_{j,k+1}}\right) \tag{3-13}$$

$$\hat{X}_{j,k+1|k+1} = \hat{X}_{j,k+1|k} + K_{j.k+1} E_{j,z,k+1|1} \tag{3-14}$$

$$P_{j,k+1|k+1} = \left(I - K_{j,k+1} H_{j,sys}\right) P_{j,k+1|k} \tag{3-15}$$

$$E_{j,z,k+1|k+1} = Z_{k+1} - H_{j,sys} \hat{X}_{j,k+1|k+1} \tag{3-16}$$

Step 3: When the SVSF varying boundary layer (VBL) is implemented, additional iterative steps are necessary for updating the boundary layer width ψ as Eqn (3-20).

$$\hat{X}_{j,k+1|k} = f_j\left(\hat{X}_{0j,k|k}, u_k\right)$$
$$\hat{Z}_{j,k+1|k} = h_j\left(\hat{X}_{j,k+1|k}\right) \tag{3-17}$$

$$E_{j,z,k+1|k} = Z_{k+1} - \hat{Z}_{j,k+1|k}$$
$$P_{j,k+1|k} = F_{j,sys}P_{0j,k|k}F_{j,sys}^T + Q \tag{3-18}$$

$$S_{j,k+1} = H_{j,sys}P_{j,k+1|k}H_{j,sys}^T + R \tag{3-19}$$

$$\psi_{j,k+1} = \left(diag\left(\left|E_{j,z,k+1|k}\right| + \gamma\left|E_{z,k|k}\right|\right)^{-1} H_{sys}P_{k+1|k}H_{sys}^T S_{k+1}^{-1}\right)^{-1}$$
$$\text{If} \quad \psi_{j,k+1} \geq \psi_{j,max}$$
$$\psi_{j,k+1} = \psi_{j,max} \tag{3-20}$$
$$\text{Else } \psi_{j,k+1} = \psi_{j,k+1}$$

$$K_{j,k+1} = H_{j,sys}^{-1}\left(\left|E_{j.z,k+1|k}\right| + \gamma\left|E_{j,z,k|k}\right|\right) \circ sat\left(\frac{E_{j,z,k+1|k}}{\psi_{j,k+1}}\right) \tag{3-21}$$

$$\hat{X}_{j,k+1|k+1} = \hat{X}_{j,k+1|k} + K_{j.k+1}E_{j,z,k+1|1} \tag{3-22}$$

$$P_{j,k+1|k+1} = \left(I - K_{j,k+1}H_{j,sys}\right)P_{j,k+1|k} \tag{3-23}$$

$$E_{j,z,k+1|k+1} = Z_{k+1} - H_{j,sys}\hat{X}_{j,k+1|k+1} \tag{3-24}$$

Step 4: After the state estimations are updated with each filters, the likelihood function $\Lambda_{j,k+1}$ is calculated based on the measurement innovation ($e_{j,z,k+1|k}$) and the measurement error covariance ($S_{j,k+1}$) .

$$\Lambda_{j,k+1} = \frac{1}{\sqrt{|2\pi S_{j,k+1}|}} \exp\left(\frac{-\frac{1}{2} E_{j,z,k+1|k}^T E_{j,z,k+1|k}}{S_{j,k+1}}\right) \tag{3-25}$$

Step 5: The mode probability ($\mu_{j,k+1}$) is updated based on the likelihood function as:

$$\begin{aligned} u_{j,k+1} &= \frac{1}{c}\Lambda_{j,k+1}\sum_{i=1}^{r} p_{ij}\mu_{i,k} \\ c &= \sum_{j=1}^{r}\Lambda_{j,k+1}\sum_{i=1}^{r} p_{ij}\mu_{i,k} \end{aligned} \tag{3-26}$$

Step 6: As the end of the cycle, final state estimation and covariance of the system are updated with mode probability and estimation values of each mode.

$$\begin{aligned} \hat{X}_{k+1|k+1} &= \sum_{j=1}^{r} \hat{X}_{j,k+1|k+1}\mu_{j,k+1} \\ P_{k+1|k+1} &= \sum_{j=1}^{r} \mu_{j,k+1}\Big\{P_{j,k+1|k+1} \\ &\quad + \big(\hat{X}_{j,k+1|k+1} - \hat{X}_{k+1|k+1}\big)\big(\hat{X}_{j,k+1|k+1} - \hat{X}_{k+1|k+1}\big)^T\Big\} \end{aligned} \tag{3-27}$$

In this thesis, results from the implementation of the IMM-SVSF (VBL), the IMM-SVSF (FBL), and the IMM-EKF are reported. IMMM-EKF is provided for comparison.

4 EHA prototype

4.1 Introduction

Hydraulic actuators have several advantages including: (i) the ability to maneuver large loads; (ii) high torque-to-mass ratio; (iii) control accuracy; and (iv) self-lubrication [**25**] [**3**]. As such, hydraulic systems have been widely used for flight surface control since the 1930s [**3**].

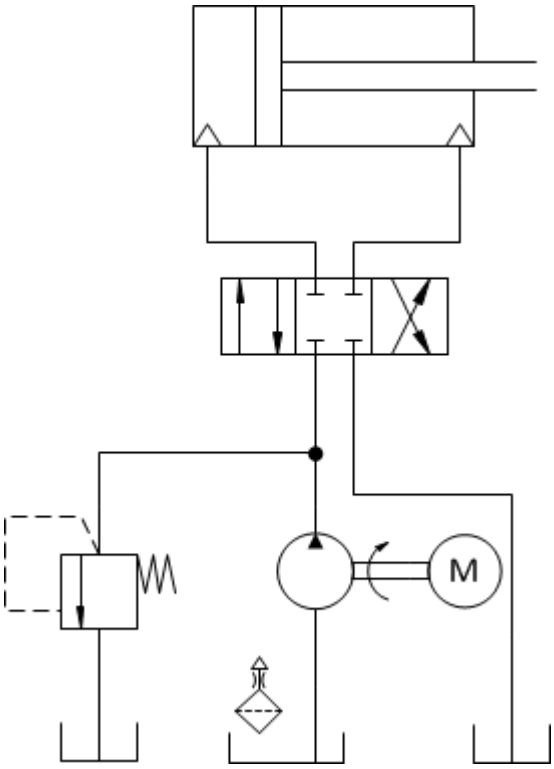

Figure 4-1: Concept of open circuit valve control hydrostatic actuator

Figure 4-1 shows the basic concept of an open circuit valve controlled hydraulic actuator. A pump and a pressure relief mechanism maintain the hydraulic supply pressure at a constant level to provide hydraulic power. Servo-valves control actuation by channeling the fluid flow into actuators and by regulating flow. Valve controlled hydraulic systems have several disadvantages that include: 1. high complexity; 2. heavy weight; 3. relatively low energy efficiency.

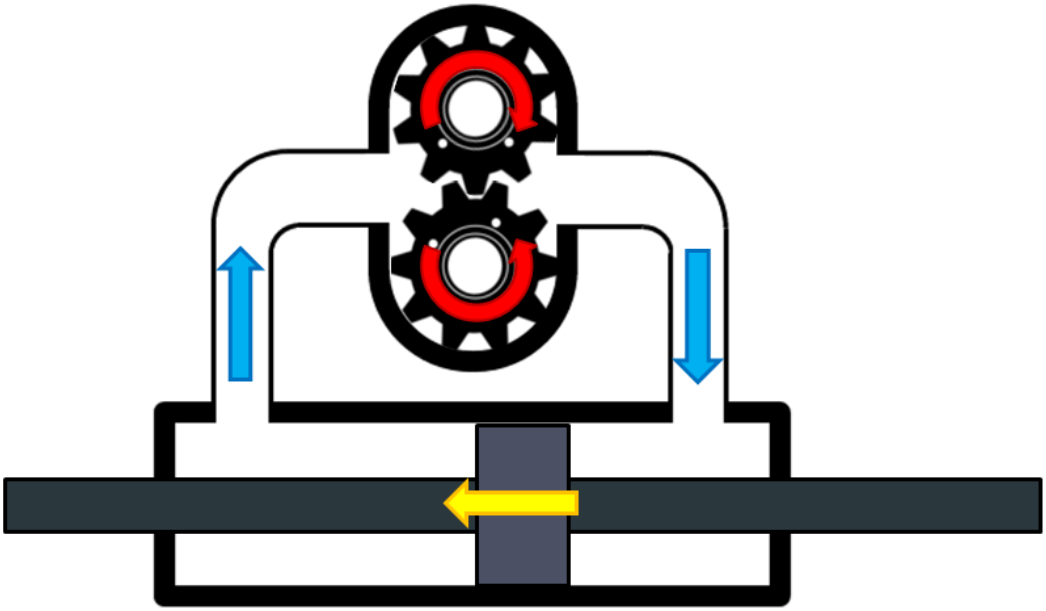

Figure 4-2: Concept of close circuit pump control hydrostatic actuator

The hydraulic system can have an open or a closed circuit based on the way the fluid returns. An open circuit hydraulic system example is shown in Figure 4-1 and has the fluid returned to the reservoir. As another approach, the fluid in a closed circuit hydraulic system returns to pump inlet directly. The simplified diagram in Figure 4-2 demonstrates an example of a closed circuit hydrostatic actuator. As gears rotate, hydraulic fluid such as oil is transferred from one chamber to another. Pumping action results in a pressure difference between the two cylinder chambers, causing actuator motion.

The aerospace industry has been implementing the EHA for flight surface control as a replacement of the conventional open circuit hydraulic system for better performance, higher energy efficiency and more redundancy. As the largest commercial jet, the Airbus A380 implements EHA in its flight surface control system and has saved considerable amount of weight as a result [**34**]. EHAs are increasingly being used in flight surface control as shown in Figure 4-3. Compared to conventional centralized open circuit systems, they achieve higher energy efficiencies and have provided in up to 15% in weight savings [**1**].

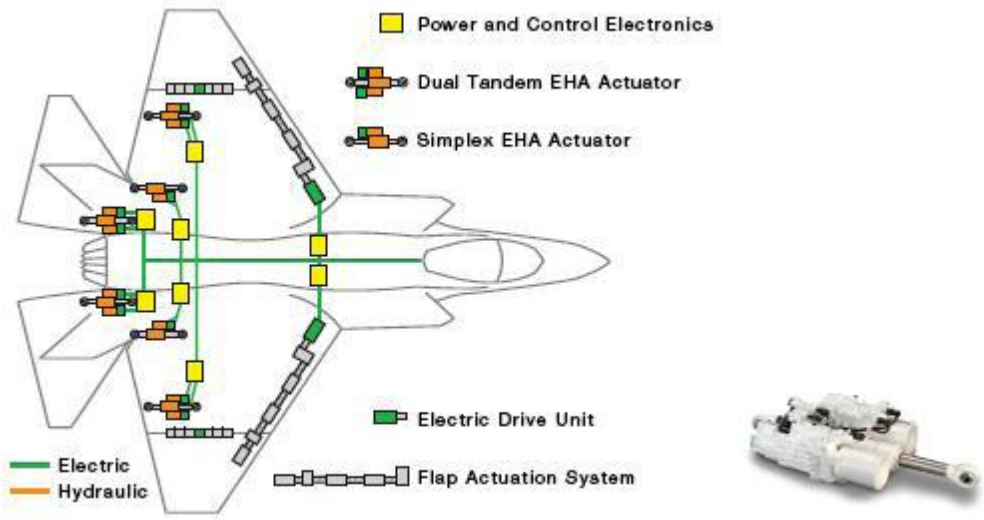

Figure 4-3: Layout of Power-By-Wire system in F35 and EHA (Moog Inc) (Taken from [35])

4.2 Electro-Hydrostatic Actuator Prototype

Figure 4-4 shows an Electro Hydrostatic Actuator prototype built at McMaster University for experimentation [**3**]. It includes auxiliary circuits for fault simulation. In the original design, the prototype was built as a dual system to provide redundancy as shown in Figure 4-5. It this research, the prototype is run as a single system with the second cylinder used for simulating friction as shown in Figure 4-6. The bi-directional fixed displacement pump ② driven by the servo motor ① pumps oil to cylinders ⑥. An inner circuit ❶ consisting of three check valves ③ and an accumulator ⑩ is designed to prevent cavitation and to collect case drain leakage from the gear pump. There is also a pressure relief valve ④circuit for safety.

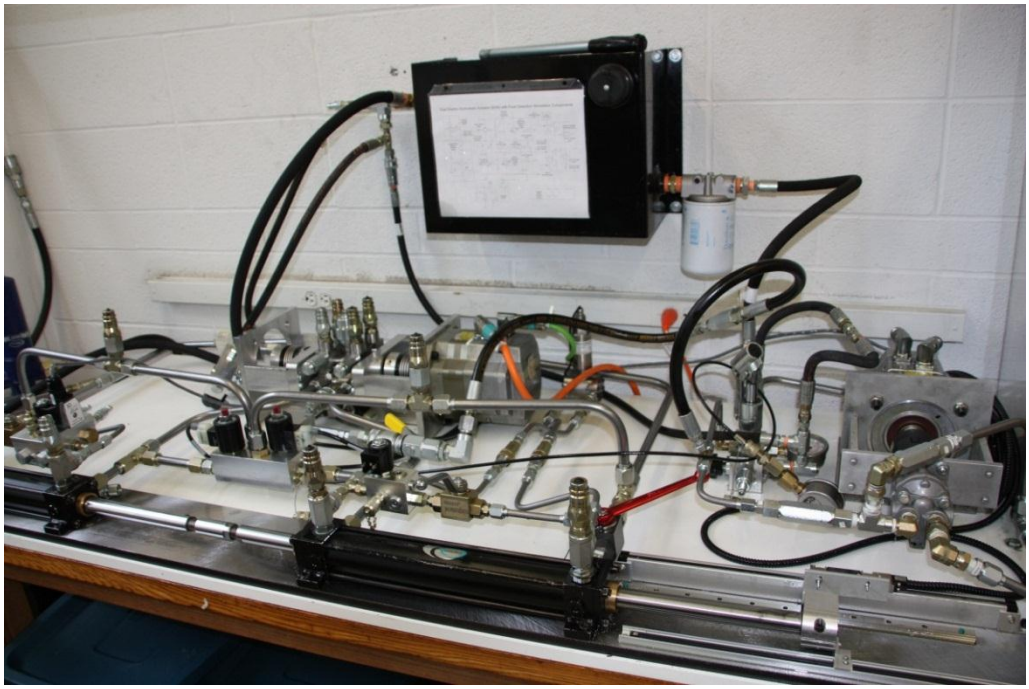

Figure 4-4: Electro Hydrostatic Actuator prototype

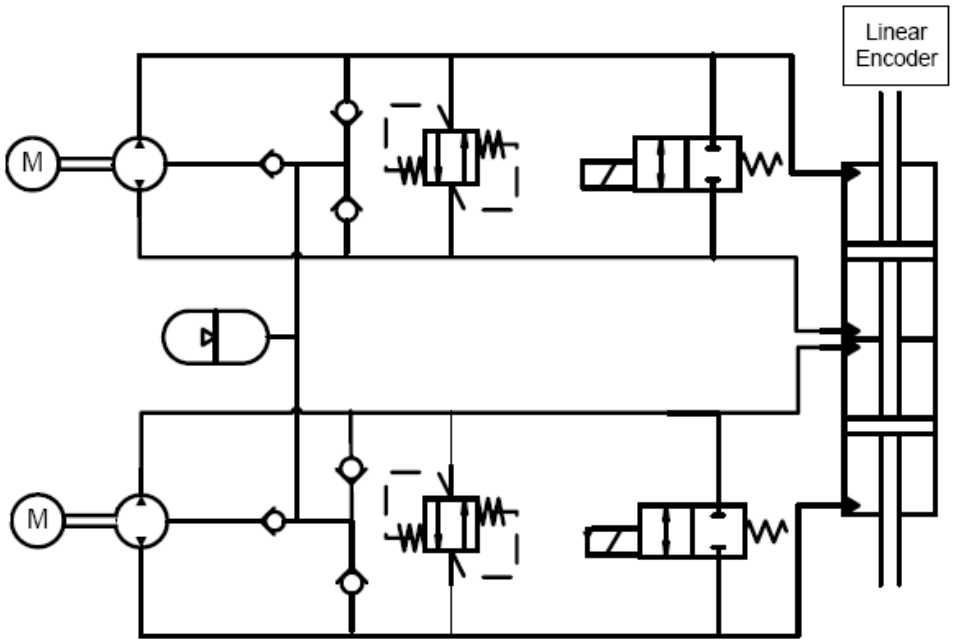

Figure 4-5: EHA dual system design (Adapted from [3])

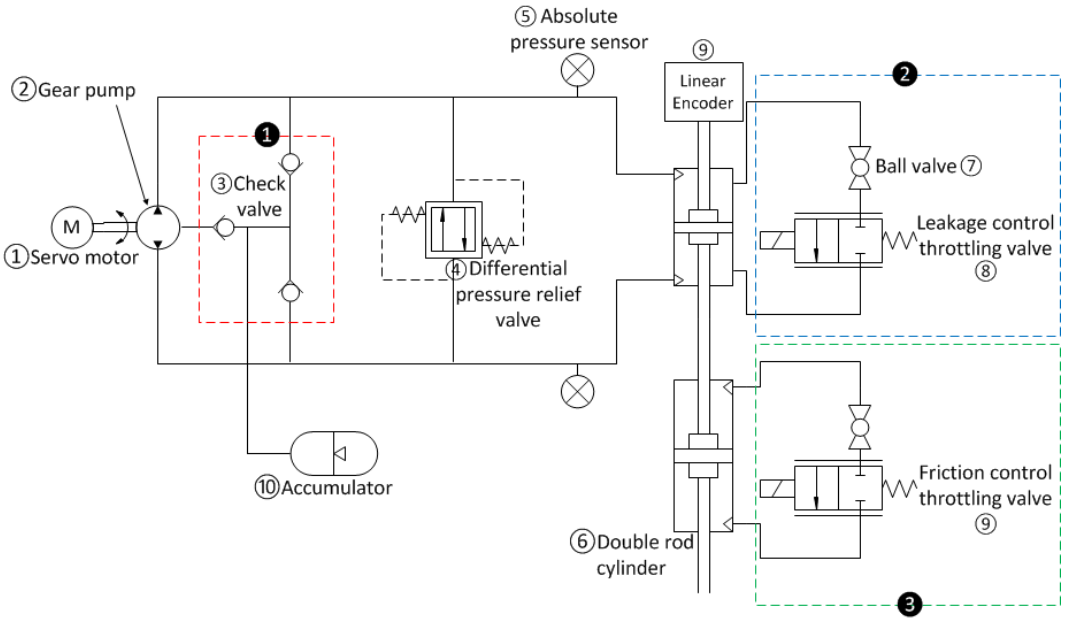

Figure 4-6: Simplified diagram of prototype

During operation, the pressure at the pump inlet drops as flow increases. Air dissolved in oil starts to nucleate and form bubbles under low pressure. The formation of bubbles leads to cavitation which can potentially damage the pump so that the Inner circuit ❶ is therefore used in the EHA of Figure 4-6 in order to prevent cavitation. When two gears mesh, a sealed chamber is created by the meshing teeth. Small amount of fluid is trapped during this process. Due to the incompressibility of oil, the trapped fluid would cause the pump to stall. A case drain is designed in the gear pump from so that the trapped fluid can be released. The inner circuit (❶ in Figure 4-6) is also used to collect the case drain leakage from the pump. It consists of an accumulator and three check valves. The accumulator maintains the inner circuit pressure above 40 Psi. Once the pressure at pump inlet drops below 40 Psi, the pressure difference opens the check valve so that the pump inlet pressure remains above 40 Psi and cavitation is prevented.

The cylinder may stall due to damage or heavy external load. When the cylinder is stalled, pressure inside the system may exceed design limits and damage the EHA. A bidirectional differential pressure relief valve is installed and set to open when pressure

exceeds the max rated pressure. The max pressure for the prototype is 3000 psi, but set to 500 psi during experimentations in this thesis. Therefore, once the pressure at pump outlet is 500 psi higher than the pump inlet, the pressure relief valve would open and release the pressurised fluid.

Two sets of sensors (⑨ and ⑤) are installed. These measure the actuator position and the cylinder differential pressure. The position sensor is a Fagor type MX linear encoder (⑨) and is set up at the tip of cylinder rod. The encoder has a resolution of $1\mu m$ and an accuracy of $5\,\mu m$ [**36**]. The rod velocity and acceleration are derived by the differentiation of the measured position. Although the position measurement has a $1\,\mu m$ resolution, the noise is amplified during the differentiation process. Therefore, the calculated velocity and acceleration are filtered with a 12^{th} order Butterworth low pass filter. The filter cut-off frequency was set 10% larger than the maximum frequency content of the input signal. Note that a higher cut off frequency may be used if there is a concern about signal loss at maximum frequency. Since the low pass filter also brings a phase shift to the measurement, which significantly impacts model estimation, a double-flipped technique was implemented to achieve zero-phase change. The measurement is flipped over and filtered again to restore the signal phase. As shown in Figure 4-6, two absolute pressure transducers (⑤) are attached to cylinder ports respectively. They have a large measurement range of ± 2500 psi and a small error band of 1% of full scale [**37**].

The Siemens 1FK7080-5AF71-1AG2 servo motor is employed. It is controlled and powered by a Siemens drive amplifier Simodrive 611U. This drive receives 3-phase 480V and 30 amperes. A PI controller is built in the drive amplifier for motor control [**3**].

4.3 Fault Study and Simulation

Two faults were considered in this study and simulated on the EHA prototype. These were internal leakage and friction.

4.3.1 Leakage Simulation

Leakage is one of the most common faults occurring in a hydraulic system. In EHA, leakage can result in a reduction of the actuator velocity, and loss of pressure and efficiency. Leakage can be categorized as external or internal. The external leakage occurs at connections and is easier to detect [**23**]. It can be detected by visual inspection [**4**]. On the other hand, internal leakage occurs inside the pump or the cylinder. A minor damage of a piston seal can easily cause internal leakage between cylinder chambers. Since internal leakage is relatively more difficult to detect [**23**], it is chosen as one of the faults to study.

In order to simulate internal leakage in the cylinder, a throttling valve (⑧) is installed to connect the driving cylinder chambers (numbered ❷ in Figure 4-6). The throttling valve used is HydraForce SP08-25, 2-Way, normally open, bi-directional type. Its flow is linearly proportional to the input current [**38**]. A HydraForce proportional valve controller DIN coil mount with 0-10 VDC input range is chosen to control the throttling valve [**39**]. Given 10 VDC input, the throttling valve becomes fully closed. It is fully open when the input is 0 VDC. By partially opening the throttling valve, certain amount of fluid bypasses the cylinder and simulates internal leakage [**3**].

According to experimental observations, the leakage has a direct impact on the actuator velocity. In order to examine the effect of leakage with throttling valve input, 17 throttling inputs were chosen from 0 to 10V. A plot of the actuator velocity versus the throttling valve input can be seen in Figure 4-7. A constant pump speed of $94.25\ rad/\sec\ (900RPM)$ was used for all trials. Three trials were performed to verify repeatability. It was found that the results were repeatable with a small margin of error.

Actuator velocity remained relatively constant at $0.0317\ \mathrm{m/sec}$ with throttling inputs between 10 to $3\ \mathrm{V}$ as shown in Figure 4-7. The actuator velocity started to notably change at $2.5\ \mathrm{V}$, and then it dropped sharply. The velocity measurements are calculated and listed

in Table 4-1. With the throttling valve fully closed at 10 V, the EHA is considered to be working normally without additional internal leakage.

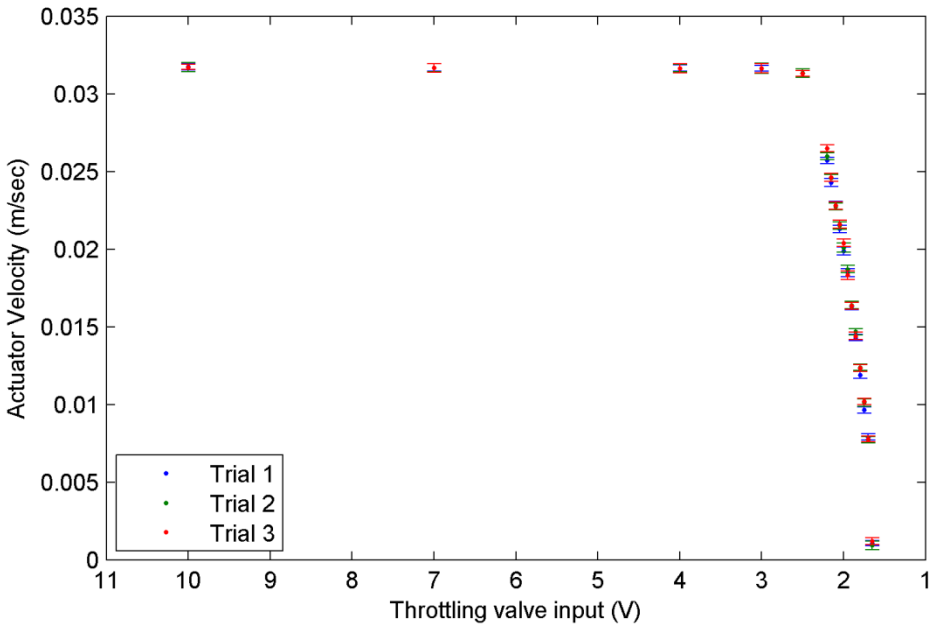

Figure 4-7: Actuator Velocity vs. Leakage throttling input at 900 RPM pump speed

The simulated leakage volumetric flow rate can be obtained from the following formula:

$$Q_{leak} = A\dot{x}_{NC} - A\dot{x} \tag{4-1}$$

where $\dot{x}_{NC}$ stands for the piston velocity of EHA running under normal condition and A is the effective piston area.

The leakage percentage can be calculated as:

$$\%_{leak} = \frac{Q_{leak}}{A\dot{x}_{NC}} = 1 - \frac{\dot{x}}{\dot{x}_{NC}} \tag{4-2}$$

Table 4-1: Actuator Velocity vs. Leakage throttling input at a pump speed of 900 RPM

Leakage control	Actuator	Leakage

throttling valve Input (V)	Velocity (m/sec)	percentage	
10	0.0317	0.00%	Normal
7	0.0317	0.00%	
4	0.0316	0.32%	
3	0.0316	0.32%	
2.5	0.0313	1.26%	
2.2	0.0261	17.67%	
2.15	0.0245	22.71%	
2.1	0.0228	28.08%	
2.05	0.0215	32.18%	
2	0.0201	36.59%	Minor Leakage
1.95	0.0185	41.64%	
1.9	0.0163	48.58%	
1.85	0.0145	54.26%	
1.8	0.0122	61.51%	
1.75	0.01	68.45%	Major Leakage
1.7	0.0078	75.39%	
1.65	0.0011	96.53%	

EHA is defined to be working with minor leakage when it has 36.59% of simulated leakage and major leakage when it is operating under 68.45% of simulated leakage. The corresponding leakage control throttling valve inputs are 2V and 1.75V respectively.

4.3.2 Friction Simulation

Friction is present at the piston seals. Friction is related to seal condition. Too little friction could be an indication of a failed seal On the other hand, excessive friction would not only lead to reduction of efficiency, but also accelerate wear and cause premature seal failure [**40**] [**41**].

Friction fault is difficult to directly simulate without seal replacement. In this research, the friction is simulated by using an auxiliary cylinder which is connected to the driving cylinder in series. As numbered ❸ in Figure 4-6, the auxiliary cylinder chambers are connected using a throttling valve (⑨) to form a closed circuit. The friction control throttling valve is the same HydraForce valve used for leakage simulation. An increased load is generated with decreased valve orifice to simulate increased friction [**3**]. The orifice flow is used to create an effect that is consistent with the effect of friction in the EHA system as reported by [**25**].

According to experimental observations, the simulated friction has a direct impact on the differential pressure of the driving actuator. Thirteen throttling valve inputs were chosen to examine the friction effect.

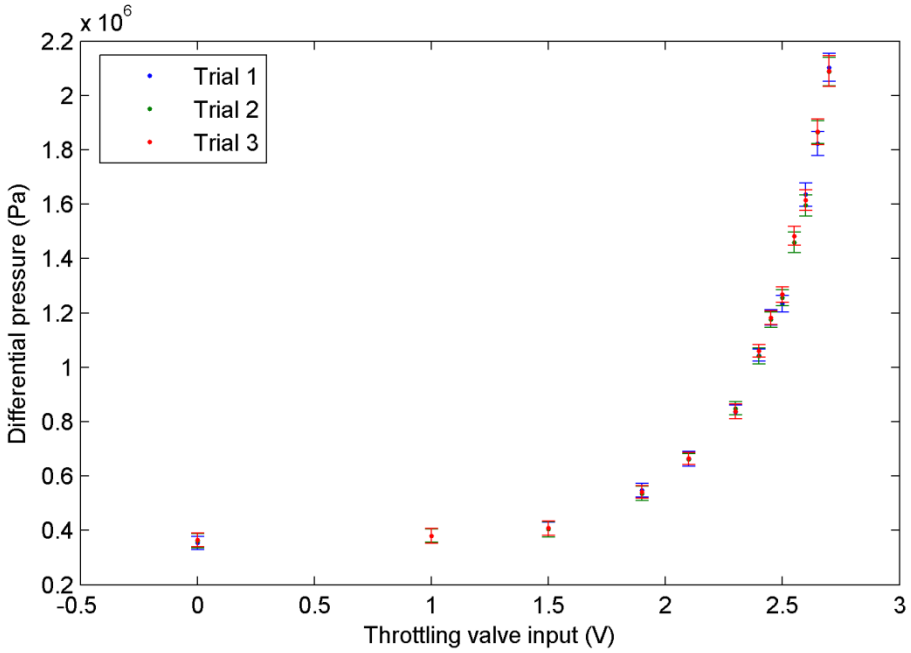

Figure 4-8: Differential pressure vs. Friction throttling input at 900 RPM pump speed

A plot of differential pressure versus friction throttling input can be seen in Figure 4-8. A constant pump speed of $94.25\,rad/\sec\ (900RPM)$ was again used for all trials. Three trials were performed to verify repeatability. It was found that the results were repeatable

with a small margin of error. As expected, the pressure increases quadratically with the throttling valve input. The mean differential pressures of all trials are calculated and listed in Table 4-2. With friction control throttling valve fully open at 0 V, the EHA is considered to be working normally without additional simulated friction.

The additional simulated friction force can be obtained from the following formula:

$$F_f = A\Delta P - A\Delta P_{NC} \tag{4-3}$$

where ΔP_{NC} stands for the differential pressure of EHA running under normal friction and A is the piston area.

The friction percentage is calculated as follows:

$$\%_{friction} = \frac{F_f}{A\Delta P_{NC}} = \frac{\Delta P}{\Delta P_{NC}} - 1 \tag{4-4}$$

Table 4-2: Differential pressure vs. Friction throttling input at 900 RPM pump speed

Friction control throttling valve Input (V)	Differential Pressure (MPa)	Friction percentage	
0	0.3601	0.00%	Normal
1	0.3798	5.47%	
1.5	0.4061	12.77%	
1.9	0.5417	50.43%	
2.1	0.6635	84.25%	
2.3	0.841	133.55%	Minor Friction
2.4	1.0487	191.22%	
2.45	1.1804	227.80%	
2.5	1.2525	247.82%	Major friction
2.55	1.4672	307.44%	
2.6	1.6152	348.54%	
2.65	1.8511	414.05%	
2.7	2.0938	481.45%	

EHA is defined to be working with minor friction when it has 133.55% simulated friction and major friction when it is operating at 247.82% simulated friction. The corresponding friction control throttling valve inputs are 2.3V and 2.5V respectively.

4.3.3 Operating Conditions Classification

Based on experimental tests, 5 conditions are considered in this research defined as normal, minor leakage, major leakage, minor friction and major friction. However, EHA may not only have one fault but both leakage and friction faults at the same time. Therefore, 4 other combined conditions must be taken into account. As such, there are 9 conditions considered as listed in Table 4-3.

Table 4-3: Working conditions

Working conditions	Leakage control throttling input (V)	Friction control throttling input (V)	Short form
Normal	10	0	NC
Minor Leakage	2	0	Min. L
Major Leakage	1.75	0	Maj. L
Minor Friction	10	2.3	Min. F
Major Friction	10	2.5	Maj. F
Minor Leakage and Minor Friction	2	2.3	Min. L & Min. F
Minor Leakage and Major Friction	2	2.5	Min. L & Maj. F
Major Leakage and Minor Friction	1.75	2.3	Maj. L & Min. F
Major Leakage and Major Friction	1.75	2.5	Maj. L & Maj. F

4.4 Conclusion

As a compact, robust, and reliable power distribution method, hydraulic systems have been used for flight surface control for decades. Electro-Hydrostatic Actuators (EHA) are increasingly replacing the conventional valve-controlled systems for better performance, lighter weight and higher energy efficiency. Two common faults, internal leakage and friction, were simulated on an EHA prototype with two throttling valves and an auxiliary circuit. The normal and 8 simulated fault conditions were used as a basis for testing a fault detection and diagnosis (FDD) system in this research as defined in Table 4-3.

5 EHA modeling

5.1 Introduction

A well-developed model library capable of properly describing the EHA dynamics is required for successful fault detection and controller design. In this study, two types of models were obtained: (i) a physical model was mathematically derived; and (ii) a set of parametric models were generated through system identification. The advantage of implementing physical models is that parameters have a physical meaning, and the model provides a mechanism for understanding the dynamic effects present in the system. System identification provides empirical parametric models that are very accurate, but are not explicitly linked to physical parameters [**42**].

5.2 The Physical EHA Model

A physical model was developed for the EHA system in [**38**] and dynamically simplified in [**25**]. The EHA uses a gear pump with constant displacement that be modeled as follows [**25**]:

$$Q_a = D_p\omega_P - \xi(P_a - P_b) - \frac{V_a}{\beta}\frac{dP_a}{dt} - C_{ep}(P_a - P_r) \quad (5\text{-}1)$$

$$Q_b = D_p\omega_P - \xi(P_a - P_b) + \frac{V_b}{\beta}\frac{dP_b}{dt} + C_{ep}(P_a - P_r) \quad (5\text{-}2)$$

where Q_a, Q_b are the pump volumetric flow rate of ports a and b; P_a, P_b are the corresponding port pressures and V_a, V_b are the fluid volume associated with the inlet and outlet; ω_P is the motor angular velocity; ξ is the pump cross-port leakage coefficient; and C_{ep} is the pump external leakage coefficient; β stands for the effective bulk modulus of the working fluid; and P_r is the accumulator pressure. V_a and V_b are assumed to be equal due to the symmetrical design of the system.

The actuator flow is modeled by [**25**]:

$$Q_1 = A\dot{x} + \frac{A(x_0 + x)}{\beta}\frac{dP_1}{dt} + L_{in}(P_1 - P_2) + L_{out}(P_1) \quad (5\text{-}3)$$

$$Q_2 = A\dot{x} - \frac{A(x_0 - x)}{\beta}\frac{dP_2}{dt} + L_{in}(P_1 - P_2) - L_{out}(P_2) \quad (5\text{-}4)$$

where Q_1, Q_2 are the flow rate to and from the two actuator chambers, P_1 and P_2 are the chamber pressures. A is the effective piston area, x stands for the actuator displacement, and $x_0$is the mean position of actuator. L_{in} and L_{out} are the internal and external leakage coefficients. Since a solid tubing is used in the prototype, the pressure impact of pipe expansion and flexibility on the effective bulk modulus is assumed to be negligible. Furthermore, due to the short length of tubing, pump port pressures and flows are assumed to be equal to the actuator inlet and outlet flows and pressures such that:

$$Q_a = Q_1;\ Q_b = Q_2;\ P_1 = P_a;\ P_2 = P_2$$

$$Q_1 + Q_2 = Q_a + Q_b \tag{5-5}$$

Since the actuator is symmetrical and is oriented horizontally, in the absence of gravitational load, $\frac{dP_1}{dt} \approx -\frac{dP_2}{dt}$ [**3**]. V_0 is the nominal volume of each EHA chamber which equals to the pipe plus mean actuator chamber volume given by the following:

$$V_a = V_0 + Ax$$

$$V_b = V_0 - Ax$$

Substituting Eqn (5-1) to (5-4) into (5-5) yields

$$D_p\omega_p = A\dot{x} + \frac{V_0}{\beta}\left(\frac{dP_1}{dt} - \frac{dP_2}{dt}\right) + \left(L_{in} + \frac{L_{out}}{2} + \xi + \frac{C_{ep}}{2}\right) * (P_1 - P_2) \tag{5-6}$$

Using a lump sum leakage coefficient $L_t = L_{lin} + \frac{L_{out}}{2} + \xi + \frac{C_{ep}}{2}$, Eqn (5-6) can be further simplified as:

$$D_p\omega_p = A\dot{x} + \frac{V_0}{\beta}\left(\frac{dP_1}{dt} - \frac{dP_2}{dt}\right) + L_t(P_1 - P_2) \tag{5-7}$$

5.2.1 Leakage Model and Overall Leakage Coefficient

According to the model, the ideal pump flow $D_p\omega_p$ is equal to flow rates associated with the actuator motion $A\dot{x}$, compressibility flow $\frac{V_0}{2\beta}\left(\frac{dP_1}{dt} - \frac{dP_2}{dt}\right)$, and leakage $L_t(P_1 - P_2)$. At steady state, the pressure is constant and $\frac{dP_1}{dt} = \frac{dP_1}{dt} = 0$. Eqn (5-7) is thereby simplified to yield a linear model for leakage as follows:

$$Q_L = D_p\omega_p - A\dot{x} = L_t(P_1 - P_2) \tag{5-8}$$

where Q_L denotes the leakage flow rate.

According to the design of the EHA presented in [**3**], the values of the EHA parameters are listed in the following table.

Table 5-1: EHA parameters and their values

EHA Parameter	Description	Value
D_p	Gear pump volumetric displacement	$5.57 \times 10^{-7}\ m^3/\text{rad}$
A	Piston surface area	$1.52 \times 10^{-3}\ m^2$
V_0	Nominal volume of each EHA chamber	$1.08 \times 10^{-3}\ m^3$

In order to determine the overall leakage coefficient L_t, the EHA system was operated with constant pump speed ω_p of 94.25 rad/sec (900 RPM) under various differential pressures. The differential pressure was modified by changing the friction control throttling valve (open area). Both the differential pressure $(P_1 - P_2)$ and the actuator velocity $(\dot{x})$ were measured, and the leakage condition results were defined in section 4.3.1 and plotted in Figure 5-1.

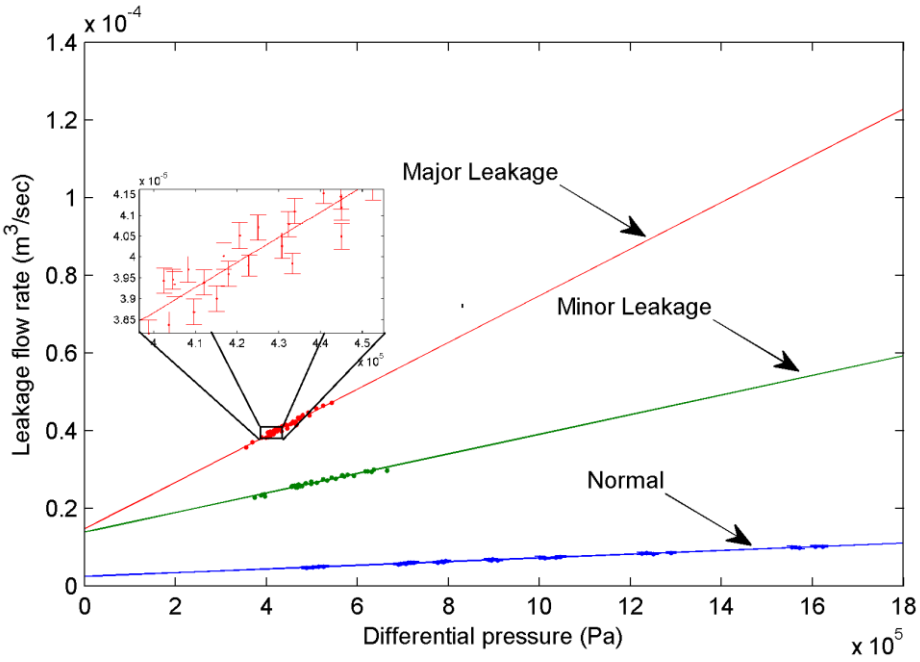

Figure 5-1: The flow rate vs. differential pressure

Figure 5-1 demonstrates leakage flow rate versus differential pressure at three different leakage conditions (normal, minor leakage, and major leakage). Each data set involves five trials to ensure sufficient data repeatability. The plot shows a linear relationship between the leakage flow rate and differential pressure that agrees with Eqn (5-8). A significant offset can be observed (with zero differential pressure) in minor and major leakage conditions.

The flow rate of an orifice can be modeled as:

$$Q = C_d A \sqrt{\frac{2}{\rho}|\Delta P|} * sgn(\Delta P) \tag{5-9}$$

where ρ stands for fluid density. A is the orifice flow area and C_d is the discharge coefficient, the value of which depends on orifice geometry [**43**]. According to Eqn (5-9), the orifice flow rate Q is proportional to the square root of the pressure difference between the two sides of the orifice (ΔP). As observed in Figure 5-1, the leakage flow

model can be linearized as in Eqn (5-8) with an offset Q_{L0} within the prototype's operating region.

$$Q_L = D_p\omega_p - A\dot{x} = L_t(P_1 - P_2) + Q_{L0} \tag{5-10}$$

A linear trend line is obtained for each data set by using least square fit. The slope and interception correspond to the overall leakage coefficient L_t and offset Q_{L0} for the appropriate leakage condition.

Table 5-2: Leakage coefficients and flow rates

Condition	**Leakage Coefficient (L_t)**	**Flow Rate (Q_{L0})**
Normal	$4.784 \times 10^{-12}\ m^3/(s * Pa)$	$2.413 \times 10^{-6}\ m^3/s$
Minor Leakage	$2.523 \times 10^{-11}\ Pa\ m^3/(s * Pa)$	$1.382 \times 10^{-5}\ m^3/s$
Major Leakage	$6.006 \times 10^{-11}\ Pa\ m^3/(s * Pa)$	$1.465 \times 10^{-5}\ m^3/s$

5.2.2 Friction Model and Friction Coefficient

In this study, the EHA is not connected to any external load. However, this is recommended for future studies. The actuator output force is governed by the following:

$$F = (P_1 - P_2)A = M\ddot{x} + F_f \tag{5-11}$$

where M denotes actuating mass, where in this case it is $7.376\ kg$ [**3**]. F_f is the actuator friction which can be formulated as a second-order quadratic function related to the actuator velocity $\dot{x}$ [**25**]:

$$F_f = a_2\dot{x} + (a_1\dot{x}^2 + a_3)sgn(\dot{x}) \quad (5\text{-}12)$$

At steady state, the acceleration of the actuator becomes zero. Substituting Eqn (5-12) and $\ddot{x} = 0$ in (5-11) yields the following :

$$(P_1 - P_2)A = a_2\dot{x} + (a_1\dot{x}^2 + a_3)sgn(\dot{x}) \quad (5\text{-}13)$$

To determine the friction coefficients (a_1, a_2, a_3) experiments were performed with various pump speeds, ranging from 15.58 rad/sec (150 RPM) to 109.0 rad/sec (1050 RPM). The steady state velocity and differential pressures were measured. Figure 5-2 demonstrates differential pressure versus actuator velocity regarding three friction conditions (normal, minor friction, and major friction) defined in section 4.3.2. Each data set involves 4 trials for data repeatability. By fitting parabolic curves into these data points, three friction models can be extracted with coefficients listed in the Table 5-3.

Table 5-3: Friction coefficients

Condition	a_1	a_2	a_3
Normal	6.589×10^4	2.144×10^3	436
Minor Friction	1.162×10^6	-7.440×10^3	500
Major Friction	4.462×10^6	1.863×10^4	551

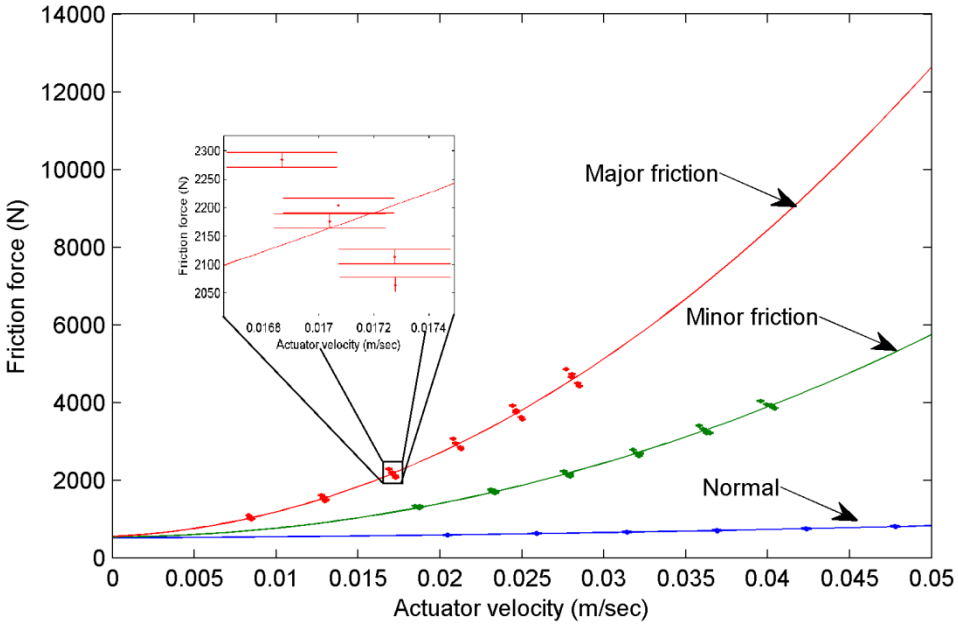

Figure 5-2: Differential pressure vs. actuator velocity

Substituting Eqn (5-12) in (5-11) and rearranging yields:

$$P_1 - P_2 = \frac{M}{A}\ddot{x} + \frac{a_2}{A}\dot{x} + \frac{a_1\dot{x}^2 + a_3}{A}sgn(\dot{x}) \tag{5-14}$$

With an linearized leakage model as Eqn (5-10), the system model (5-7) is modified as follows:

$$D_p\omega_p = A\dot{x} + \frac{V_0}{\beta}\left(\frac{dP_1}{dt} - \frac{dP_2}{dt}\right) + L_t(P_1 - P_2) + sgn(P_1 - P_2)Q_{L0} \tag{5-15}$$

Eqn (5-14) is differentiated to obtain $\frac{dP_1}{dt} - \frac{dP_2}{dt}$ in Eqn (5-15). However, since the sign function $sgn(\dot{x})$ is not continuous when $\dot{x} = 0$, $\frac{dP_1}{dt} - \frac{dP_2}{dt}$ is defined conditionally as follows:

$$if\ \dot{x} > 0 \tag{5-16}$$

$$\frac{dP_1}{dt} - \frac{dP_2}{dt} = \frac{M}{A}\dddot{x} + \frac{a_2}{A}\ddot{x} + \frac{2a_1\dot{x}\ddot{x}}{A}$$

$if\ \dot{x} = 0$

$$\frac{dP_1}{dt} - \frac{dP_2}{dt} = \frac{M}{A}\dddot{x} + \frac{a_2}{A}\ddot{x}$$

$if\ \dot{x} < 0$

$$\frac{dP_1}{dt} - \frac{dP_2}{dt} = \frac{M}{A}\dddot{x} + \frac{a_2}{A}\ddot{x} - \frac{2a_1\dot{x}\ddot{x}}{A}$$

which has the same effect as:

$$\frac{dP_1}{dt} - \frac{dP_2}{dt} = \frac{M}{A}\dddot{x} + \frac{a_2}{A}\ddot{x} + \frac{2a_1\dot{x}\ddot{x}}{A}sgn(\dot{x}) \tag{5-17}$$

Substituting Eqn (5-14), (5-18) to (5-15) and rearranging yields a nonlinear mathematical model of EHA as:

$$\begin{aligned} D_p\omega_p - sgn(P_1 - P_2)Q_{L0} \\ = \frac{MV_0}{A\beta}\dddot{x} + \frac{a_2V_0 + M\beta L_t}{A\beta}\ddot{x} + \frac{A^2 + a_2L_t}{A}\dot{x} \\ + \frac{2a_1V_0\dot{x}\ddot{x} + \beta L_t(a_1\dot{x}^2 + a_3)}{A\beta}sgn(\dot{x}) \end{aligned} \tag{5-18}$$

5.2.3 EHA Model

In order to implement the nonlinear model for state or parameter estimation, Eqn (5-17) is converted into a discrete-time state space format. The input is defined as $u = D_p\omega_p - sgn(P_1 - P_2)Q_{L0}$. The discrete state space model is defined as follows:

$$x_{1,k+1} = x_{1,k} + Tx_{2,k}$$

$$x_{2,k+1} = x_{2,k} + Tx_{3,k}$$

$$\begin{aligned} x_{3,k+1} = &\left[1 - T\frac{a_2V_0 + M\beta L_t}{MV_0}\right]x_{3,k} - T\frac{(A^2 + a_2L_t)\beta}{MV_0}x_{2,k} \\ &- T\frac{2a_1V_0x_{2,k}x_{3,k} + \beta L_t\left(a_1x_{2,k}^2 + a_3\right)}{MV_0}sgn\left(x_{2,k}\right) \\ &+ T\frac{A\beta}{MV_0}u_k \end{aligned} \tag{5-19}$$

where $x_1, x_2, and\ x_3$ are the actuator states position, velocity and acceleration respectively.

5.2.4 Effective Bulk Modulus

In ideal cases, hydraulic fluid is considered as incompressible. With the presence of air (e.g., trapped air bubble) fluid becomes compressible, causing loss of energy and compromising stability. The effective bulk modulus parameter β is a measure of the fluid compressibility. Its value is extremely difficult to determine experimentally since the volume of trapped air is unpredictable. In such cases, the popular Extend Kalman Filter (EKF) may be used with the mathematical model obtained in Section 5.2.3 to estimate the effective bulk modulus [**25**]. In an effort to implement the EKF, the model is transformed into the following state space equations.

$$x_{1,k+1} = x_{1,k} + Tx_{2,k} \tag{5-20}$$

$$x_{2,k+1} = x_{2,k} + Tx_{3,k} \tag{5-21}$$

$$x_{3,k+1} = \left[1 - T\frac{a_2V_0 + ML_tx_{4,k}}{MV_0}\right]x_{3,k} - T\frac{A^2 + a_2L_t}{MV_0}x_{4,k}x_{2,k} - T\left[\frac{2a_1V_0x_{2,k}x_{3,k}}{MV_0} + \frac{\left(a_1x_{2,k}^2 + a_3\right)L_t}{MV_0}x_{4,k}\right]sgn\left(x_{2,k}\right) + T\left[\frac{Au_k}{MV_0}x_{4,k}\right] \quad (5\text{-}22)$$

$$x_{4,k+1} = x_{4,k} \quad (5\text{-}23)$$

where the states are actuator position, velocity, acceleration and effective bulk modulus respectively. With measurement chosen as the actuator position, the measurement matrix becomes

$$C_{sys} = [1 \quad 0 \quad 0 \quad 0] \quad (5\text{-}24)$$

The linearized model is calculated as

$$F_{sys}(k) = \varphi(k) = \frac{\partial f\left(x(k)\right)}{x(k)} = \begin{bmatrix} \varphi_{11}(k) & \varphi_{12}(k) & \varphi_{13}(k) & \varphi_{14}(k) \\ \varphi_{21}(k) & \varphi_{22}(k) & \varphi_{23}(k) & \varphi_{24}(k) \\ \varphi_{31}(k) & \varphi_{32}(k) & \varphi_{33}(k) & \varphi_{34}(k) \\ \varphi_{41}(k) & \varphi_{42}(k) & \varphi_{43}(k) & \varphi_{44}(k) \end{bmatrix} \quad (5\text{-}25)$$

the parameters of which is calculated by

$$\varphi_{11}(k) = 1;\ \varphi_{21}(k) = T;\ \varphi_{31}(k) = 0;\ \varphi_{41}(k) = 0;\ \varphi_{21}(k) = 0;\ \varphi_{22}(k) = 1;$$

$$\varphi_{23}(k) = T;\ \varphi_{24}(k) = 0; \varphi_{31}(k) = 0;$$

$$\varphi_{32}(k) = -Tsgn\left(x_{2,k}\right)\left(\frac{2a_1x_{3,k}}{M} + \frac{2a_1L_tx_{2,k}x_{4,k}}{MV_0}\right) - T\frac{A^2 + a_2L_t}{MV_0}x_{4,k};$$

$$\varphi_{33}(k) = 1 - T\frac{2a_1}{M}x_{2,k}sgn\left(x_{2,k}\right) - T\frac{a_2V_0 + L_tMx_{4,k}}{MV_0};$$

$$\varphi_{34}(k) = T\frac{Au_k}{MV_0} - T\frac{x_{2,k}(A^2 + a_2L_t)}{MV_0} - T\frac{L_t}{V_0}x_{3,k} - T\frac{L_t\left(a_1x_{2,k}^2 + a_3\right)}{MV_0}sgn\left(x_{2,k}\right);$$

$$\varphi_{41}(k) = 0;\ \ \varphi_{42}(k) = 0;\ \ \varphi_{43}(k) = 0;\ \varphi_{44}(k) = 1;$$

T is the sampling time with value of 0.1 ms. Note that the system and measurement noise covariance matrices were defined respectively as:

$$Q = diag(1 \times 10^{-12}\ \ 1 \times 10^{-8}\ \ 1 \times 10^{-6}\ \ 1 \times 10^{-12}) \tag{5-26}$$

$$R = diag(1 \times 10^{-12}) \tag{5-27}$$

To estimate the effective bulk modulus, the testing input was chosen as a sinusoidal wave with 124.6 rad/sec amplitude and 10 Hz frequency. A priori information such as initial value of the estimating states and parameters must be provided for EKF process. The initial position, velocity, and acceleration were assumed as zero. The bulk modulus estimation process was run with different initial effective bulk modulus (with values from 0 Pa to 5×10^8 Pa) to see if different initial values affected the final estimation. The estimation results are plotted in Figure 5-3.

In subplot 1, the position estimation (green line) followed the corresponding experimental measurement (blue line) within acceptable limits. In subplot 2, the effective bulk modulus estimations with different initial values converged to the same value after approximately 7 ms and reached steady state value (2.07×10^8 Pa) after 1 sec. The subplot 3 demonstrates the rank number of local observability is constantly 4 which equals to the number of states (position, velocity, acceleration and effective bulk modulus). The system was therefore considered as observable during the whole process. The bulk modulus values converged to the same value 2.08×10^8 Pa which agrees with the bulk modulus value 2.1×10^8 Pa obtained in [**25**].

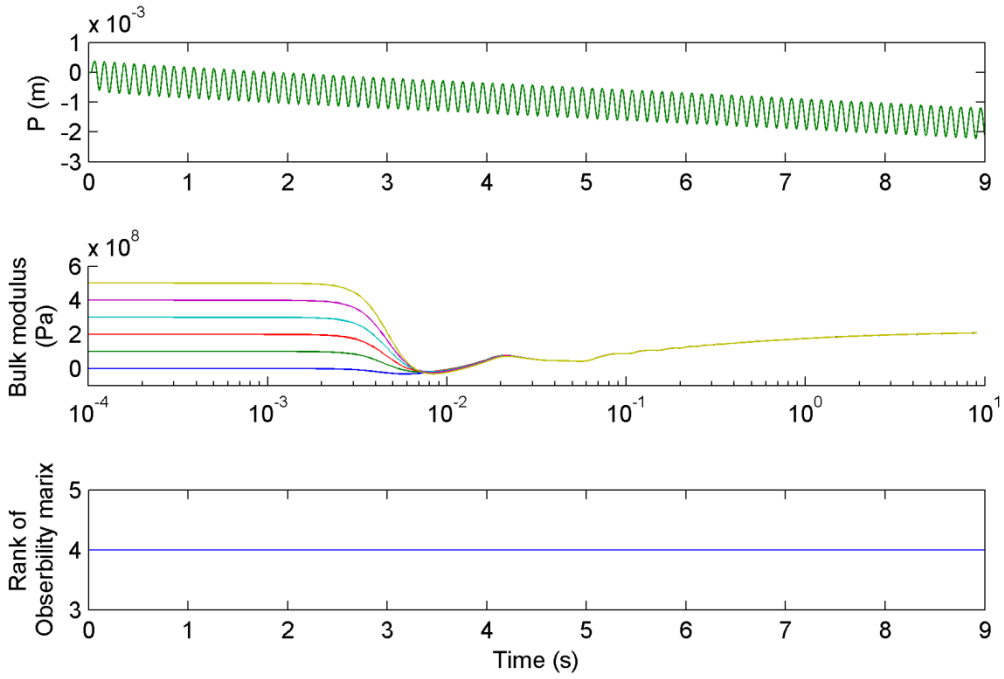

Figure 5-3: Effective bulk modulus estimation

5.3 The Parametric EHA Model

5.3.1 System Identification Introduction

System identification is a fast and accurate technique used to obtain empirical parametric models for dynamic systems. The quality of models depends on measurement accuracy and prior knowledge. Compared to physical models derived mathematically, the identified parametric model is obtained: quickly, predictably, and typically more accurately [**44**]. Note that system identification does not require a full knowledge of the system, and can be universally used in various fields. However, the method is not without its drawbacks: (i) system identification requires access to the system, such that special signals -such as pseudo random binary signals (PRBS) and chirp signals- can be applied; (ii) the input and output must be measurable; (iii) parameters in parametric models do not directly translate to the physical parameters of the target system. In this research, system

identification strategies were applied on the Electro-Hydrostatic Actuator prototype in an effort to obtain models of the nine working conditions defined in Table 4-3.

In general, system identification techniques consist of three main steps:

1. A series of initial tests are applied on the target system for gathering preliminary information which helps the signal collection process design.
2. The target system is operated with input signals designed in step 1. The system output is measured with signal processing performed to remove unwanted noise.
3. Models are estimated based on the input-output data set, and prior knowledge of the system. Models are also validated with experimental data.

These steps may need to be repeated until an accurate model is obtained.

5.3.2 Initial Tests

Initial tests are implemented to obtain preliminary information on the system. This information includes: system bandwidth, steady state gain, dead-zone, saturation, and linearity. The initial tests are required for designing the input signal for data collection.

In this case, the target system was the EHA prototype which can be considered as a single-input, single-output (SISO) system. An important consideration in system identification is that the input signal should have a flat power spectrum within the frequency range of interest. The input was firstly chosen as the angular velocity of the servo motor. Figure 5-4 demonstrates the motor velocity output with a chirp signal input from 0.1Hz to 60Hz. It was found that the motor response dampened significantly after 20Hz and failed to provide an even power spectrum for system identification.

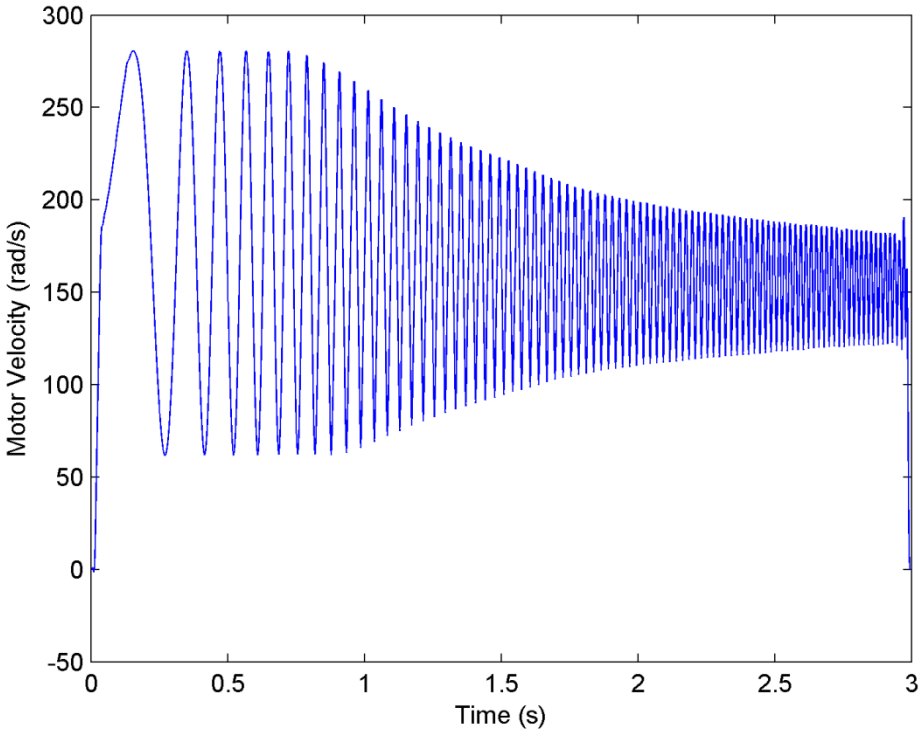

Figure 5-4: Motor Velocity with chirp signal

The motor voltage input with a range from -10 to 10 volt was chosen as the system input so that a flat power spectrum is achieved. An installed linear encoder provided actuator position measurement as output. According to [**3**], the EHA is a type 1, third order transfer function, defined by:

$$\frac{X(s)}{U(s)} = \frac{K_h \omega_{nh}^2}{s(s^2 + 2\xi_h \omega_{nh} s + \omega_{nh}^2)} \tag{5-28}$$

where the input $U(s)$ is known and the output $X(s)$ is measureable. ω_{nh} and ξ_h stand for system natural frequency and damping ratio, respectively. Since in system identification a type zero system is preferred, the output was replaced by the actuator velocity which was derived by differentiating actuator position [**3**].

5.3.2.1 Dead-zone test

The first test was performed to determine the EHA's dead-zone. A 0.5 Hz sinusoidal signal with an amplitude of 124.6 rad/sec (1200 RPM) was fed as the input. As an example, the response of the EHA operating with a major leakage fault condition is plotted in Figure 5-5.

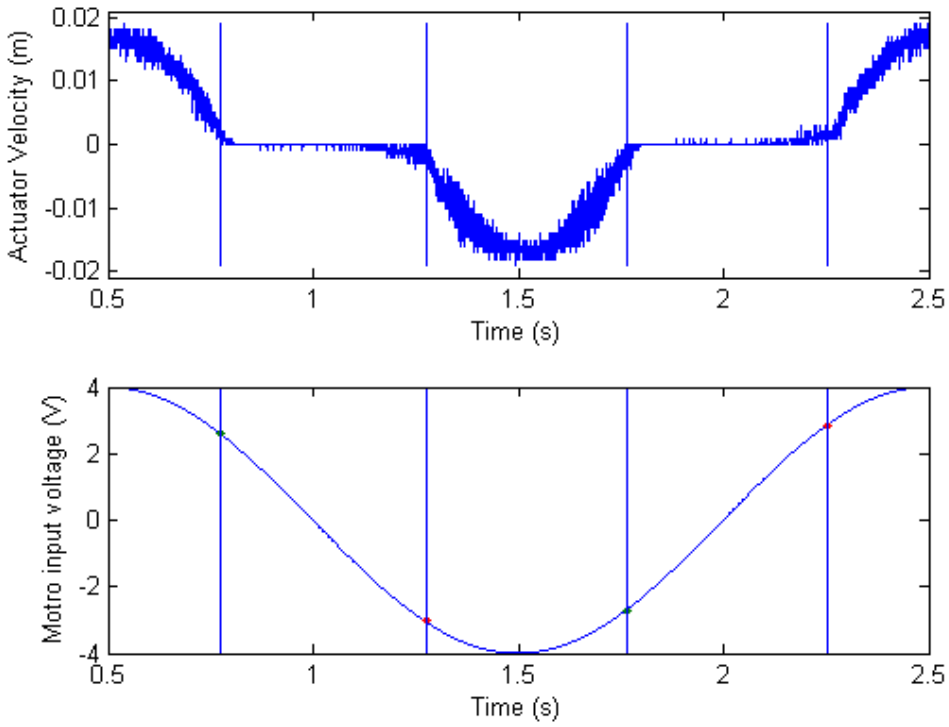

Figure 5-5: Dead-band test of Major Leakage EHA

Two zero velocity regions may be observed from the actuator response. The corresponding range of motor voltage input was considered as the dead-zone of the EHA. Ten measurements for each operating condition were made in an effort to verify repeatability. Their mean values are listed respectively in Table 5-4.

Table 5-4: Dead-band of all operating conditions

Operating condition	Dead-zone width (V)	Standard deviation
Normal	0.5421	0.0892
Minor Leakage	3.0479	0.0573
Major Leakage	5.6068	0.0691
Minor Friction	0.6583	0.0544
Major Friction	0.6696	0.0712
Minor Leakage Minor Friction	3.7531	0.0759
Minor Leakage Major Friction	3.8129	0.0736
Major Leakage Minor Friction	5.4352	0.1322
Major Leakage Major Friction	5.5735	0.1408

5.3.2.2 Steady-state gain test

The steady-state gain provides important system information such as: the linearity range, dead-zone, and saturation. In order to observe the steady-state gain, the EHA was run at various constant voltage input values. The input amplitudes were chosen from ±0.5 V to ±9 V.

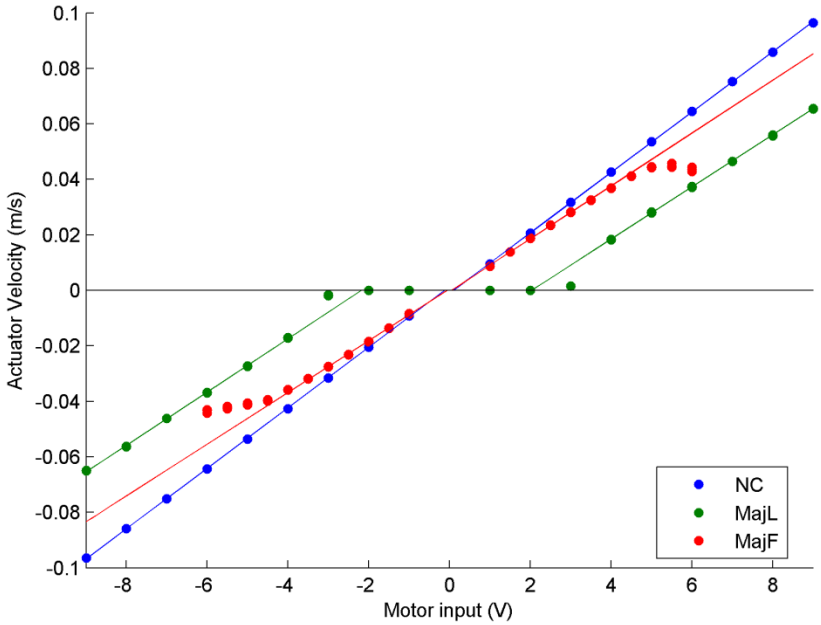

Figure 5-6: Steady state gain test results for normal, major leakage and major friction condition

Table 5-5: Steady state gain and bias of EHA

Operating condition	Steady state gain (m/s/V)	Offset (V)
Normal	0.0109	0.106
Minor Leakage	0.0098	1.4118
Major Leakage	0.0094	2.1060
Minor Friction	0.0102	0.999
Major Friction	0.0095	0.0525

Minor Leakage Minor Friction	0.0077	1.4431
Minor Leakage Major Friction	0.0075	1.6585
Major Leakage Minor Friction	0.0073	2.3247
Major Leakage Major Friction	0.0066	2.4640

Figure 5-6 demonstrates the steady-state response of the EHA operated under normal, major leakage, and major friction conditions respectively. The slope is the steady-state gain of the system, and the offset value corresponds to the dead-zone. Both the steady-state gain and the offset of each operating condition are listed in Table 5-5. As shown in the figure, the actuator velocity is linearly proportional to motor voltage input. Note that the offset is found to be relatively small under the normal condition, and becomes significantly large with the presence of major leakage. These findings lead to a hypothesis that the dead-zone is caused or amplified by the internal leakage of the cylinder. For the system operated under the major friction fault, saturation may be observed when the input exceeds 4V. Saturation is caused by the pressure relief valve which is set to open when the differential pressure exceeds 500 Psi (3.447 MPa). As the actuator velocity increases, the differential pressure is built up to compensate the increasing friction. When the differential pressure reaches its limit, it results in velocity saturation.

System identification is applicable when the target system is operating in a piece-wise linear region. According to the steady-state gain test (described earlier), the EHA has dead-zone nonlinearity that grows and becomes significant as the leakage level increases. There is also saturation nonlinearity with the presence of friction faults. A piece-wise linear regions is observed for each working condition based on the steady-state gain test. The EHA should be operated within the regions listed in Table 5-6 for system identification to be within a piecewise linear region and in order to avoid non-linearities.

Table 5-6: Piece-wise linear region

Operating condition	Piece-wise linear region (V)
Normal	$1-9$
Minor Leakage	$3-9$
Major Leakage	$4-9$
Minor Friction	$1-5$
Major Friction	$1-4$
Minor Leakage Minor Friction	$3-8$
Minor Leakage Major Friction	$3-7$
Major Leakage Minor Friction	$4-9$
Major Leakage Major Friction	$4-8$

5.3.2.3 Frequency range of interest test

The third test involved determining the frequency range of interest. The EHA frequency response was investigated by using an Empirical Transfer Function Estimation (ETFE). ETFE was obtained by taking the Fast Fourier transform (FFT) of the system output (actuator velocity) and dividing it by the FFT of the system input (input voltage) [**3**] [**44**]. The frequency range of interest was chosen to be from 0.1 Hz to the 10 times or 100 times of EHA bandwidth for the following two reasons.

1. Both leakage and friction conditions affect system performance at low frequency ranges.
2. The model accuracy at the system bandwidth frequency is critical for the closed-loop control performance [**44**].

The system bandwidth is defined as the frequency when the gain drops by 3dB. The ETFE requires an input with an even power spectrum along the frequency range of interest. In this case, the test signal was selected as a chirp signal, which is a series of sinusoidal curve with gradually increasing frequency. It had a frequency range of 0.1 to 60 Hz. The mean and amplitude of the signal (listed in Table 5-7) was selected to cover the piece wise linear region.

Table 5-7: Bandwidth test signal mean and amplitude

Operating condition	Mean (V)	Amplitude (V)
Normal	5	4
Minor Leakage	6	3
Major Leakage	6.5	2.5
Minor Friction	3	2
Major Friction	2.5	1.5
Minor Leakage Minor Friction	5.5	2.5
Minor Leakage Major Friction	5	2
Major Leakage Minor Friction	6.5	2.5

Major Leakage Major Friction	6	2

The ETFE of the EHA under normal condition is shown in Figure 5-7. The ETFE shown here is filtered with a 128-size Hamming window to give a cleaner curve.

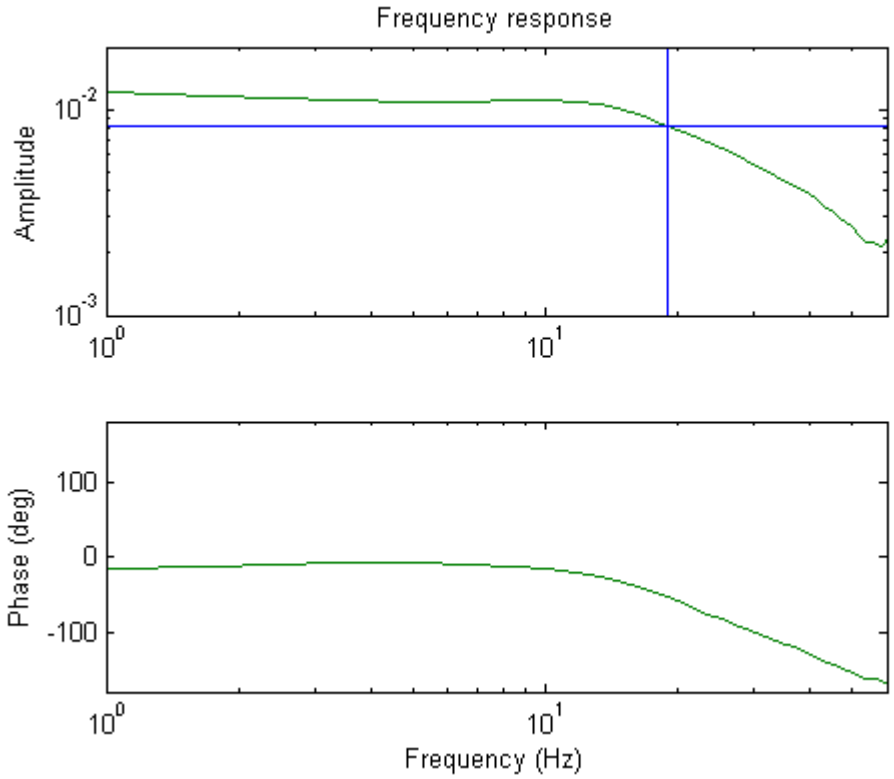

Figure 5-7: ETFE of normal condition

The amplitude curve has a 3dB drop at 19Hz, which is the bandwidth of the EHA operating under the normal condition. The process was repeated for all of the 8 fault conditions considered in Chapter 4. The observed bandwidths of all these operating conditions are listed in Table 5-8.

Table 5-8: Bandwidth of EHA

Operating condition	Bandwidth (Hz)
Normal	19
Minor Leakage	25
Major Leakage	30
Minor Friction	28
Major Friction	31
Minor Leakage Minor Friction	29
Minor Leakage Major Friction	30
Major Leakage Minor Friction	32
Major Leakage Major Friction	40

5.3.2.4 Input signal mean and amplitude test

After determination of bandwidths, the fourth test involved selection of the input signal mean and amplitude. In system identification, large input amplitudes are preferred for obtaining a better signal-to-noise ratio. However, the selected signal amplitude needs to stay within a piece-wise linear region of the system. The mean of the test signal should be chosen at the center of the piece-wise linear region to achieve the largest amplitude. Chirp signal with small amplitude falling within the linear region were chosen to verify the linearity using frequency response. The EHA performance can be considered as linear if it gives the same frequency response with different input means.

As an example, the piece-wise linear region was observed to be from 1 to 9V using the steady state gain test for EHA under normal condition. Seven test signals were chosen as chirp signals with means from 2 to 8V. All the signals had the same amplitude of 1V and

a frequency range three times the bandwidth. The corresponding ETFEs are plotted in Figure 5-8. It was found that all the seven ETFE's had the same shapes, proving that the EHA under normal condition had piece-wise linear region from 1 to 9 V. The same test was applied to the other eight working conditions and the test results verified the piece-wise linear region obtained in steady-state gain test. The operating point for each working condition was chosen as the center of the corresponding piece-wise linear region as listed in Table 5-9.

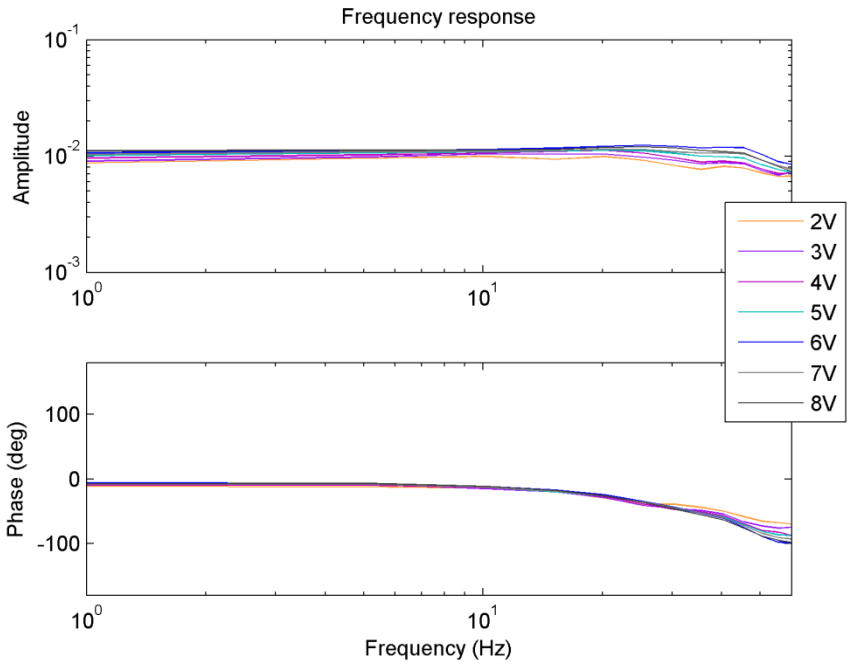

Figure 5-8: Mean test of EHA under normal condition

Table 5-9: EHA operation point

Operating condition	Operation point (V)
Normal	5
Minor Leakage	5.5
Major Leakage	6
Minor Friction	3
Major Friction	2.5
Minor Leakage Minor Friction	4.5
Minor Leakage Major Friction	4.5
Major Leakage Minor Friction	6
Major Leakage Major Friction	5.5

To ensure that the EHA's linearity was not affected by the change of amplitude, the EHA was tested by chirp signals with various amplitudes. The chirp signals had means at the selected operation points as listed in Table 5-9 and frequency range of 3 times of the system bandwidth as provided in Table 5-8. The amplitudes of the test signals varied within the piece-wise linear region. As an example, the inputs to the EHA under normal condition were chosen as chirp signals with mean of 5V and a frequency range of 0.1 to 60Hz. The amplitudes were chosen from 1 to 3.5V. The corresponding ETFEs are plotted in Figure 5-9.

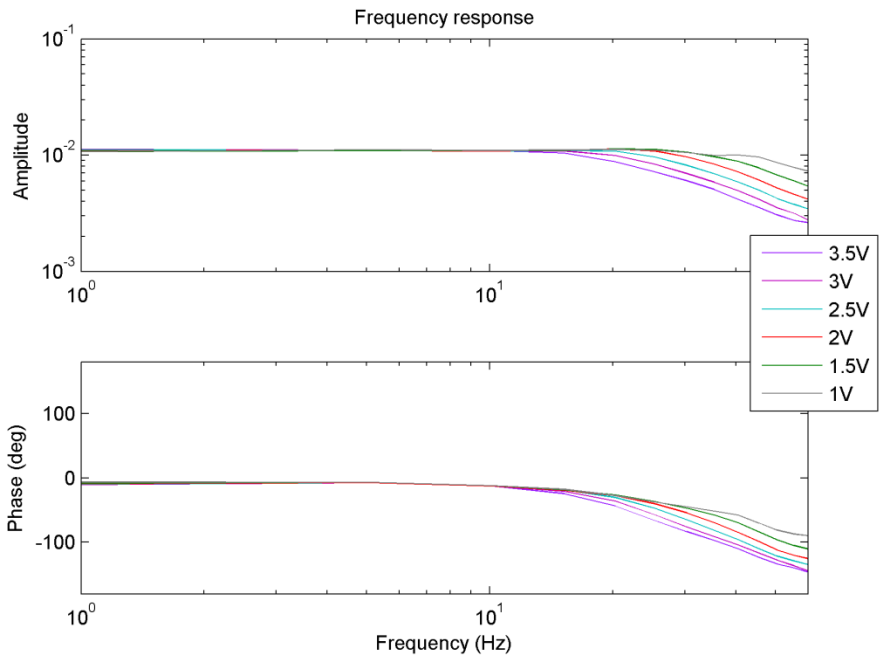

Figure 5-9: Amplitude test of EHA under normal condition

As shown in Figure 5-9, the bandwidth of the EHA under normal condition is significantly changed as the input amplitude increased from 1 to 3.5V. This finding indicates that the EHA is nonlinear as the amplitudes change. It requires multiple models to describe its dynamics properly. The same test was applied to the other eight working conditions and similar results were observed.

In order to demonstrate a complete system identification process and to test the accuracies of identified models, the maximum available amplitude within the piece-wise linear region observed in previous tests is chosen for each condition. They are listed in Table 5-10.

Table 5-10: Input amplitude for EHA system identification

Operating condition	Input amplitude (V)
Normal	3.5
Minor Leakage	3.5
Major Leakage	3
Minor Friction	2.5
Major Friction	2
Minor Leakage Minor Friction	2.5
Minor Leakage Major Friction	2.5
Major Leakage Minor Friction	3
Major Leakage Major Friction	2.5

5.3.2.5 System order test

The fifth test involved estimating the order of the system. Based on an analysis of the physical models, the EHA system was considered to be second-order type zero, with the actuator velocity as the output and the motor input voltage as the input. Two different techniques were implemented and compared in order to confirm this assumption of system order: (i) impulse response test, and (ii) using AutoRegressive models with eXternal input (ARX) .

The impulse response of the EHA was derived by differentiating the actuator's velocity to a step-input. A Hankel matrix was obtained and its corresponding singular values were computed by using singular value decomposition (SVD). The magnitudes of the singular values indicate the order of the EHA. Details of the Hankel matrix and SVD calculation may be found in [**45**] [**3**].

To determine the model order, another approach involved estimating a series of ARX models, with order ranging from 1 to 10. The ARX model has a relatively simple structure and is chosen for computational convenience. The error variance based on model prediction of the measurement from the system indicates which model order has the best fit. In the following figures, model order estimation of the EHA under normal conditions are presented. Figure 5-10 shows the impulse response results, and Figure 5-11 shows the results from the ARX models.

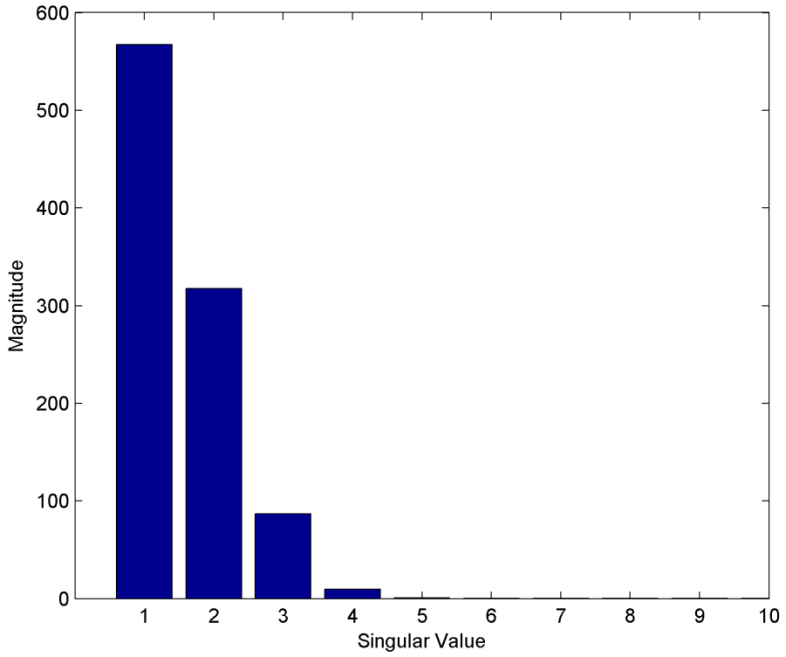

Figure 5-10: Model order estimation of normal condition (Impulse response)

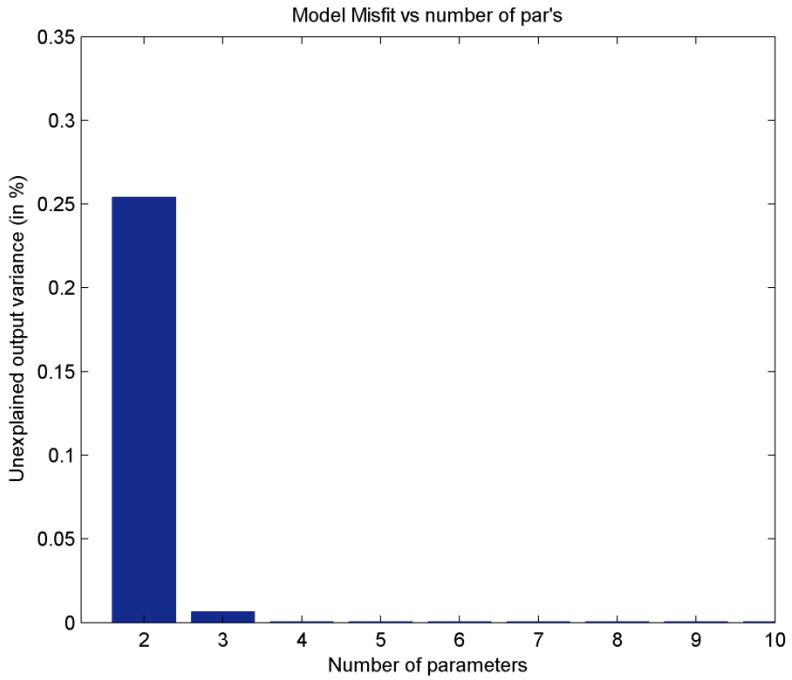

Figure 5-11: Model order estimation of normal condition (ARX model)

Figure 5-10 shows a significant magnitude drop between the singular values 1 past 3. This finding indicates that the dominant dynamics are second or third order, with negligible higher-order dynamics.

The result demonstrated in Figure 5-11 shows only one significant drop of variance between 2nd and 3rd order models. This finding indicates that the EHA has second-order dominant dynamics, which agrees with the mathematical analysis.

The same tests were performed on the EHA, operating under all of the nine conditions considered in Chapter 4. The results were nearly identical. The tests concluded that the EHA retains the same model structure and order, despite the presence of faults.

5.3.3 Data Collection and Processing

With the knowledge obtained from initial tests, the amplitude and frequency range for the inputs for system identification were selected. The test signals were chosen as pseudo-random binary signals (PRBS) with amplitude, mean and maximum frequency listed in

Table 5-11. A PRBS signal consists of sequential steps with a fixed amplitude. The amplitude toggles at a frequency that is ideally at least 10 times the system bandwidth. However, such a high frequency could not be applied to the EHA system due to the safety limitations of the Siemens motor. In this case, the upper bound of switching frequency was set as 3 times the EHA bandwidth.

Table 5-11: System identification test input design

Operating condition	Input amplitude (V)	Input mean (V)	Maximum frequency (Hz)
Normal	3.5	5	60
Minor Leakage	3.5	5.5	75
Major Leakage	3	6	90
Minor Friction	2.5	3	90
Major Friction	2	2.5	90
Minor Leakage Minor Friction	2.5	4.5	90
Minor Leakage Major Friction	2.5	4.5	90
Major Leakage Minor Friction	3	6	90
Major Leakage Major Friction	2.5	5.5	120

The ‘raw’ actuator velocity measurements included outliers, and a large amount of high-frequency noise. In order to remove the outliers, a data standard deviation was calculated. Outliers can be detected when the difference between the neighbouring data points is larger than a threshold based on the standard deviation. Once an outlier is detected, the value of the abnormal data point is replaced by the mean of its neighbours. This method was applied to the measurements from the EHA.

High-frequency noise was removed by using a 12th-order Butterworth low pass filter. The filter cut-off frequency was set 10% larger than the input frequency. Since the filtering brings a phase shift, a double-flipped technique was implemented to achieve zero-phase change. The measurement was flipped over and filtered again to remove phase shift. As an example, the test input and the corresponding output velocity of the EHA under the normal condition are plotted in Figure 5-12. In order to eliminate the effect of offset caused by the dead-zone of system, the test data was adjusted by removing the mean values. The adjusted test data of the EHA under the normal condition are plotted in Figure 5-13.

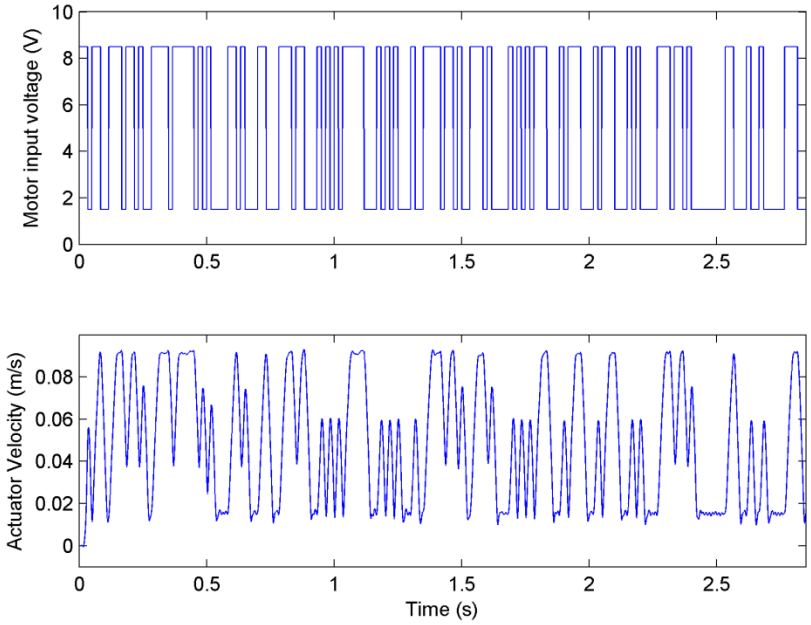

Figure 5-12: PRBS input signal and corresponding velocity output under normal condition

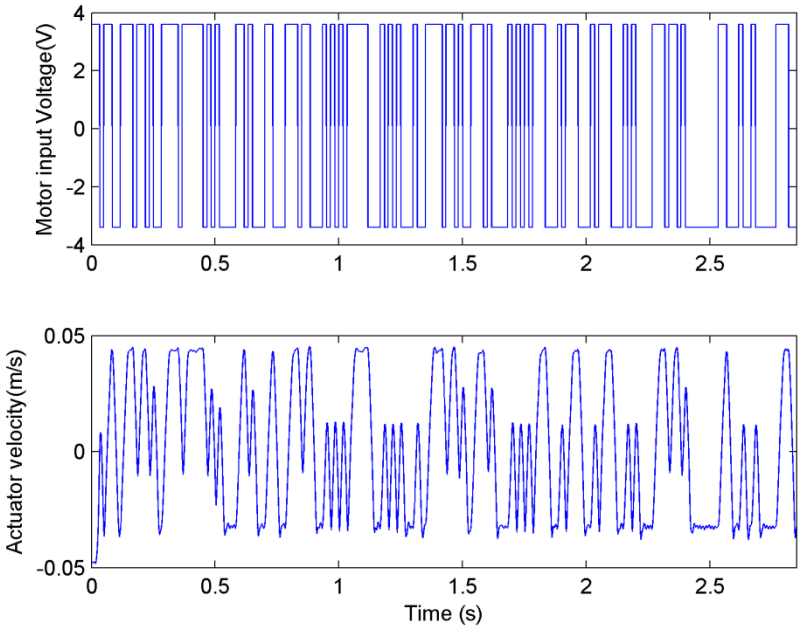

Figure 5-13: Adjusted measurements of normal condition

5.3.4 Model Estimation

In system identification, models are obtained by fitting different types of transfer functions. Four types of models are commonly used. They are the (i) AutoRegressive model with eXternal input (ARX), (ii) the AutoRegressive Moving Average model with eXternal input (ARMAX), (iii) Box-Jenkins (BJ), and (iv) Output Error (OE). Their corresponding structures and transfer functions are provided in Figures 4-12 to 4-15.

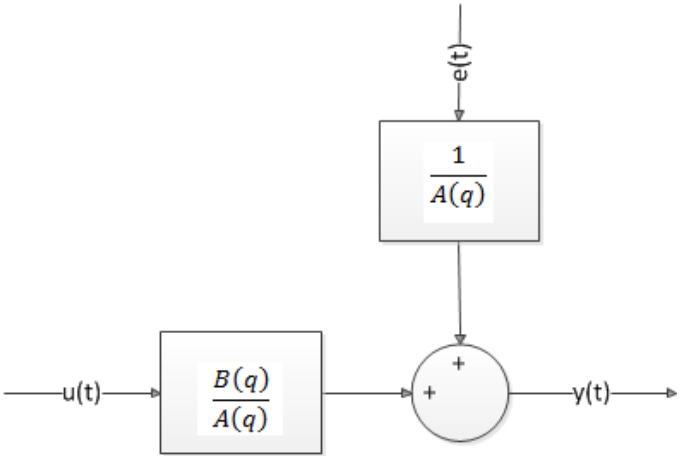

$$ARX\ transfer\ function: y(t) = \frac{B(q)}{A(q)}u(t) + \frac{1}{A(q)}e(t)$$

Figure 5-14: ARX model structure

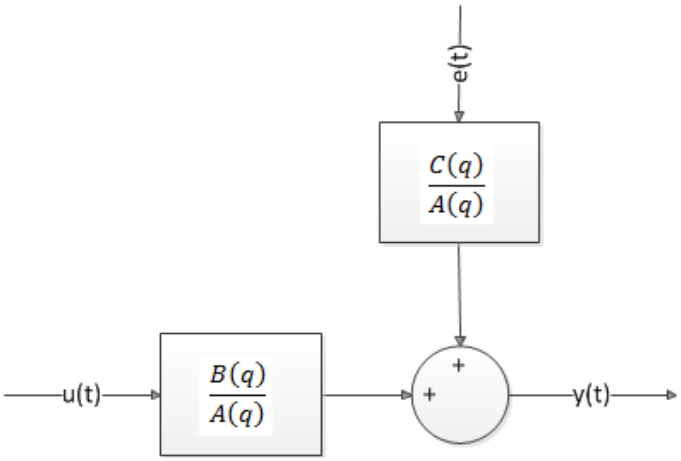

$$ARMAX\ transfer\ function: y(t) = \frac{B(q)}{A(q)}u(t) + \frac{C(q)}{A(q)}e(t)$$

Figure 5-15: ARMAX model structure

In ARX and ARMAX models, noise is assumed to go through a transfer function that has the same denominator ($A(q)$) as the system transfer function. The ARMAX provides extra flexibility by adding an extra nominator ($C(q)$) to the noise transfer function.

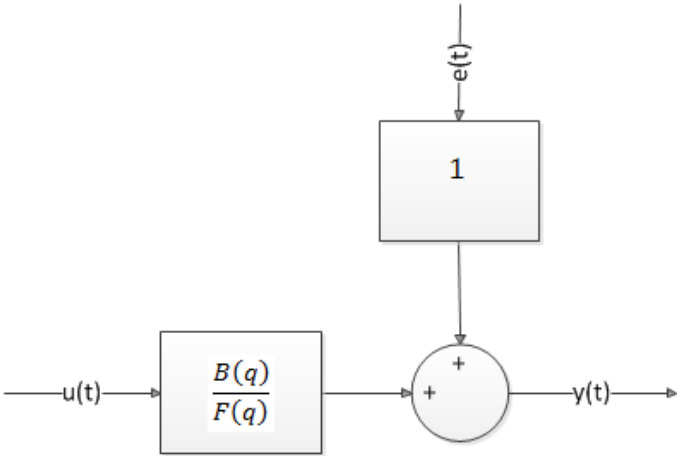

$$OE\ transfer\ function: y(t) = \frac{B(q)}{F(q)}u(t) + e(t)$$

Figure 5-16: OE model structure

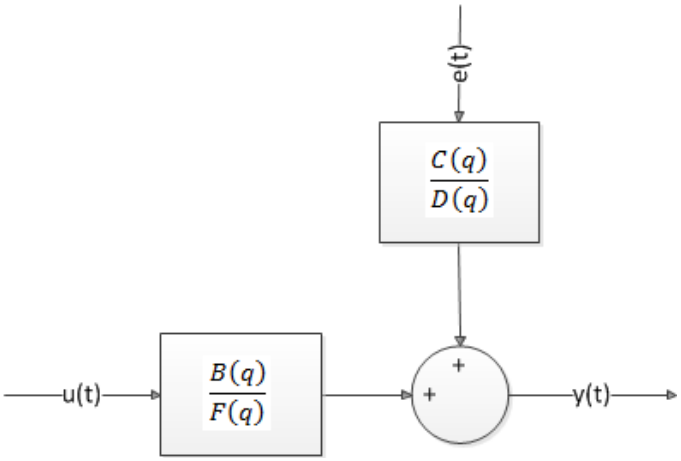

$$BJ\ transfer\ function: y(t) = \frac{B(q)}{F(q)}u(t) + \frac{C(q)}{D(q)}e(t)$$

Figure 5-17: BJ model structure

Both BJ and OE models have noise transfer function that is independent of the system transfer function. BJ offers full flexibility, since both the noise and the system transfer function have different denominators and numerators. Note that further information for these model structures may be found in [**3**] and [**45**]. In general, the BJ and OE structures provide better accuracies amongst these four strategies. In the case of the EHA, BJ and

OE showed the same level of accuracies according to experimental results. In order to minimize computation time, OE was selected. With a 3rd order OE model structure, models of the EHA operating under the nine working conditions were estimated and are listed in Table 5-12. Note that the system input and output were the motor input voltage and the actuator velocity, respectively.

Table 5-12: System identification models of EHA

Operating condition	Estimated Model
Normal	$\frac{5.698 \times 10^{-8} z^3}{z^3 - 2.963z^2 + 2.928z + 0.9644}$
Minor Leakage	$\frac{7.181 \times 10^{-8} z^3}{z^3 - 2.946z^2 + 2.894z + 0.9477}$
Major Leakage	$\frac{9.491 \times 10^{-8} z^3}{z^3 - 2.947z^2 + 2.895z + 0.9483}$
Minor Friction	$\frac{4.476 \times 10^{-7} z^3}{z^3 - 2.808z^2 + 2.623z + 0.8149}$
Major Friction	$\frac{3.671 \times 10^{-7} z^3}{z^3 - 2.872z^2 + 2.751z + 0.8782}$
Minor Leakage Minor Friction	$\frac{8.812 \times 10^{-7} z^3}{z^3 - 2.677z^2 + 2.369z + 0.6913}$
Minor Leakage Major Friction	$\frac{6.641 \times 10^{-7} z^3}{z^3 - 2.752z^2 + 2.514z + 0.7626}$
Major Leakage Minor Friction	$\frac{1.816 \times 10^{-6} z^3}{z^3 - 2.341z^2 + 1.714z + 0.3722}$
Major Leakage Major Friction	$\frac{3.956 \times 10^{-7} z^3}{z^3 - 2.872z^2 + 2.750z + 0.8783}$

5.4 Model Validation

Two models were obtained for each condition defined in Chapter 3. The first was a physical model, which was mathematically derived. The second was a parametric model found through the aforementioned system identification process. In this section, the accuracies of these two sets of models are tested through validataion.

5.4.1 Physical model validation

In order to find the accuracy of physical models, a sequential step signal was chosen for model validation. The absolute amplitudes of the steps were randomly selected between 77.88 to 124.6 rad/sec. The input direction switched every second as shown in Figure 5-18.

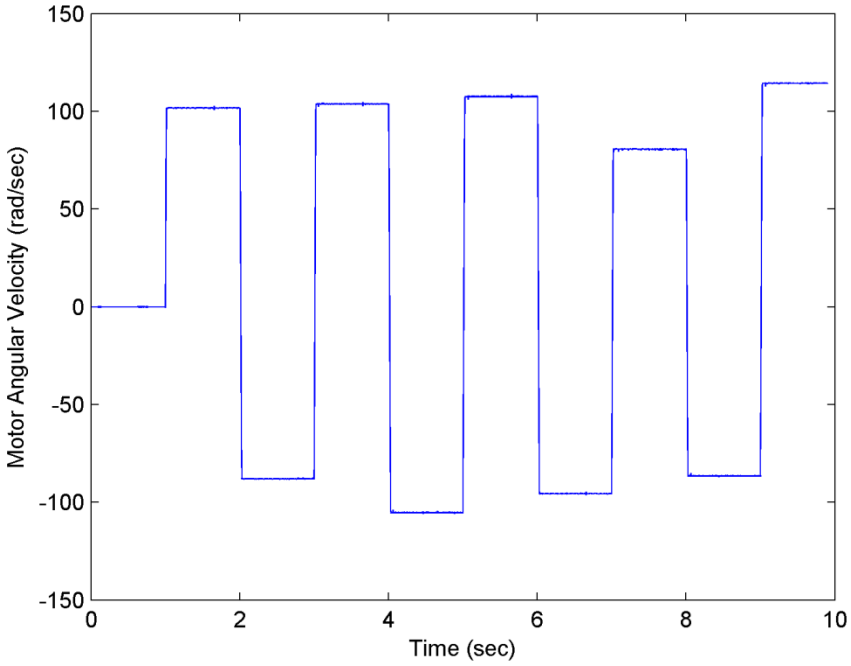

Figure 5-18: Physical model validation input

To test model quality, the root mean square error (RMSE) was calculated based on the actuator velocity measurement compared to its predicted value obtained from physical models. The results are shown in Figure 5-19 to Figure 5-24.

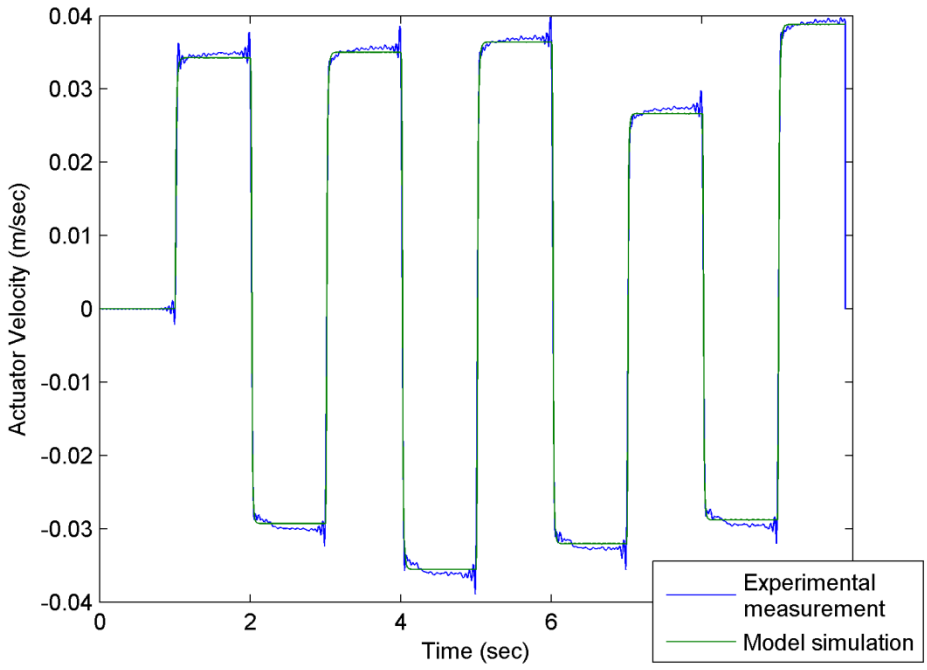

Figure 5-19: Physical model simulation at normal condition

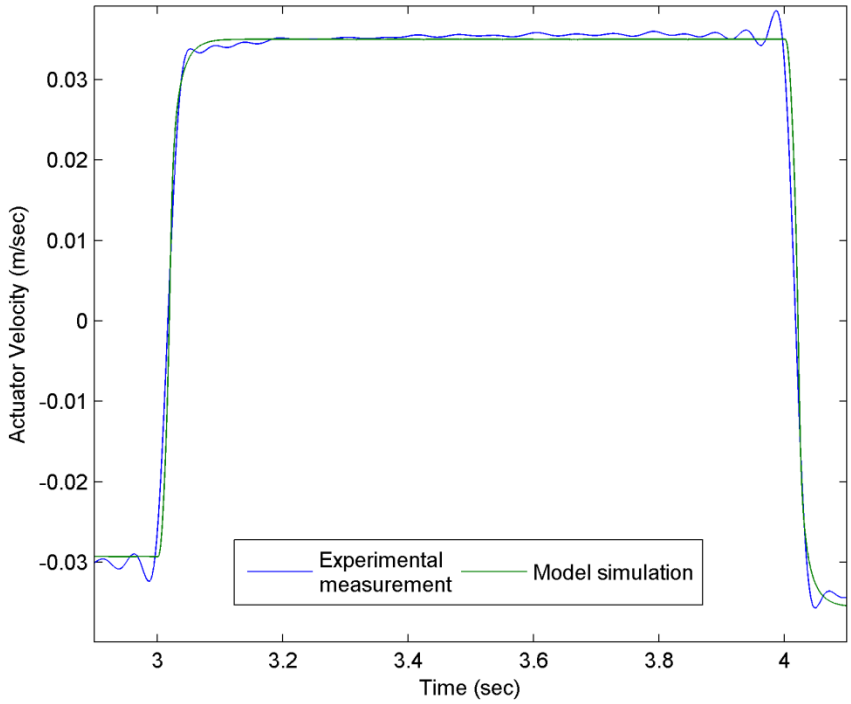

Figure 5-20: Physical model simulation at normal condition (amplified)

Figure 5-19 demonstrates the physical model simulated under normal condition with corresponding velocity measurement. Figure 5-20 shows the amplified view between the 3rd and 4th second. According to the figures, the physical model of the normal condition had good fit with the experimental measurement.

When the EHA operated under friction-only faults, the physical models provided an accurate performance at steady state. The model simulation of the EHA under major friction is plotted in Figure 5-21 and Figure 5-22.

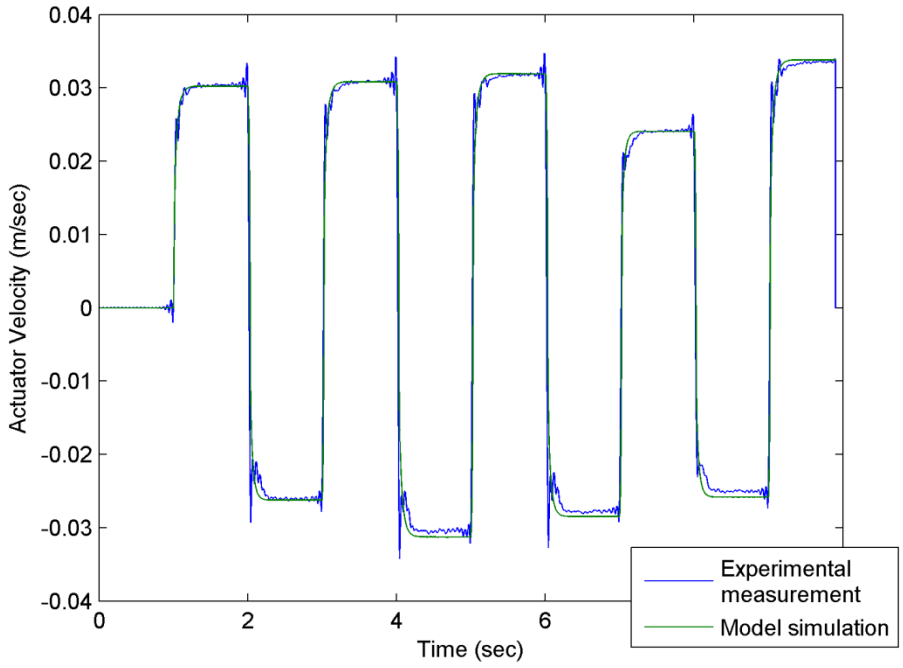

Figure 5-21: Physical model simulation at major friction condition

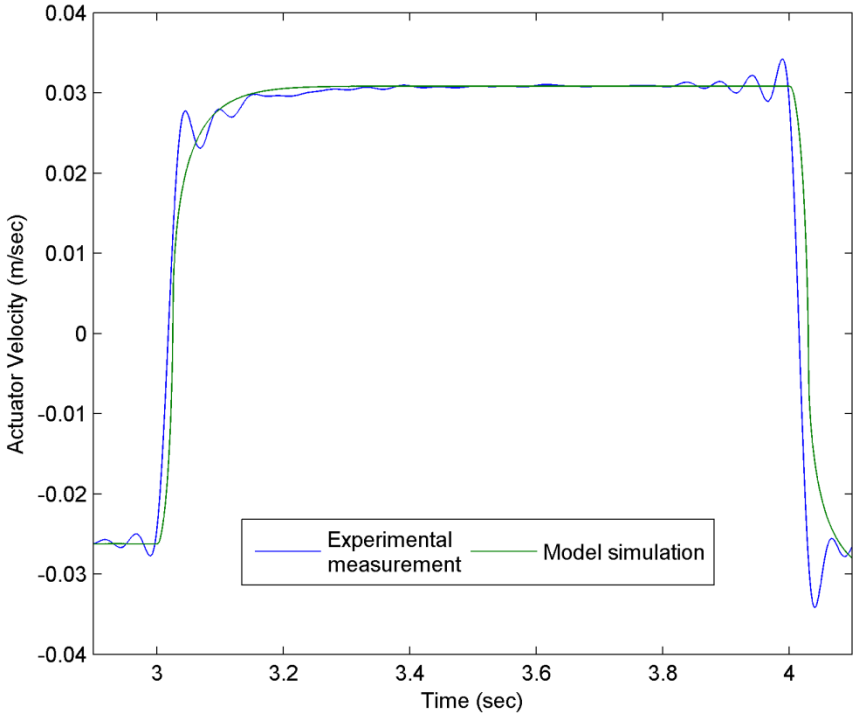

Figure 5-22: Physical model simulation at major friction condition (amplified)

When the EHA was operating under the leakage fault conditions, the physical model accurately predicted the steady-state region. However, a noticeable offset was observed between 7th and 9th second (highlighted red in Figure 5-23). The offset is believed to have been caused by the nonlinear leakage in EHA when it operated close to the dead-zone. Recall the linear leakage model obtained in section 5.2.1 that it is applicable within the pressure range demonstrated in Figure 5-1. With input close to the system dead-zone, the operating pressure may drop below the linear region, therefore the linear leakage model becomes incorrect and results in prediction offset. The performance of the physical model under the major leakage condition is demonstrated in Figure 5-23 and Figure 5-24.

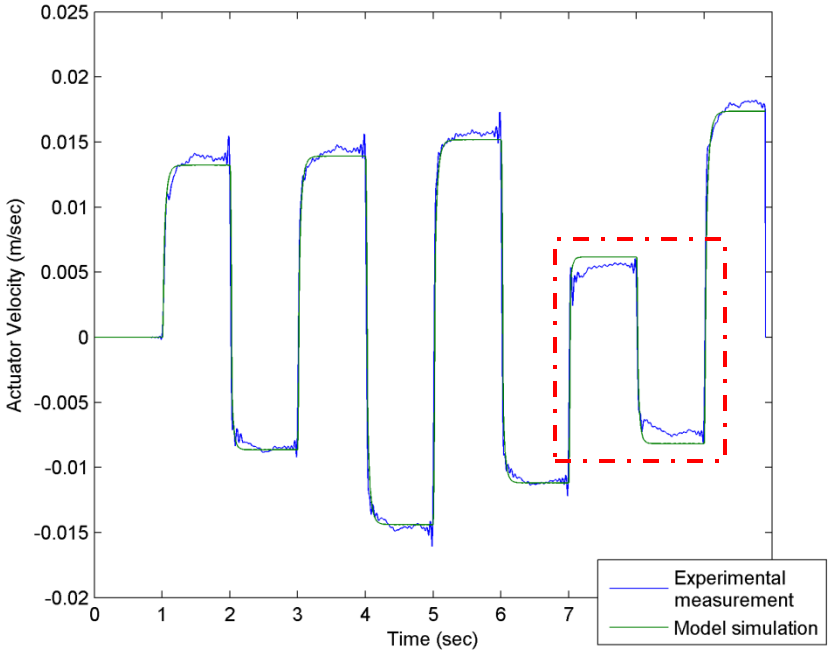

Figure 5-23: Physical model simulation at major leakage condition

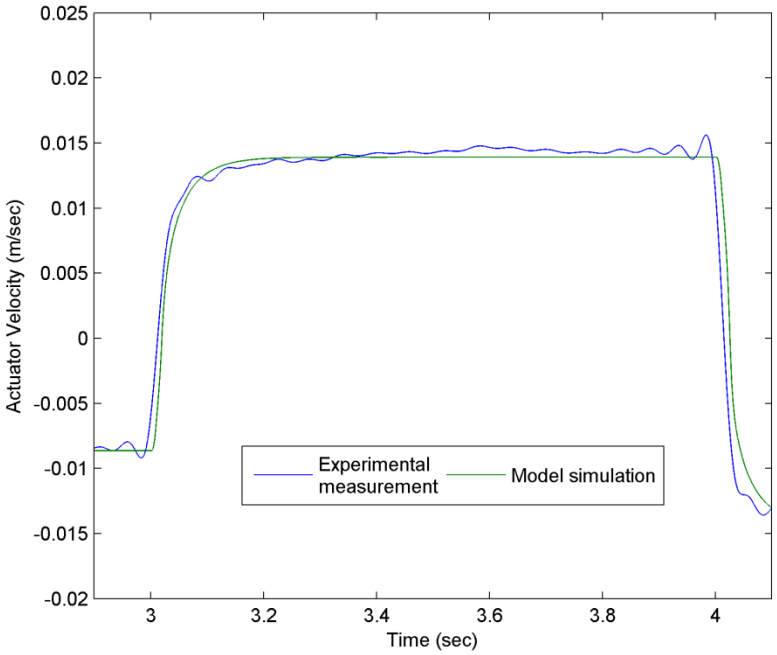

Figure 5-24: Physical model simulation at major leakage condition (amplified)

To qualify modeling accuracy, the RMSE was calculated (based on the velocity comparison) for each model as listed in Table 5-13.

Table 5-13: RMSE of mathematical models

Operation condition	RSME (m/sec)
Normal	0.0015
Minor Leakage	0.0011
Major Leakage	0.0012
Minor Friction	0.0023
Major Friction	0.0024
Minor L. Minor F.	0.0013
Minor L. Major F.	0.0022
Major L. Minor F.	7.7194e-004
Major L. Major F.	9.1800e-004

According to the calculated RMSE, the physical models offered accurate simulations of the EHA dynamics under all nine working conditions.

5.4.2 Identified parametric model validation

In order to determine the accuracy of identified parametric models, PRBS signals were chosen for model validation. The signals amplitudes, means and maximum frequencies are listed in Table 5-14.

Table 5-14: System identification validation signals

Operating condition	Input amplitude (V)	Input mean (V)	Maximum frequency (Hz)
Normal	3.5	5	20
Minor Leakage	3.5	5.5	25
Major Leakage	3	6	30
Minor Friction	2.5	3	30
Major Friction	2	2.5	30
Minor Leakage Minor Friction	2.5	4.5	30
Minor Leakage Major Friction	2.5	4.5	30
Major Leakage Minor Friction	3	6	30
Major Leakage Major Friction	2.5	5.5	40

Note that the test data used for system identification was adjusted to remove the offset in Section 5.3.3. Similar to the physical model validation, the RMSE based on the actuator velocity comparison was calculated to indicate the accuracies of identified parametric models. The prediction from the identified parametric model under the normal condition compared to the measurement is shown in Figure 5-25.

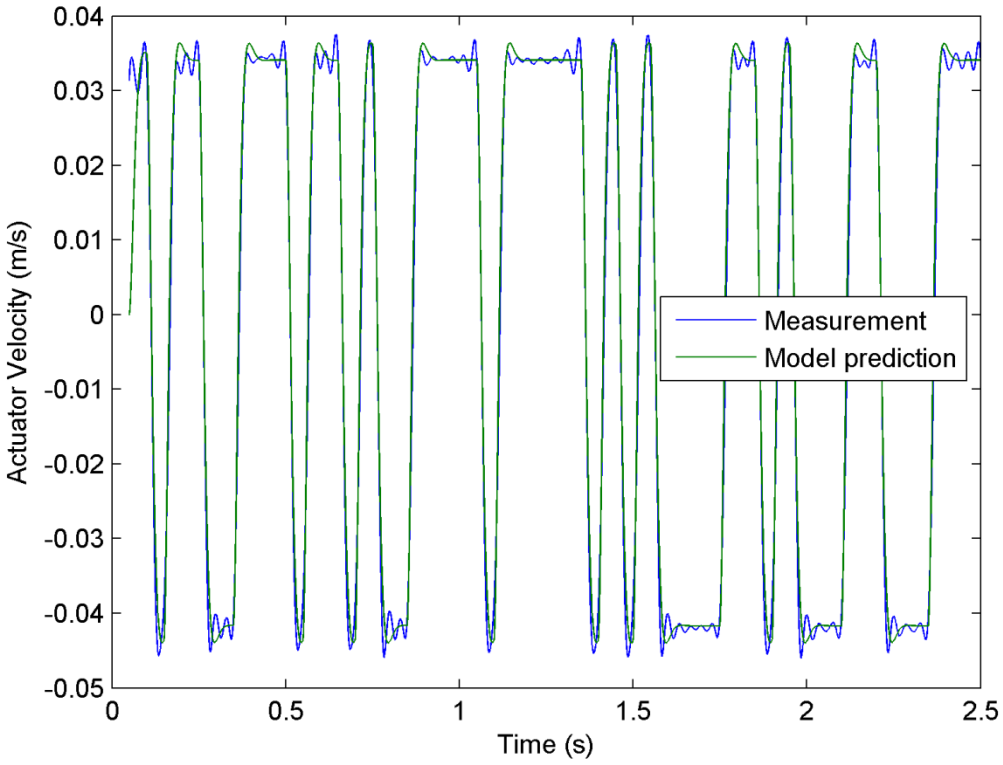

Figure 5-25: Identified parametric model simulation at normal condition

As shown in the figure, the identified model prediction agreed with the measurement well. The RMSE values of the validations are listed in Table 5-15.

Table 5-15: RMSE of parametric models

Operation condition	RSME (m/sec)
Normal	0.0023
Minor Leakage	0.0021
Major Leakage	0.0025
Minor Friction	0.0016
Major Friction	0.0014

Minor L. Minor F.	0.0011
Minor L. Major F.	0.0013
Major L. Minor F.	0.0016
Major L. Major F.	0.0012

5.5 Conclusion

Two types of models were obtained for the EHA for the nine working conditions defined in Chapter 3. The first type was a physical model derived mathematically. Parameters in the physical model have physical meanings and therefore provide a mechanism for understanding the dynamic effects in the system. For comparison, parametric models were also obtained experimentally through system identification.

Model validation results show that the parametric models and physical models have comparable prediction accuracies. According to the amplitude test results in Section 5.3.2.4, the EHA was found to have multiple piece-wise linear regions as the amplitudes change and therefore a large number of models were required to completely describe the system dynamics. As such case, the system identification process is not a suitable method for fault detection and diagnosis due to the complexity of generating a large number of models for various operating as well as fault conditions, even though they can be accurate at a narrow operating region.

The physical models were accurate and offered a mechanism for understanding dynamic effects. They were chosen for fault detection and diagnosis in this study.

6 Fault detection and diagnosis on EHA

This chapter reports an implementation of three different fault detection and diagnosis strategies that were implemented on the EHA prototype. These were presented and introduced in Chapter 3. All the three strategies used the Interacting Multiple Model frame work. The first method, IMM-EKF used the popular Extended Kalman Filter. The second and the third methods used the Smooth Variable Structure Filter with different approaches for the smoothing boundary layer. The IMM-SVSF (VBL) implementation utilized the varying boundary layer while IMM-SVSF (FBL) used a fixed boundary layer. These three fault detection and diagnosis methods were applied to the fault conditions discussed in Chapter 4.

For fault detection, it is difficult to distinguish the leakage and the friction fault with velocity measurements only. Pressure measurement can be used to more accurately indicate the friction level of the system. Based on the physical model derived in Section 5.2.3, the EHA differential pressure can be equated to the actuator output force and friction equations as:

$$F = (P_1 - P_2)A = M\ddot{x} + F_f \tag{6-1}$$

$$F_f = a_2\dot{x} + (a_1\dot{x}^2 + a_3)sgn(\dot{x}) \tag{6-2}$$

Substituting (6-2) to (6-1) and rearranging yields,

$$P_1 - P_2 = \frac{M}{A}\ddot{x} + \frac{a_2}{A}\dot{x} + \frac{a_1\dot{x}^2 + a_3}{A}sgn(\dot{x}) \tag{6-3}$$

All the methods used a physical model of the EHA as derived in section 5.2.

$$\begin{aligned} x_{1,k+1} &= x_{1,k} + Tx_{2,k} \\ x_{2,k+1} &= x_{2,k} + Tx_{3,k} \end{aligned} \tag{6-4}$$

$$x_{3,k+1} = \left[1 - T\frac{a_2V_0 + M\beta L_t}{MV_0}\right]x_{3,k} - T\frac{(A^2 + a_2L_t)\beta}{MV_0}x_{2,k} - T\frac{2a_1V_0x_{2,k}x_{3,k} + \beta L_t\left(a_1x_{2,k}^2 + a_3\right)}{MV_0}sgn\left(x_{2,k}\right) + T\frac{A\beta}{MV_0}u_k$$

$$x_{4,k+1} = \frac{M}{A}x_{3,k} + \frac{a_2}{A}x_{2,k} + \frac{a_1x_{2,k}^2 + a_3}{A}sgn(x_{2,k})$$

where $x_1, x_2, x_3\ and\ x_4$ denote the four system states (actuator position, velocity, acceleration and differential pressure). u_k is an adjusted input defined as:

$$u(k) = D_p\omega_p(k) - sgn(x_{4,k})Q_{L0} \tag{6-5}$$

The Jacobian matrix of the system model is defined as

$$F_{sys}(k) = \varphi(k) = \frac{\partial f}{\partial x}$$

$$\varphi_{11} = 1;\ \varphi_{12} = T;\ \varphi_{13} = 0;\ \varphi_{14} = 0;\ \varphi_{21} = 0;\ \varphi_{22} = 1;\ \varphi_{23} = T;\ \varphi_{24} = 0;$$

$$\varphi_{31} = 0;\ \varphi_{32} = -T\frac{\beta(A^2 + a_2L_t)}{MV_0} - T\frac{\left(2a_1V_0x_{3,k} + 2a_1\beta L_tx_{2,k}\right)}{MV_0}sgn\left(x_{2,k}\right)$$

$$\varphi_{33} = 1 - T\frac{2a_1x_{2,k}}{M}sgn\left(x_{2,k}\right) - T(a_2V_0 + \beta L_tM);$$

$$\varphi_{34} = 0;$$

$$\varphi_{41} = 0;\ \varphi_{42} = \frac{a_2}{A} + \frac{2a_1x_{2,k}}{A}sgn\left(x_{2,k}\right);\ \varphi_{43} = \frac{M}{A};\ \varphi_{44} = 0;$$

The model parameters are listed in Table 6-1 to Table 6-3.

Table 6-1: EHA parameters and their values

EHA Parameter	Description	Value
D_p	Gear pump volumetric displacement	$5.57 \times 10^{-7}\ m^3/s$
A	Piston surface area	$1.52 \times 10^{-3}\ m^2$
V_0	Nominal volume of each EHA chamber	$1.08 \times 10^{-3}\ m^3$
M	Actuating mass	7.38 kg

Table 6-2: Leakage coefficients

Condition	Leakage Coefficient L_t	Offset Q_{L0}
Normal	$4.78 \times 10^{-12}\ Pa\ m^3/s$	$2.41 \times 10^{-6}\ m^3/s$
Minor Leakage	$2.52 \times 10^{-11}\ Pa\ m^3/s$	$1.38 \times 10^{-5}\ m^3/s$
Major Leakage	$6.01 \times 10^{-11}\ Pa\ m^3/s$	$1.47 \times 10^{-5}\ m^3/s$

Table 6-3: Friction coefficients

Condition	a_1	a_2	a_3
Normal	6.59×10^4	2.14×10^3	436
Minor Friction	1.16×10^6	-7.44×10^3	500
Major Friction	4.46×10^6	1.86×10^4	551

According to the system model, there are four states corresponding to the actuator position, velocity, acceleration, and differential pressure. The actuator position and differential pressure were measured by a linear encoder and two absolute pressure sensors. Hence, the measurement matrix used by the EKF was defined as:

$$H_{ekf} = \begin{bmatrix} 1 & 0 & 0 & 0 \\ 0 & 0 & 0 & 1 \end{bmatrix} \tag{6-6}$$

Due to the unique design of the SVSF, an output matrix that is full rank must be obtained through a transformation applied to measurements.

$$H_{svsf} = \begin{bmatrix} 1 & 0 & 0 & 0 \\ 0 & 1 & 0 & 0 \\ 0 & 0 & 1 & 0 \\ 0 & 0 & 0 & 1 \end{bmatrix} \tag{6-7}$$

The actuator velocity and acceleration were obtained by differentiating the measured position.

For both strategies, the initial state estimation and state error covariance are respectively set to:

$$\hat{x}_{0|0} = [0 \quad 0 \quad 0 \quad 0]^T$$

$$\mathrm{P}_{0|0} = \begin{bmatrix} 10 & 0 & 0 & 0 \\ 0 & 10 & 0 & 0 \\ 0 & 0 & 10 & 0 \\ 0 & 0 & 0 & 10 \end{bmatrix}$$

The nine conditions considered were defined in Chapter 4. These are numbered here for clarity as listed in the Table 6-4.

Table 6-4: Operation conditions numbering

Numbering	Condition
1	Normal

2	Minor Leakage
3	Major Leakage
4	Minor Friction
5	Major Friction
6	Minor leakage and Minor Friction
7	Minor leakage and Major Friction
8	Major leakage and Minor Friction
9	Major leakage and Major Friction

The EHA was assumed to have 90% chances to operate normally at the beginning and have an equal probability to experience one of the eight fault conditions. The initial mode probability $\mu_{i,0}$ was therefore defined as

$$\mu_{i,0} = [0.9 \quad 0.0125 \quad 0.0125 \quad 0.0125 \quad 0.0125 \quad 0.0125 \quad 0.0125 \quad 0.0125 \quad 0.0125]$$

After the start, the probability of mode switching was change to 98%, thus giving a mode transition matrix $p_{i,j}$ defined as

$$p_{ij} = \begin{bmatrix} 0.98 & 0.0025 & 0.0025 & 0.0025 & 0.0025 & 0.0025 & 0.0025 & 0.0025 & 0.0025 \\ 0.0025 & 0.98 & 0.0025 & 0.0025 & 0.0025 & 0.0025 & 0.0025 & 0.0025 & 0.0025 \\ 0.0025 & 0.0025 & 0.98 & 0.0025 & 0.0025 & 0.0025 & 0.0025 & 0.0025 & 0.0025 \\ 0.0025 & 0.0025 & 0.0025 & 0.98 & 0.0025 & 0.0025 & 0.0025 & 0.0025 & 0.0025 \\ 0.0025 & 0.0025 & 0.0025 & 0.0025 & 0.98 & 0.0025 & 0.0025 & 0.0025 & 0.0025 \\ 0.0025 & 0.0025 & 0.0025 & 0.0025 & 0.0025 & 0.98 & 0.0025 & 0.0025 & 0.0025 \\ 0.0025 & 0.0025 & 0.0025 & 0.0025 & 0.0025 & 0.0025 & 0.98 & 0.0025 & 0.0025 \\ 0.0025 & 0.0025 & 0.0025 & 0.0025 & 0.0025 & 0.0025 & 0.0025 & 0.98 & 0.0025 \\ 0.0025 & 0.0025 & 0.0025 & 0.0025 & 0.0025 & 0.0025 & 0.0025 & 0.0025 & 0.98 \end{bmatrix}$$

The elements of $p_{ij}$are the probabilities of the EHA switching from one mode to another. The diagonal cells (with values 0.98) indicated that the EHA has 98% chances of retaining the same mode with which it started. Furthermore, the non-diagonal elements

(with values 0.0025) stated that the EHA had a 0.25% chance of transiting to a different mode.

Recall that the SVSF with a varying smoothing boundary layer (VBL) required the maximum smooth boundary layer width (ψ_{max}) to be defined. By trial and error, the maximum smooth boundary layer width (ψ_{max}) was tuned to yield the best possible fault detection performance for IMM-SVSF as:

$$\psi_{max} = [3.5 \times 10^{-6}\ 10\ 1000\ 5 \times 10^{6}]$$

The residual is an important indicator of fault detection and diagnosis. In the application of the SVSF with IMM, the residual was the difference between the predicted and the measured states. In this case, it was possible to enhance fault detection by increasing the model information portion. Therefore, the SVSF with a fixed smooth boundary layer (FBL) was also implemented with IMM. The fixed smooth boundary layer ψ was chosen to be 1000 times of the ψ_{max} used in the SVSF (VBL).

$$\psi = [3.5 \times 10^{-3}\ 1 \times 10^{4}\ 1 \times 10^{6}\ 5 \times 10^{9}]$$

6.1 FDD Test with Step Inputs of Fixed Amplitude

Figure 6-1 shows the sequential step input into the EHA for fault detection tests. It has an amplitude of ±106.81 rad/sec (1020 RPM), and changes direction every second.

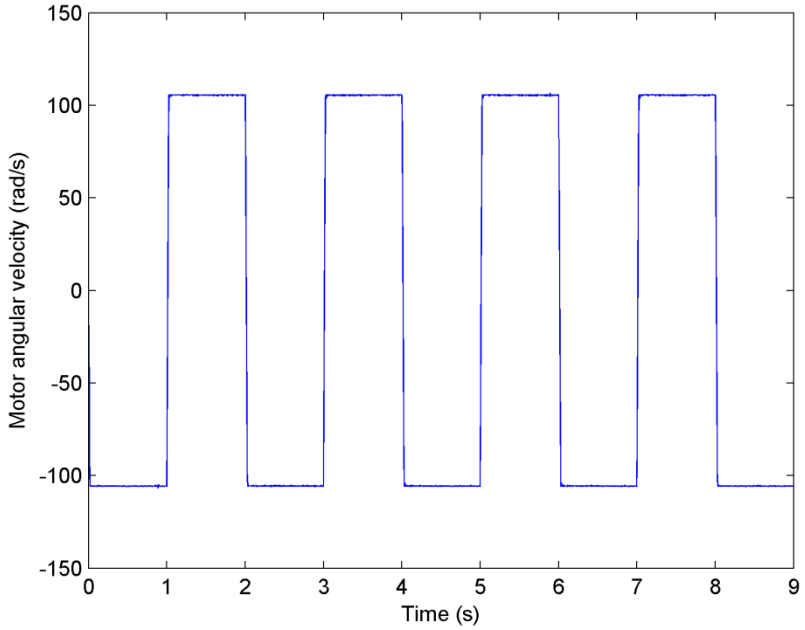

Figure 6-1: Test input for fault detection

The change in the operating conditions of the EHA during the test was as listed in Table 6-5.

Table 6-5: EHA operating mode with single amplitude input

Time (s)	EHA operating condition
0 – 1	Normal
1 – 2	Minor Leakage
2 – 3	Major Leakage
3 – 4	Minor Friction
4 – 5	Major Friction
5 – 6	Minor Leakage and Minor Friction
6 – 7	Minor Leakage and Major Friction

7 – 8	Major Leakage and Minor Friction
8 – 9	Major Leakage and Major Friction

Figure 6-2 demonstrates the corresponding unfiltered (in blue) and filtered (in green) EHA output. Recall that a linear encoder and two absolute pressure sensors measured the actuator position and differential pressure respectively. For the SVSF implementation, actuator velocity and acceleration measurements were derived from the position by differentiation. The measurement noise was filtered by a zero-phase 12^{th} order Butterworth low pass filter described in section 5.3.3. Note that the unfiltered acceleration measurement contained a great deal of noise which was amplified by double differentiation and had peak amplitude of 200 m/s^2. The noise in the acceleration measurement significantly affected the SVSF performance, and therefore, only the filtered acceleration measurement was used with the IMM-SVSF for fault detection and diagnosis.

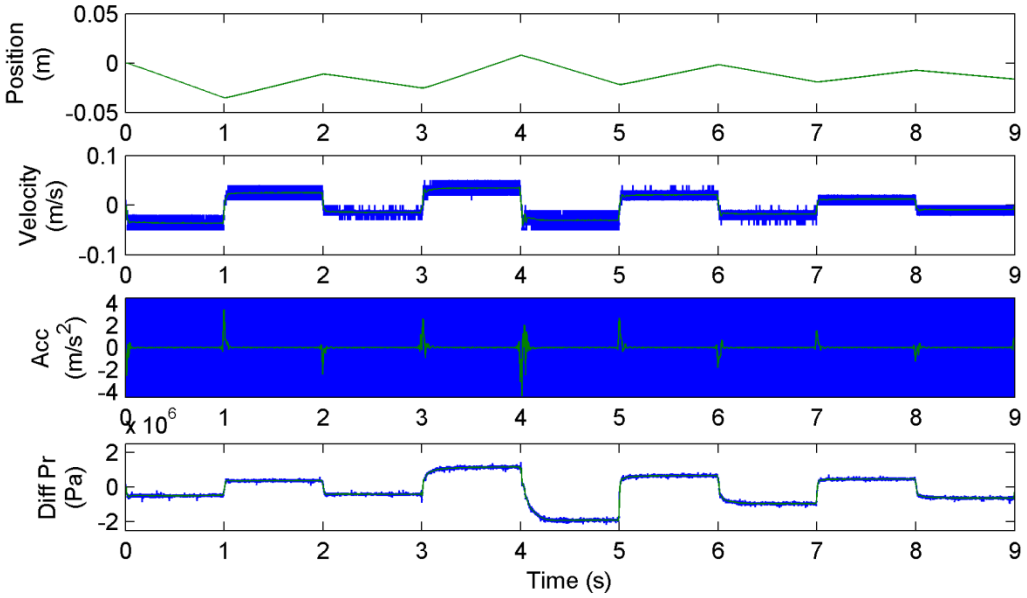

Figure 6-2: EHA output with single amplitude test input

Note that the system and measurement noise covariance matrices Q and R were required for both the EKF and the SVSF implementations. A number of methods have been developed to statistically estimate values of these two matrices [**46**] [**47**] [**48**]. Gadsden presented a method to determine the measurement error covariance R with a segment of the measurement signal [**21**]. The measurement noise covariance R was calculated by the following equation:

$$R = \frac{(z_i - \bar{z})(z_i - \bar{z})^T}{z_m} \tag{6-8}$$

where z_i and $\bar{z}$ denote the i^{th} measurement sample and measurement mean of a data segment. z_m is the number of samples in the segment.

The measurements segments were chosen from 1.1 sec to 1.9 sec as shown in Figure 6-3,

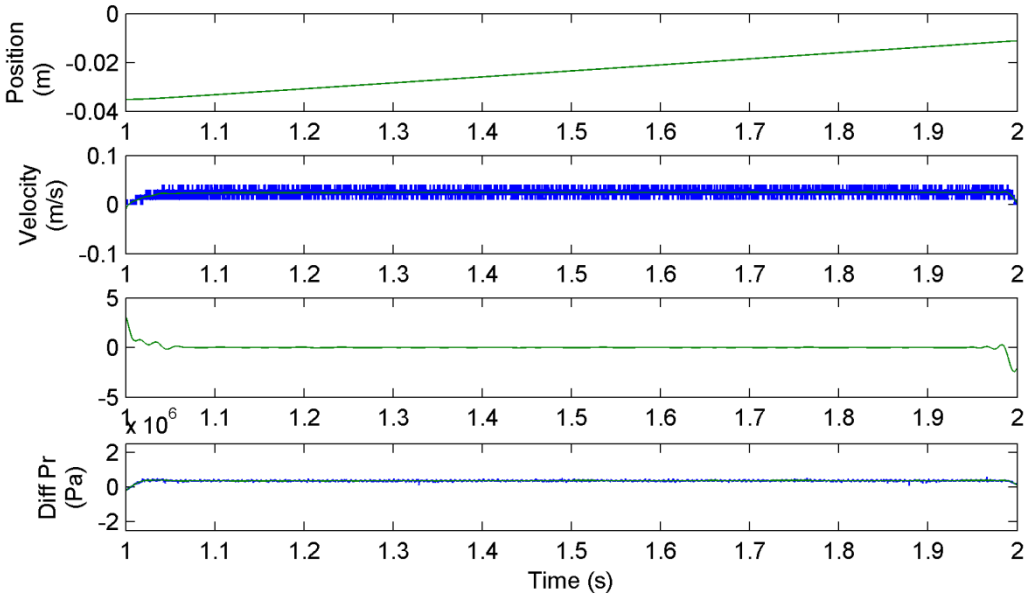

Figure 6-3: measurement segments

The velocity, acceleration and differential pressure measurement noise covariance values were calculated for the noisy measurement and the filtered measurement respectively as follow.

$$R_{vel,noisy} = 7.0198 \times 10^{-5} \, (\frac{m^2}{s^2})$$

$$R_{vel,filtered} = 3.0064 \times 10^{-8} \, (\frac{m^2}{s^2})$$

$$R_{acc} = 7.0039 \times 10^{-4} \, (\frac{m^2}{s^4})$$

$$R_{diff\ Pr,noisy} = 2.7254 \times 10^{9} \, (Pa^2)$$

$$R_{diff\ Pr,filtered} = 1.7343 \times 10^{7} \, (Pa^2)$$

The resolution of the linear encoder was 1 μm. The position measurement covariance was calculated as the square of the linear encoder resolution [**25**].

$$R_p = 1 \times 10^{-12} \, (m^2).$$

For the IMM-EKF, the measurement noise covariance matrices were defined as:

$$R_{EKF,noisy} = \begin{bmatrix} 1 \times 10^{-12} & 0 \\ 0 & 2.7254 \times 10^{9} \end{bmatrix}$$

$$R_{EKF,filtered} = \begin{bmatrix} 1 \times 10^{-12} & 0 \\ 0 & 1.7343 \times 10^{7} \end{bmatrix}$$

For the IMM-SVSF (VBL) and the IMM-SVSF (FBL), the measurement noise covariance matrices were defined as:

$$R_{SVSF,noisy} = diag[1 \times 10^{-12} \; 7.0198 \times 10^{-5} \; 7.0039 \times 10^{-4} \; 2.7254 \times 10^{9}]$$

$$R_{SVSF,noisy} = diag[1 \times 10^{-12} \; 3.0064 \times 10^{-8} \; 7.0039 \times 10^{-4} \; 1.7343 \times 10^{7}]$$

The system noise covariance Q was estimated by trial and error as:

$$Q = diag[1 \times 10^{-12}\ 1 \times 10^{-10}\ 1 \times 10^{-9}\ 1 \times 10^{6}]$$

6.1.1 Fixed Amplitude Test with Noisy Measurement

All the three strategies were implemented on the EHA for fault detection and diagnosis (FDD) with unfiltered (noisy) and filtered measurements. The mode probabilities μ were used as the indication of the operating mode. A fault was considered as being successfully detected if its corresponding mode probability was the highest.

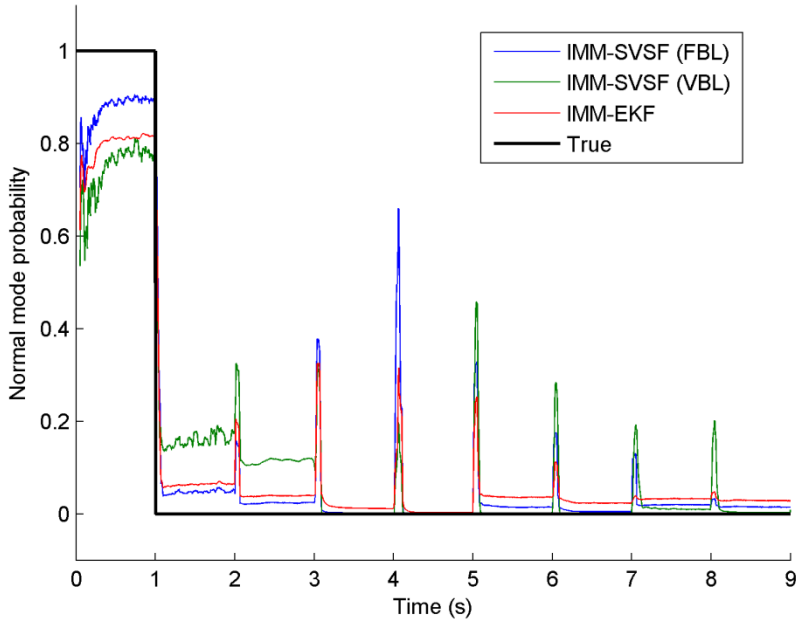

Figure 6-4: Normal mode probability for the EHA fault detection and diagnosis experiment

Faults were physically simulated on the EHA prototype sequentially for one second according to Table 6-5. Normal operation applied to the first second and Figure 6-4 shows the detection of the normal mode probability by the IMM-EKF, IMM-SVSF (FBL) and IMM-SVSF (FBL) respectively. All of the strategies were implemented with unfiltered measurement. The expected 'True' state is plotted in black. In this test, the normal working condition was imposed during the first second. The 'True' state

indicating normal mode probability therefore equaled 1 during the first second. After the first second, the 'True' state switched to 0, indicating that the normal operation condition no longer applied. According to the results demonstrated in Figure 6-4, all the three methods successfully detected the normal mode by having high normal mode probabilities during the first second. The normal mode probabilities of three methods dropped to show that the EHA was no longer operating normally after the first second. Note that all the mode probabilities results were smoothed by moving averaging of 200 iterations for clarity. Spikes are present because of the selected type of input (sequential step). When the actuator velocity and differential pressure across $0\ m/s$ and $0\ Pa$, the nine models become indistinguishable.

The probabilities of the other eight modes are shown in Figure 6-5 to Figure 6-12.

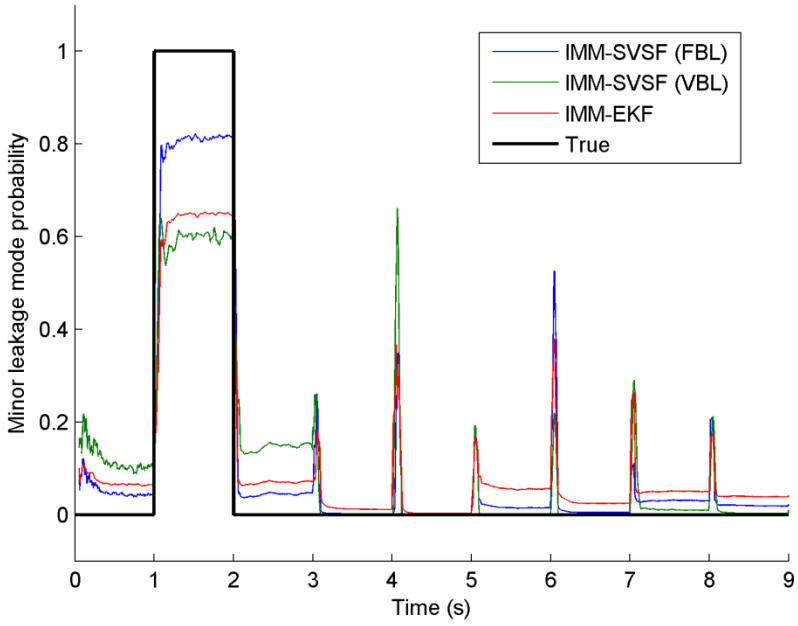

Figure 6-5: Minor leakage mode probability for the EHA fault detection and diagnosis experiment

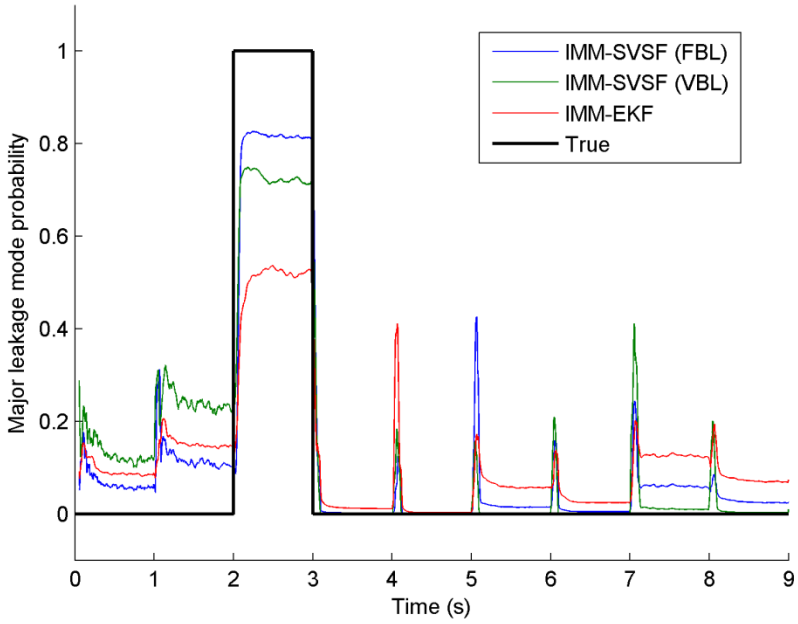

Figure 6-6: Major leakage mode probability for the EHA fault detection and diagnosis experiment

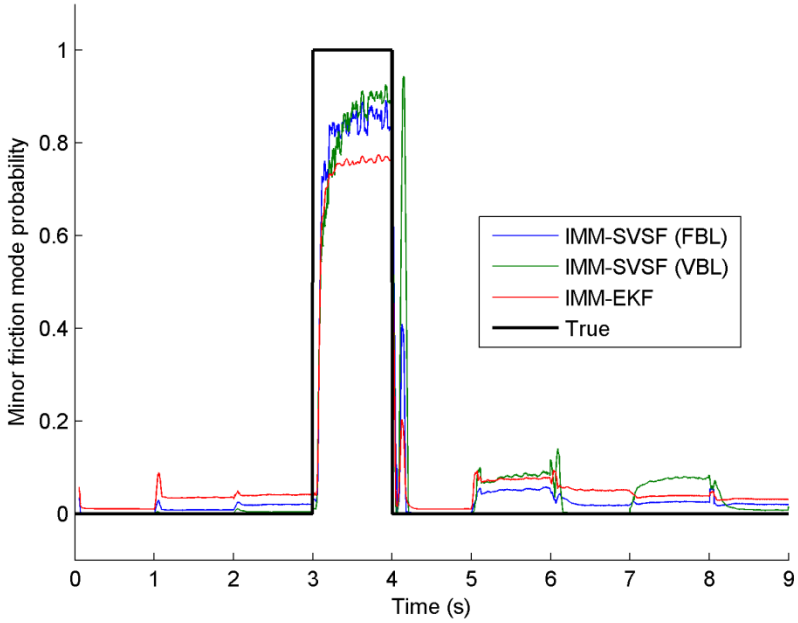

Figure 6-7: Minor friction mode probability for the EHA fault detection and diagnosis experiment

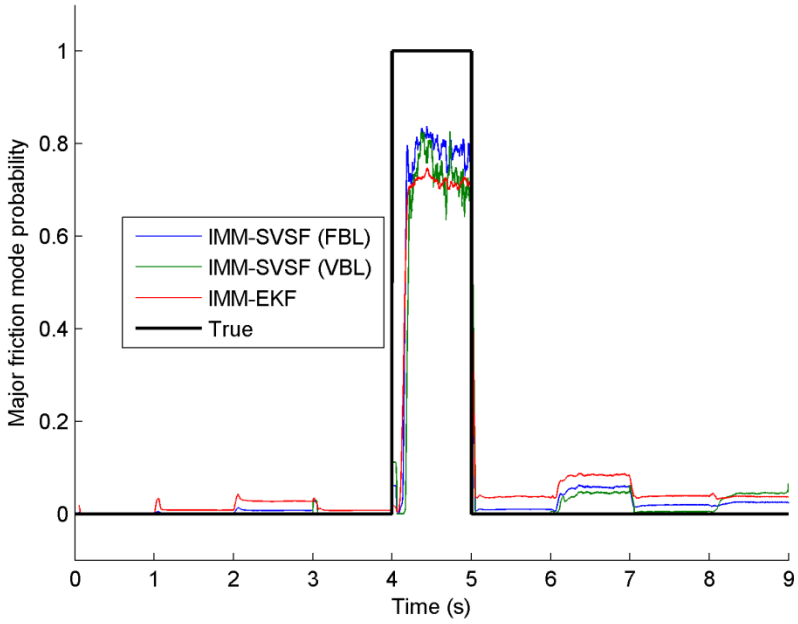

Figure 6-8: Major friction mode probability for the EHA fault detection and diagnosis experiment

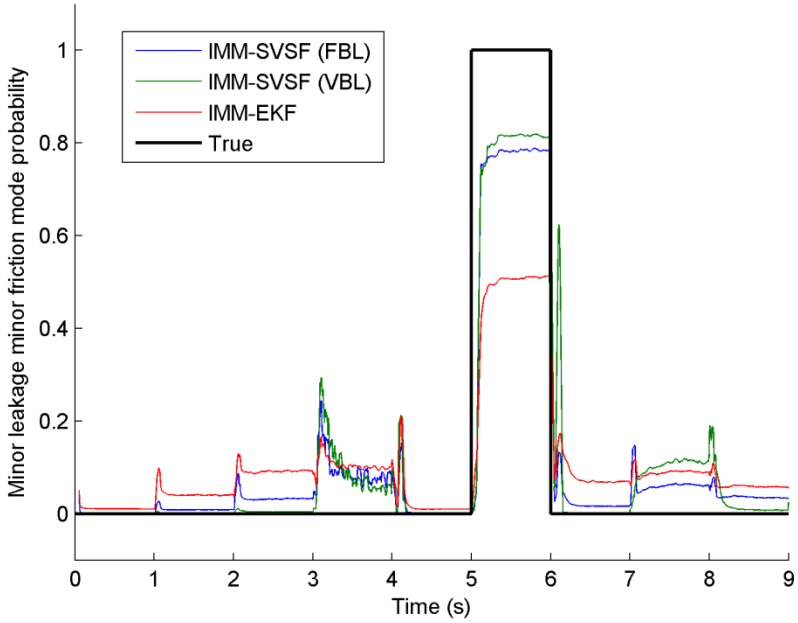

Figure 6-9: Minor leakage and minor friction mode probability for the EHA fault detection and diagnosis experiment

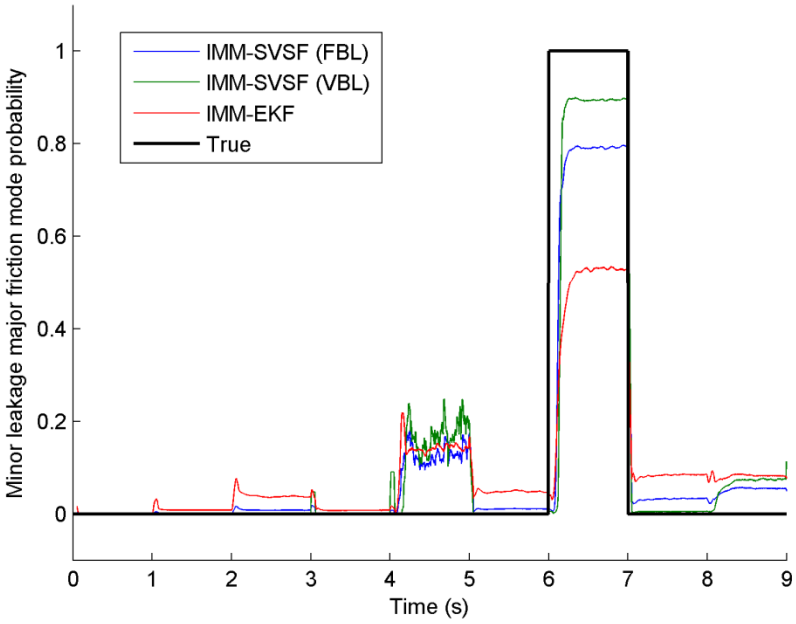

Figure 6-10: Minor leakage and major friction mode probability for the EHA fault detection and diagnosis experiment

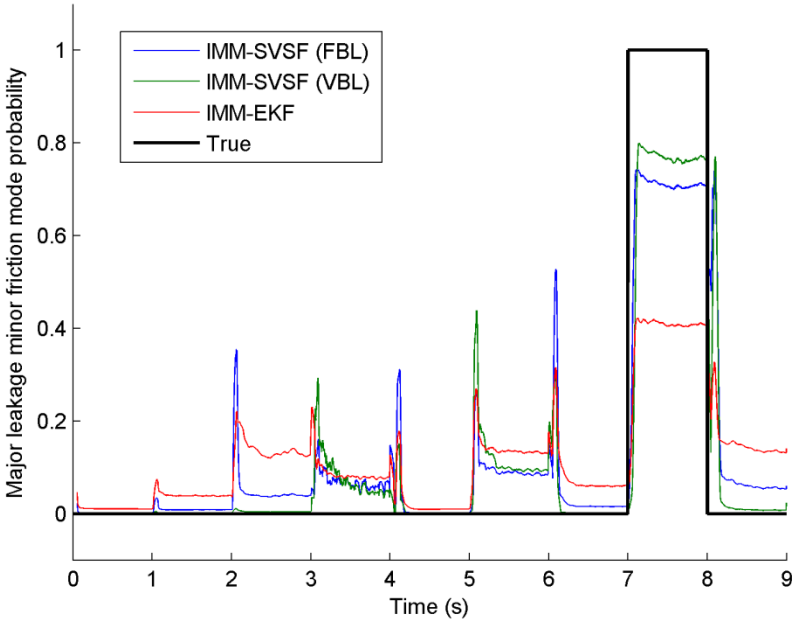

Figure 6-11: Major leakage and minor friction mode probability for the EHA fault detection and diagnosis experiment

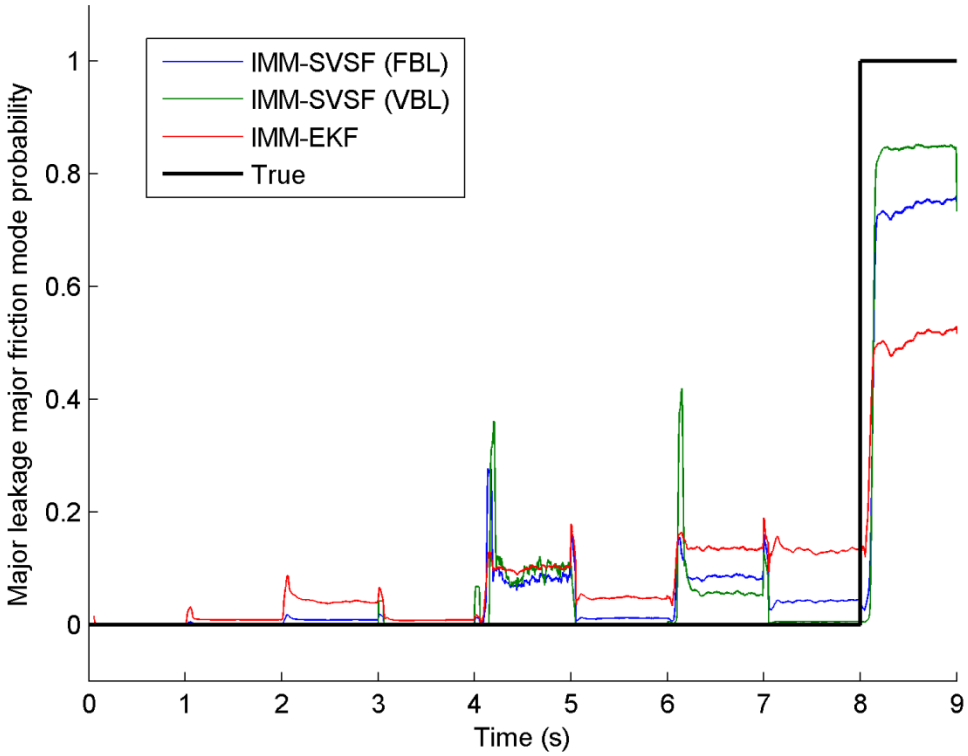

Figure 6-12: Major leakage and major friction mode probability for the EHA fault detection and diagnosis experiment

According to the results demonstrated, all the three method successfully detected the system fault conditions and correctly diagnosed them. In order to compare their performances, the mean probabilities of each mode were calculated and listed in a confusion matrix format in Table 6-6 to Table 6-8. In these confusion matrices, the first row indicates the working condition that the EHA was operating in. The first column lists the condition that is predicted. The underlined diagonal cells show the probabilities of correctly detecting the fault conditions.

Compared to the IMM-EKF, the IMM-SVSF (VBL) had comparable probabilities for the mode Normal, Minor leakage and Major friction. With the other modes, IMM-SVSF (VBL) has approximately 20-30% higher probabilities of being correct. IMM-SVSF (FBL) successfully detected all working conditions correctly. Compared to the IMM-SVSF

(VBL), the FBL improved the fault detection performance with the Normal, Minor leakage, and Major friction modes. It detected faults correctly with probabilities of over 70%.

Table 6-6: IMM-EKF performance with unfiltered measurement

IMM-EKF (Mode probability)		Operating condition								
		Normal	Minor Leakage	Major Leakage	Minor Friction	Major Friction	Min. L. Min. F.	Min. L. Maj. F.	Maj. L. Min. F.	Maj. L. Maj. F.
Model condition	Normal	**80.13%**	6.36%	3.89%	1.34%	0.37%	3.65%	2.42%	3.26%	2.90%
	Minor Leakage	6.99%	**64.47%**	6.93%	1.31%	0.36%	5.75%	2.61%	5.01%	3.93%
	Major Leakage	9.27%	15.25%	**51.73%**	1.32%	0.36%	6.09%	2.63%	12.60%	7.34%
	Minor Friction	1.06%	3.47%	4.05%	**75.08%**	1.97%	7.42%	5.17%	3.82%	3.15%
	Major Friction	0.14%	0.82%	2.76%	0.75%	**69.56%**	3.69%	8.28%	3.86%	3.70%
	Min. L. Min. F.	1.07%	4.04%	9.12%	10.51%	1.46%	**50.21%**	7.82%	8.87%	5.88%
	Min. L. Maj. F.	0.14%	0.84%	3.83%	0.77%	14.52%	4.83%	**50.79%**	8.35%	8.21%
	Maj. L. Min. F.	1.07%	3.89%	13.54%	8.12%	1.29%	13.62%	6.59%	**40.99%**	14.39%
	Maj. L. Maj. F.	0.14%	0.85%	4.15%	0.78%	10.10%	4.74%	13.69%	13.25%	**50.51%**

Table 6-7: IMM-SVSF (VBL) performance with unfiltered measurement

IMM-SVSF (VBL) (Mode probability)		**Operating condition**								
		Normal	Minor Leakage	Major Leakage	Minor Friction	Major Friction	Min. L. Min. F.	Min. L. Maj. F.	Maj. L. Min. F.	Maj. L. Maj. F.
Model condition	Normal	**75.26%**	15.89%	11.39%	0.00%	0.00%	0.12%	0.02%	1.10%	0.33%
	Minor Leakage	11.59%	**59.53%**	14.54%	0.00%	0.00%	0.12%	0.02%	1.10%	0.33%
	Major Leakage	13.15%	24.44%	**72.71%**	0.00%	0.00%	0.12%	0.02%	1.09%	0.33%
	Minor Friction	0.00%	0.04%	0.40%	**83.65%**	6.20%	7.88%	0.17%	7.39%	1.16%
	Major Friction	0.00%	0.00%	0.05%	0.00%	**67.45%**	0.07%	4.30%	0.49%	4.23%
	Min. L. Min. F.	0.00%	0.04%	0.40%	9.21%	0.19%	**80.76%**	0.24%	10.68%	1.18%
	Min. L. Maj. F.	0.00%	0.00%	0.05%	0.00%	15.45%	0.07%	**86.98%**	0.51%	6.97%
	Maj. L. Min. F.	0.00%	0.04%	0.41%	7.13%	0.18%	10.78%	0.16%	**77.13%**	1.72%
	Maj. L. Maj. F.	0.00%	0.00%	0.05%	0.00%	10.53%	0.07%	8.09%	0.52%	**83.74%**

Table 6-8: IMM-SVSF (FBL) performance with unfiltered measurement

IMM-SVSF (FBL) (Mode probability)		Operating condition								
		Normal	Minor Leakage	Major Leakage	Minor Friction	Major Friction	Min. L. Min. F.	Min. L. Maj. F.	Maj. L. Min. F.	Maj. L. Maj. F.
Model condition	Normal	**88.10%**	4.75%	2.34%	0.23%	0.04%	1.53%	0.55%	1.95%	1.52%
	Minor Leakage	4.96%	**80.91%**	4.35%	0.23%	0.04%	1.61%	0.55%	3.04%	1.98%
	Major Leakage	6.44%	11.45%	**81.77%**	0.23%	0.04%	1.60%	0.54%	6.01%	2.67%
	Minor Friction	0.16%	0.81%	1.96%	**83.40%**	2.22%	5.06%	2.05%	2.49%	2.03%
	Major Friction	0.00%	0.12%	0.75%	0.10%	**75.39%**	0.97%	5.62%	1.92%	2.45%
	Min. L. Min. F.	0.16%	0.85%	3.18%	8.94%	0.42%	**77.93%**	1.99%	5.98%	3.57%
	Min. L. Maj. F.	0.00%	0.12%	0.82%	0.10%	12.36%	1.08%	**78.16%**	3.23%	5.36%
	Maj. L. Min. F.	0.16%	0.86%	3.99%	6.64%	0.38%	9.10%	1.82%	**71.20%**	7.13%
	Maj. L. Maj. F.	0.00%	0.12%	0.85%	0.10%	9.12%	1.13%	8.73%	4.18%	**73.29%**

Table 6-9: RMSE results for single amplitude input (unfiltered measurement)

Fault detection Strategy	Position (m)	Velocity (m/s)	Acceleration (m/s^2)	Differential pressure (Pa)
IMM-EKF	2.10E-06	1.18E-03	2.41E-01	8.42E+04
IMM-SVSF (FBL)	2.09E-06	1.64E-03	2.53E-01	5.71E+04
IMM-SVSF (VBL)	2.12E-06	8.15E-04	1.04E-01	5.63E+04

Table 6-9 shows the RMSE results for all the three fault detection strategies (IMM-EKF, IMM-SVSF (FBL), and IMM-SVSF (VBL)). All the three fault detection strategies had equivalent RMSE of the first state (Position). IMM-SVSF (VBL) had the least RMSE of the other three states. This finding agrees with the results demonstrated in [**33**].

6.1.2 Fixed Amplitude Test with Filtered Measurement

All the three strategies were implemented with filtered measurements for better fault detection performance. The filtering introduces distortion and signal loss. However, the benefits of filtering demonstrated by results justify their use. The mode probability results are reported in Figure 6-13 to Figure 6-21 and Table 6-10 to Table 6-13 as follows.

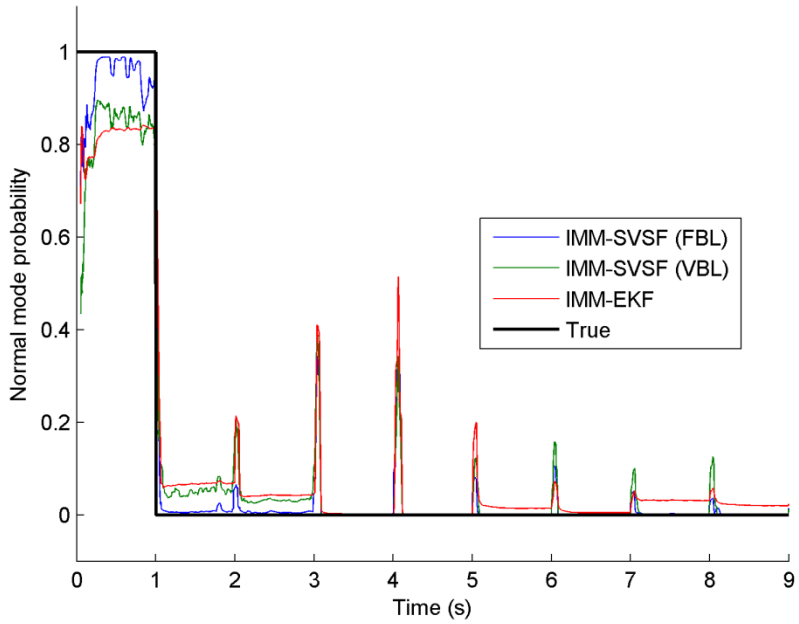

Figure 6-13: Normal mode probability for the EHA fault detection and diagnosis experiment

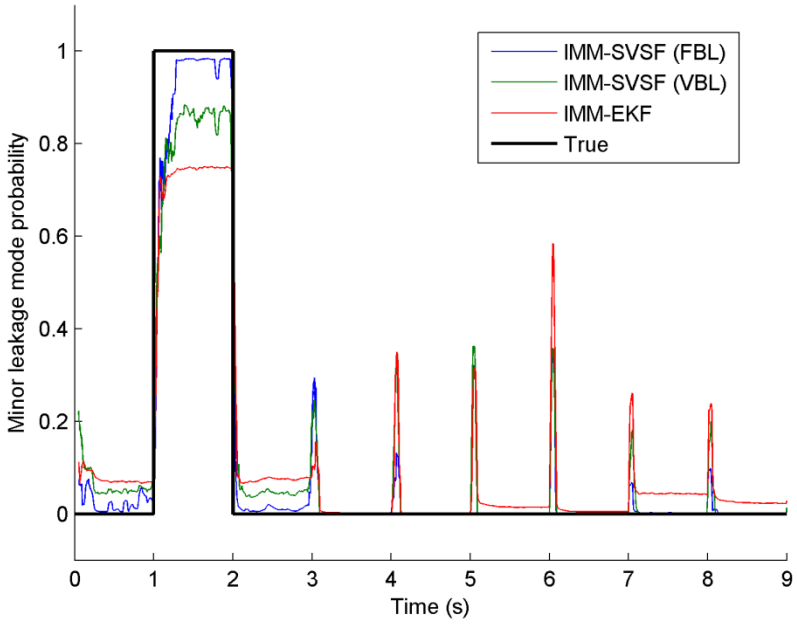

Figure 6-14: Minor leakage mode probability for the EHA fault detection and diagnosis experiment

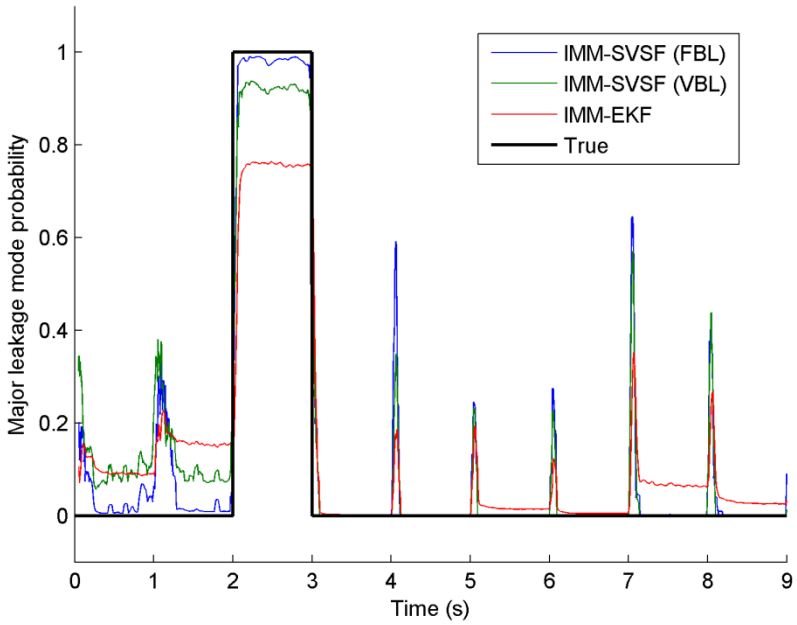

Figure 6-15: Major leakage mode probability for the EHA fault detection and diagnosis experiment

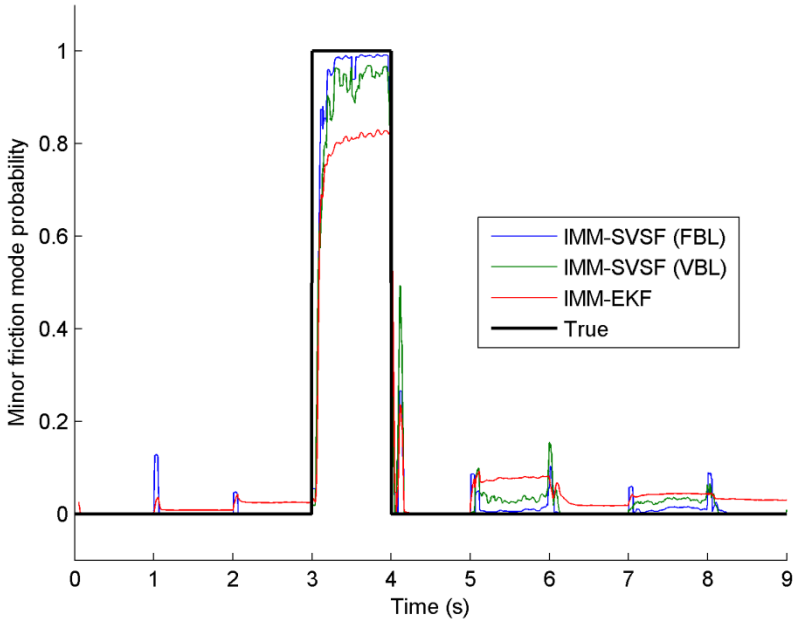

Figure 6-16: Minor friction mode probability for the EHA fault detection and diagnosis experiment

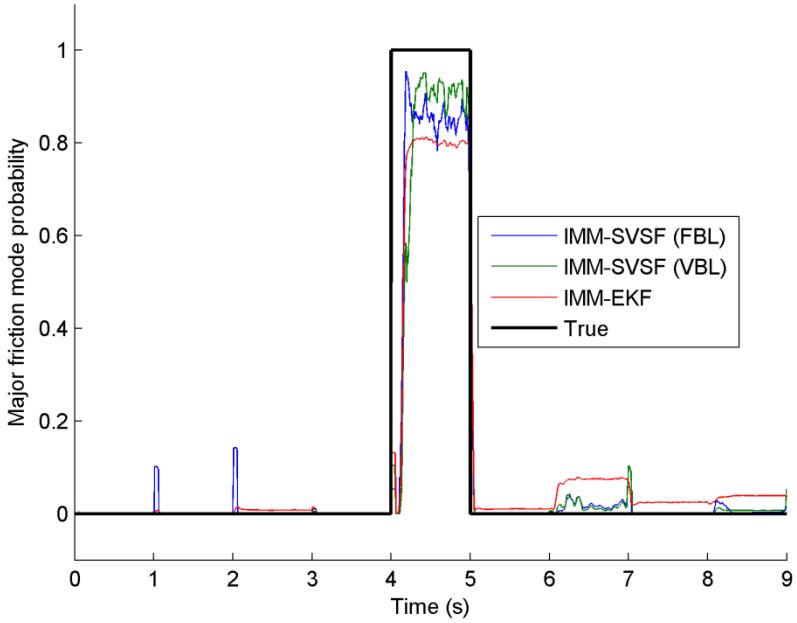

Figure 6-17: Major friction mode probability for the EHA fault detection and diagnosis experiment

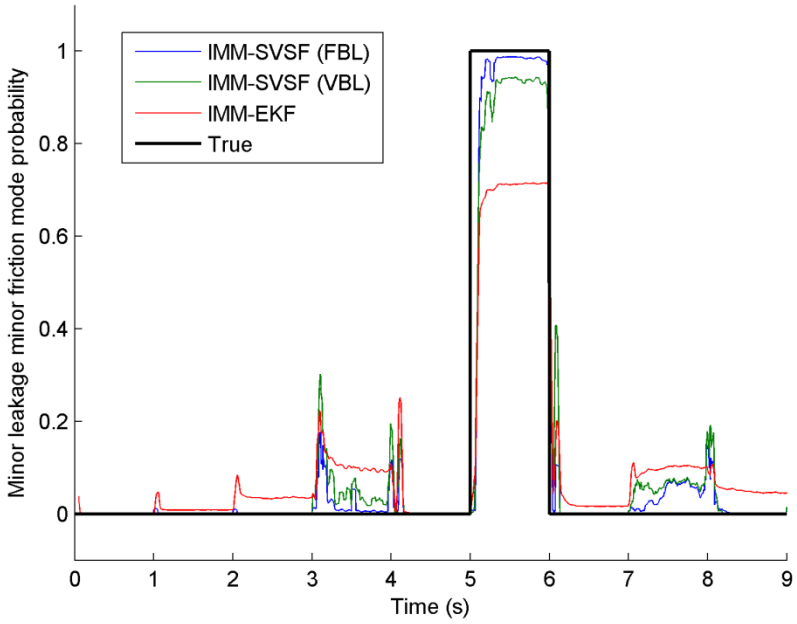

Figure 6-18: Minor leakage minor friction mode probability for the EHA fault detection and diagnosis experiment

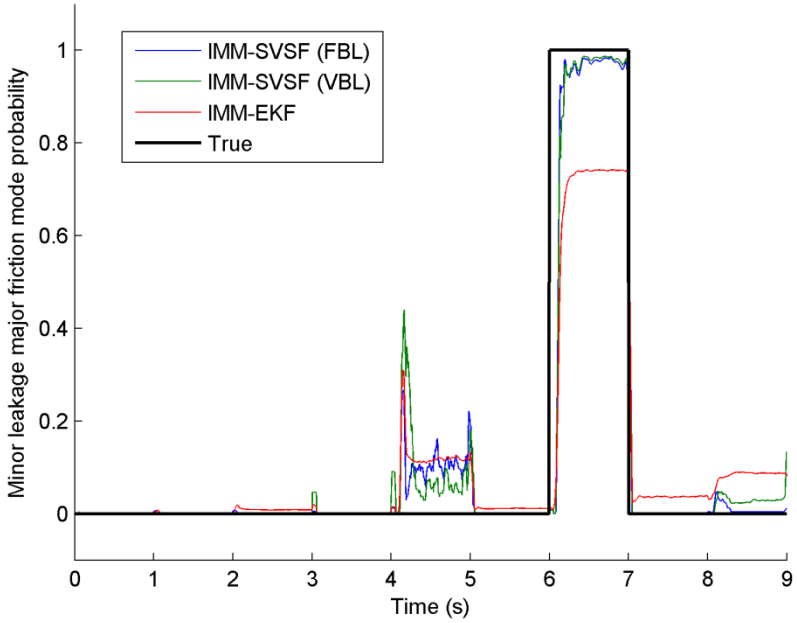

Figure 6-19: Minor leakage major friction mode probability for the EHA fault detection and diagnosis experiment

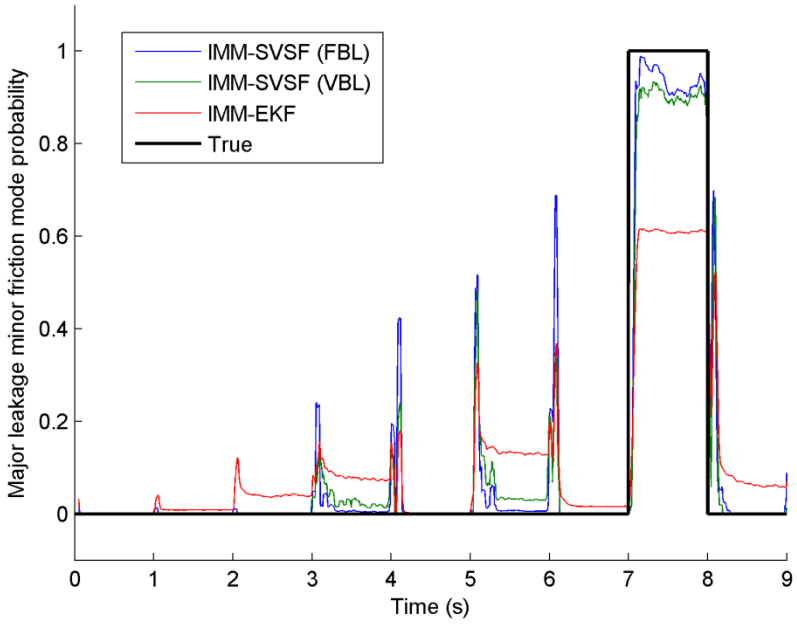

Figure 6-20: Major leakage minor friction mode probability for the EHA fault detection and diagnosis experiment

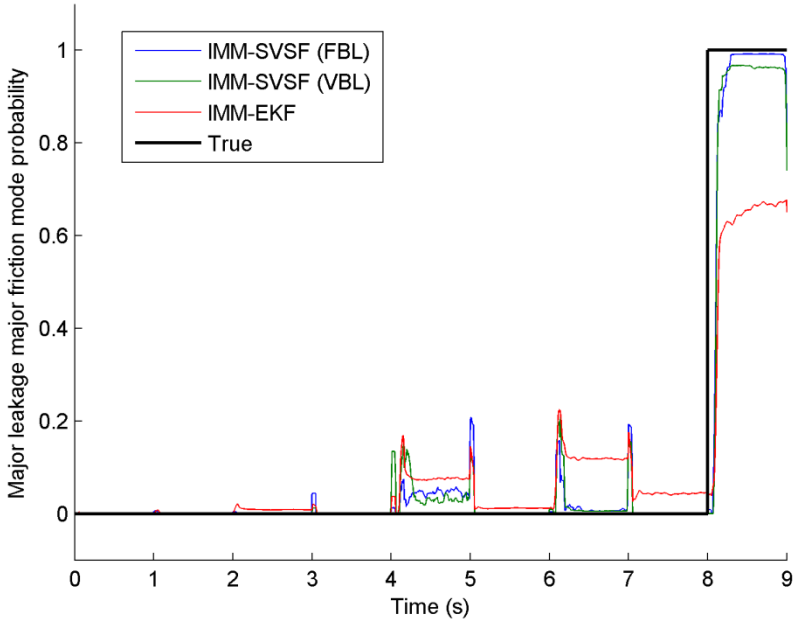

Figure 6-21: Major leakage major friction mode probability for the EHA fault detection and diagnosis experiment

Table 6-10: IMM-EKF performance with filtered measurement

IMM-EKF (Mode probability)		Operating condition								
		Normal	Minor Leakage	Major Leakage	Minor Friction	Major Friction	Min. L. Min. F.	Min. L. Maj. F.	Maj. L. Min. F.	Maj. L. Maj. F.
Model condition	Normal	**82.36%**	6.69%	4.20%	0.23%	0.04%	1.54%	0.55%	3.14%	2.11%
	Minor Leakage	7.39%	**74.31%**	7.43%	0.23%	0.04%	1.58%	0.54%	4.38%	2.49%
	Major Leakage	9.72%	16.06%	**75.81%**	0.23%	0.04%	1.57%	0.54%	6.75%	2.89%
	Minor Friction	0.17%	0.82%	2.47%	**80.33%**	0.79%	7.64%	2.07%	4.27%	3.10%
	Major Friction	0.01%	0.13%	0.79%	0.11%	**77.46%**	1.02%	7.41%	2.46%	3.84%
	Min. L. Min. F.	0.17%	0.86%	3.51%	10.54%	0.29%	**70.77%**	1.96%	9.88%	4.95%
	Min. L. Maj. F.	0.01%	0.13%	0.86%	0.11%	12.92%	1.13%	**72.65%**	3.68%	8.63%
	Maj. L. Min. F.	0.17%	0.87%	4.04%	8.10%	0.25%	13.54%	1.83%	**61.07%**	7.21%
	Maj. L. Maj. F.	0.01%	0.13%	0.89%	0.11%	8.17%	1.19%	12.45%	4.38%	**64.78%**

Table 6-11: IMM-SVSF (VBL) performance with filtered measurement

IMM-SVSF (VBL) (Mode probability)		**Operating condition**								
		Normal	Minor Leakage	Major Leakage	Minor Friction	Major Friction	Min. L. Min. F.	Min. L. Maj. F.	Maj. L. Min. F.	Maj. L. Maj. F.
Model condition	Normal	**84.84%**	5.11%	3.09%	0.00%	0.00%	0.00%	0.00%	0.08%	0.01%
	Minor Leakage	5.55%	**84.84%**	4.48%	0.00%	0.00%	0.00%	0.00%	0.08%	0.01%
	Major Leakage	9.60%	10.05%	**92.38%**	0.00%	0.00%	0.00%	0.00%	0.08%	0.01%
	Minor Friction	0.00%	0.00%	0.01%	**92.45%**	1.07%	3.21%	0.00%	2.88%	0.07%
	Major Friction	0.00%	0.00%	0.00%	0.00%	**83.72%**	0.00%	1.67%	0.02%	0.74%
	Min. L. Min. F.	0.00%	0.00%	0.01%	4.83%	0.17%	**92.26%**	0.00%	6.29%	0.10%
	Min. L. Maj. F.	0.00%	0.00%	0.00%	0.00%	10.36%	0.00%	**96.73%**	0.02%	2.93%
	Maj. L. Min. F.	0.00%	0.00%	0.01%	2.72%	0.09%	4.53%	0.00%	**90.54%**	0.18%
	Maj. L. Maj. F.	0.00%	0.00%	0.00%	0.00%	4.59%	0.00%	1.60%	0.02%	**95.97%**

Table 6-12: IMM-SVSF (FBL) performance with filtered measurement

IMM-SVSF (FBL) (Mode probability)		Operating condition								
		Normal	Minor Leakage	Major Leakage	Minor Friction	Major Friction	Min. L. Min. F.	Min. L. Maj. F.	Maj. L. Min. F.	Maj. L. Maj. F.
Model condition	Normal	**95.02%**	0.76%	0.53%	0.00%	0.00%	0.00%	0.00%	0.17%	0.02%
	Minor Leakage	2.25%	**95.15%**	0.97%	0.00%	0.00%	0.00%	0.00%	0.16%	0.02%
	Major Leakage	2.73%	4.09%	**98.46%**	0.00%	0.00%	0.00%	0.00%	0.15%	0.07%
	Minor Friction	0.00%	0.00%	0.01%	**97.25%**	0.75%	0.67%	0.00%	1.03%	0.13%
	Major Friction	0.00%	0.00%	0.00%	0.00%	**84.08%**	0.00%	1.93%	0.04%	0.56%
	Min. L. Min. F.	0.00%	0.00%	0.01%	1.82%	0.02%	**97.94%**	0.00%	4.55%	0.17%
	Min. L. Maj. F.	0.00%	0.00%	0.00%	0.00%	10.57%	0.00%	**96.82%**	0.03%	0.76%
	Maj. L. Min. F.	0.00%	0.00%	0.01%	0.92%	0.01%	1.39%	0.00%	**93.84%**	0.60%
	Maj. L. Maj. F.	0.00%	0.00%	0.00%	0.00%	4.57%	0.00%	1.25%	0.03%	**97.67%**

According to results, all of the three proposed strategies (IMM-EKF, IMM-SVSF (VBL), and IMM-SVSF (FBL)) successfully detected system changes and correctly diagnosed all nine conditions. The fault detection and diagnosis (FDD) performances were better with filtered measurements by having considerably better probabilities of correctly detecting the operating mode. Compared to the IMM-EKF, the two IMM-SVSF strategies had overall better correct mode probabilities. The performances of the two IMM-SVSF strategies were comparable. Table 6-13 summarizes the RMSE results for all of the three FDD strategies.

Table 6-13: RMSE results for fixed amplitude input (filtered measurement)

Fault detection Strategy	Position (m)	Velocity (m/s)	Acceleration (m/s^2)	Differential pressure (Pa)
IMM-EKF	8.12E-07	1.33E-03	2.50E-01	5.75E+04
IMM-SVSF (FBL)	3.36E-07	1.89E-03	2.89E-01	6.82E+04
IMM-SVSF (VBL)	8.89E-09	1.46E-04	1.02E-01	5.89E+04

Although the IMM-SVSF (VBL) had slightly larger RMSE of differential pressure than IMM-EKF, it still outperformed the other two strategies by having much smaller RMSE of position, velocity and acceleration states.

In this section, a sequential step signal with fixed amplitude was used as input the to the EHA prototype. Three FDD strategies were implemented with both unfiltered and filtered measurements. Their FDD and estimation performances were evaluated and compared. The IMM-SVSF (FBL) provided the best FDD performance by having the highest overall probability of correctly detecting the

operating mode. However, with comparable FDD performance, the IMM-SVSF (VBL) provided the best estimation performance.

6.2 FDD Test with Step Inputs of Varying Amplitudes

In order to test the three FDD strategies at different operating points, a series of sequential steps with randomly varying amplitudes was used as shown in Figure 6-22.

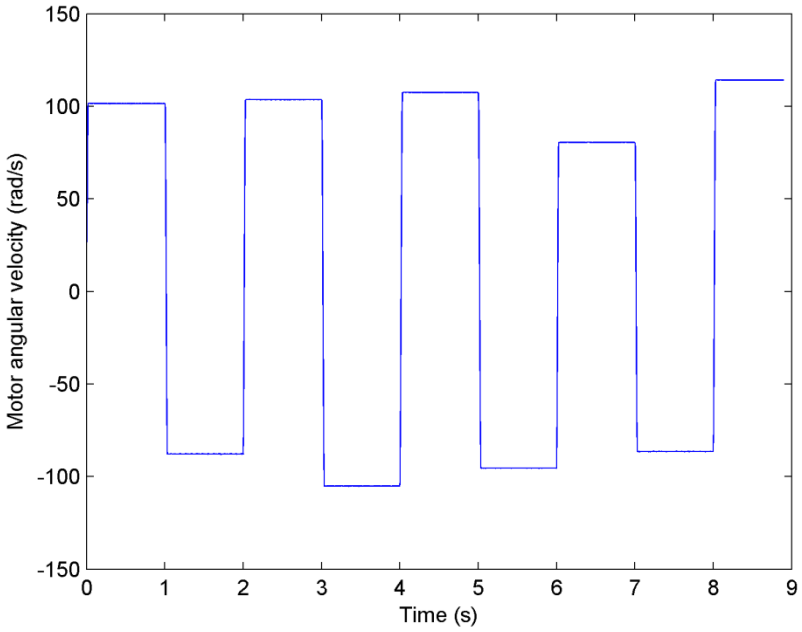

Figure 6-22: Test input with varying amplitude

Similar to the fixed amplitude input test, the actuator position and differential pressure were measured by an optical linear encoder and two absolute pressure sensors. The projected measures of velocity and acceleration were derived from the position measurement by differentiation for the SVSF implementation. As an example, the unfiltered (blue) and filtered (green) measurements of EHA operating under the normal condition are provided in Figure 6-23.

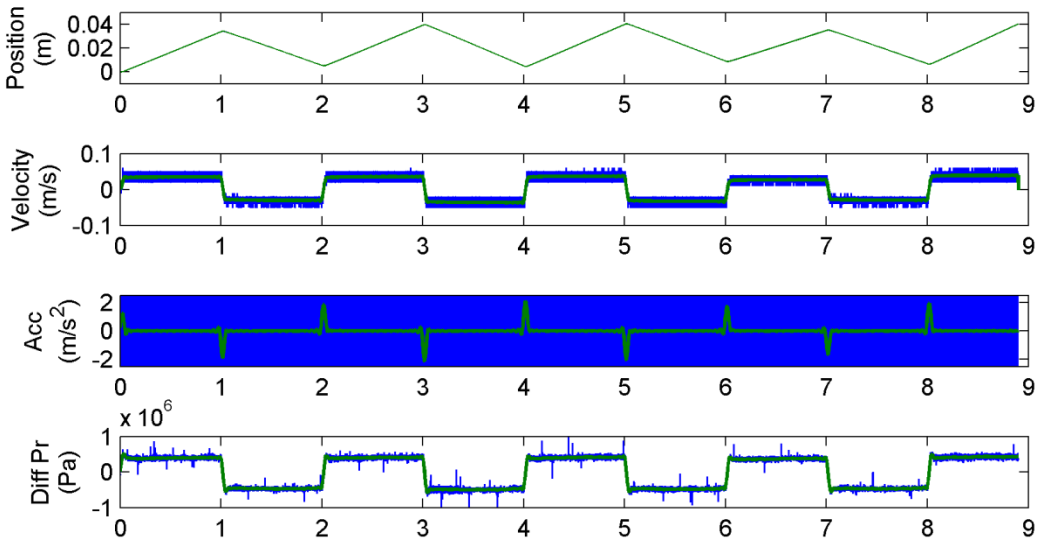

Figure 6-23: Measurement set of EHA operated under normal condition

6.2.1 Varying Amplitude Test with Unfiltered Measurement

All of the three proposed strategies (IMM-EKF, IMM-SVSF (VBL), and IMM-SVSF (FBL)) were tested with unfiltered measurements. Their mode probability results for normal operation are plotted respectively in Figure 6-24. The mode probabilities μ were used as the indication of the operating mode. A fault was considered as being successfully detected if its corresponding mode probability was the highest. The purpose of this test is to examine the proposed strategies' FDD performances at different operation region. As such case, the EHA was retained under one operating mode but in a wider operating region during each test.

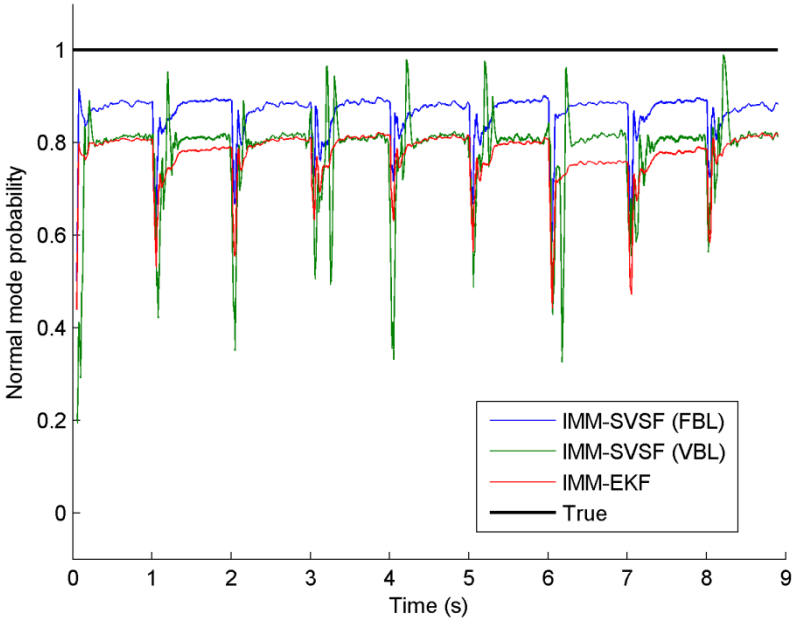

Note: EHA was operated under **normal condition**

Figure 6-24: Normal mode probability for the EHA fault detection and diagnosis experiment

Figure 6-24 shows detection under the normal mode probability for the IMM-EKF, the IMM-SVSF (FBL) and the IMM-SVSF (FBL) respectively. All of the strategies were implemented with unfiltered measurements. The 'True' mode state is plotted in black. Since the EHA was operated under normal condition during the test, the 'True' state of normal mode probability retained as 1. Outstanding results were observed and all three strategies correctly detected the normal mode with high probabilities (over 70%). Besides, the normal mode was detected with consistent probabilities at all operating regions. The mode probabilities of the incorrect modes were relatively small compared to the correct mode probability and therefore only the normal mode probabilities are shown.

The test pertaining to the EHA operated under different working conditions are provided in Figure 6-25 to Figure 6-32.

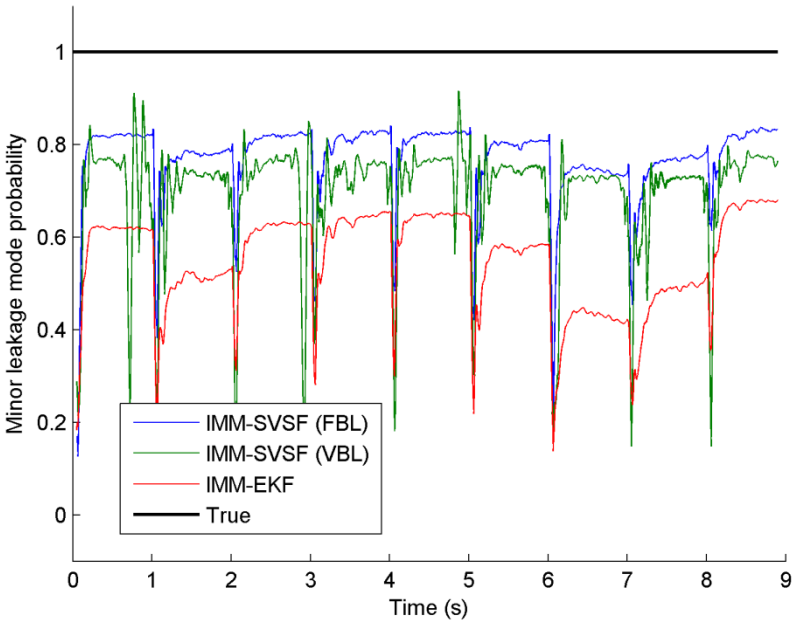

EHA was operated under **minor leakage condition**

Figure 6-25: Minor leakage mode probability for the EHA fault detection and diagnosis experiment

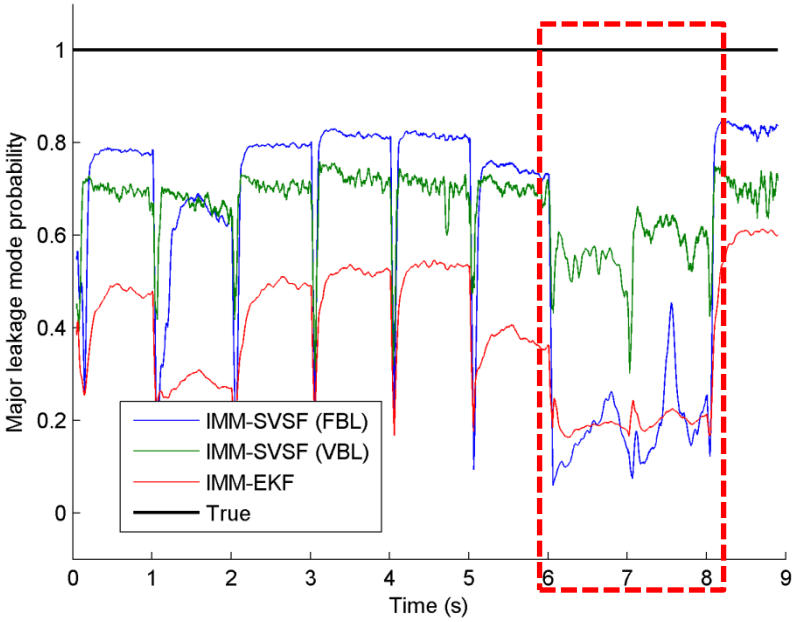

EHA was operated under **major leakage condition**

Figure 6-26: Major leakage mode probability for the EHA fault detection and diagnosis experiment

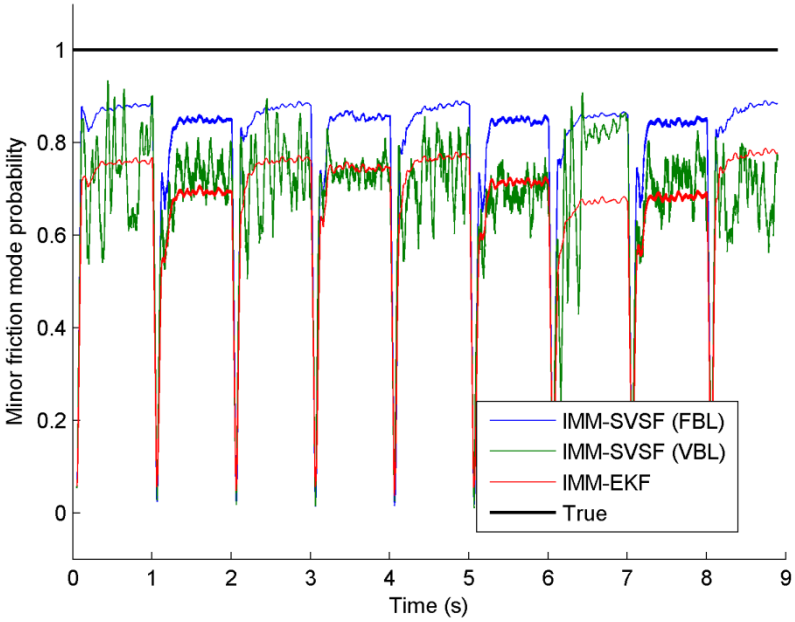

EHA was operated under **minor friction condition**

Figure 6-27: Minor friction mode probability for the EHA fault detection and diagnosis experiment

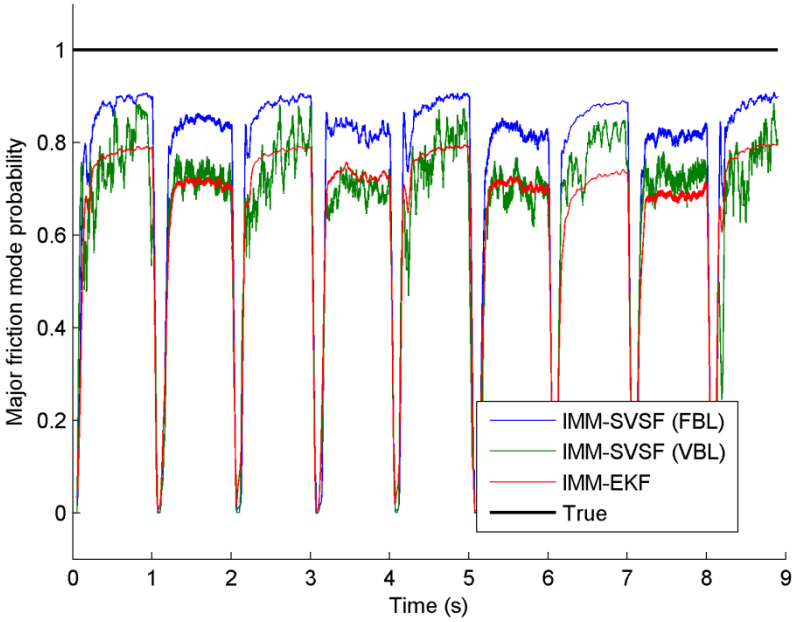

EHA was operated under **major friction condition**

Figure 6-28: Major friction mode probability for the EHA fault detection and diagnosis experiment

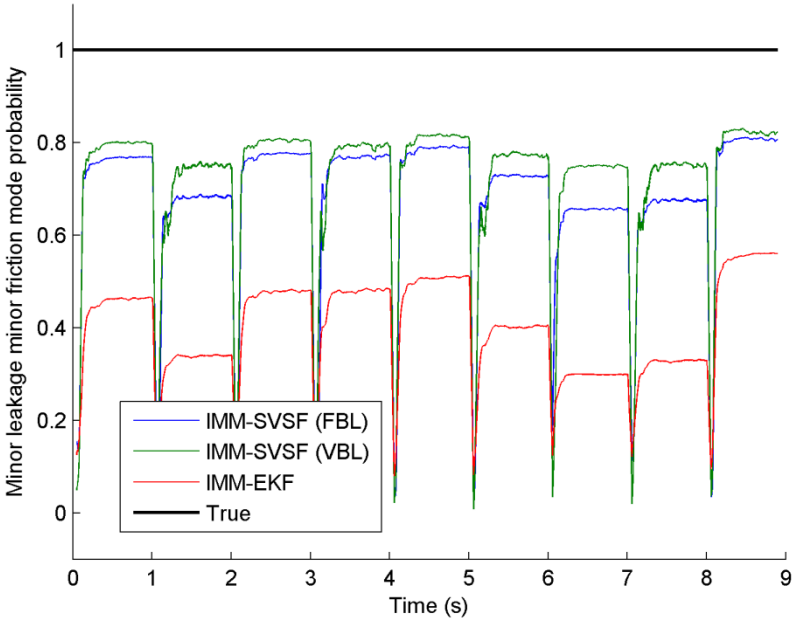

EHA was operated under **minor leakage minor friction condition**

Figure 6-29: Minor leakage minor friction mode probability for the EHA fault detection and diagnosis experiment

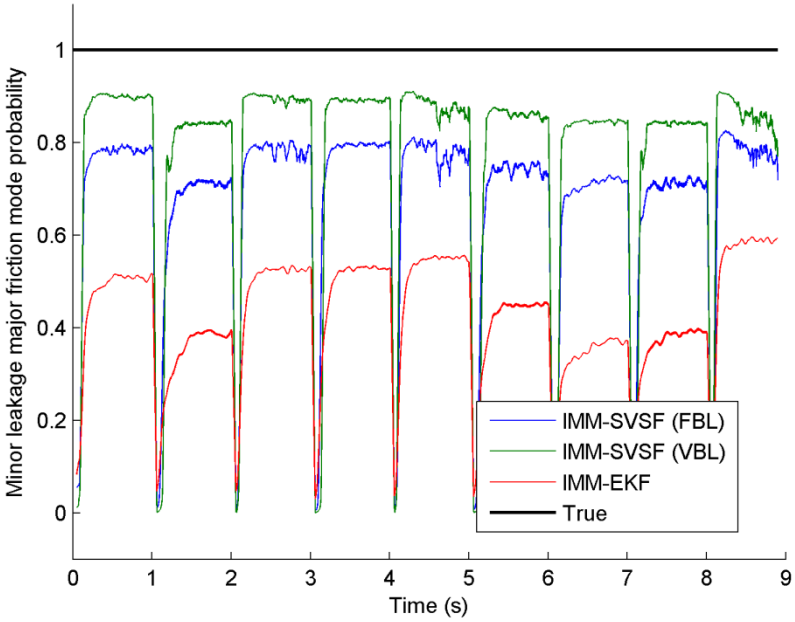

EHA was operated under **minor leakage major friction condition**

Figure 6-30: Minor leakage major friction mode probability for the EHA fault detection and diagnosis experiment

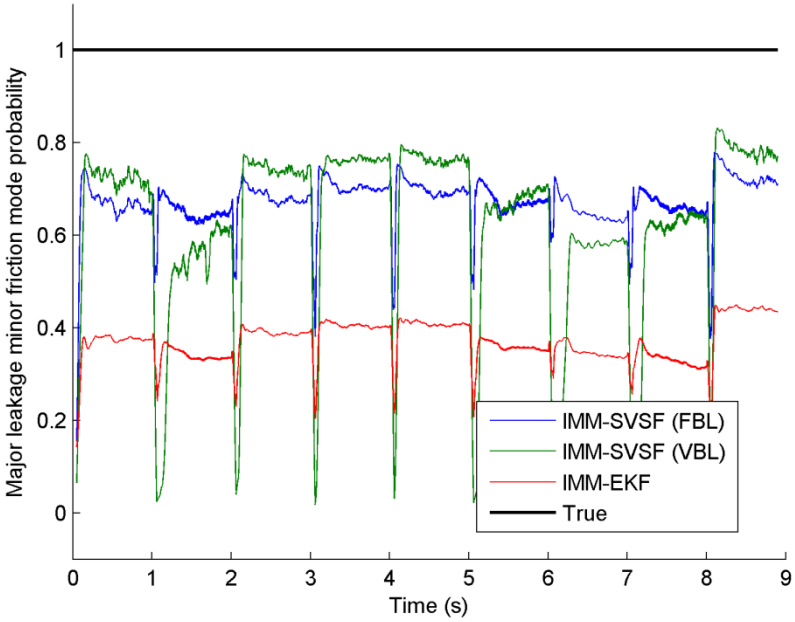

EHA was operated under **major leakage minor friction condition**

Figure 6-31: Major leakage minor friction mode probability for the EHA fault detection and diagnosis experiment

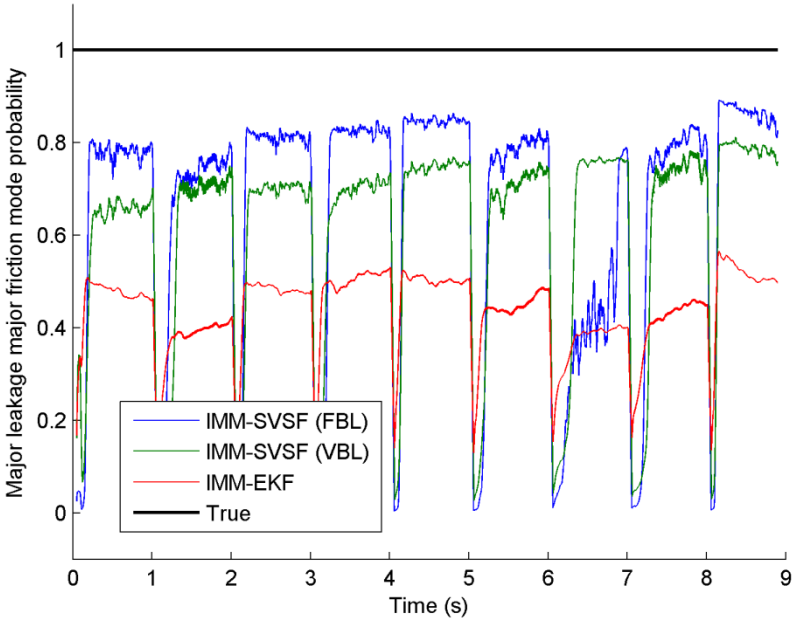

EHA was operated under **major leakage major friction condition**

Figure 6-32: Major leakage major friction mode probability for the EHA fault detection and diagnosis experiment

According to the test results, all the three proposed strategies had consistent FDD performances with most of the working conditions except the major leakage condition. Based on the major leakage mode probabilities demonstrated in Figure 6-26, it is interesting to find that the IMM-EKF and the IMM-SVSF (FBL) failed to identify the major leakage fault correctly occurring during the 6^{th} and 7^{th} seconds (highlighted by red dashed line in Figure 6-26). Recall that in section 5.4.1, the major leakage physical model showed an offset when the input amplitude was low and the EHA was operated close to its dead-band region. Since the EKF is not robust to modeling uncertainties, IMM-EKF failed to track the velocity correctly under major leakage condition close to this non-linearity. Although the SVSF is designed to be robust to modeling uncertainties, the SVSF (FBL) also failed because of the large fixed boundary layer. On the other hand, IMM-SVSF (VBL) showed great robustness to modeling uncertainties and correctly detected the major leakage fault consistently.

In order to compare the overall fault detection performances, the mean value of each mode probability was calculated in each test. All of the nine sets of test results were combined and placed in a confusion matrix as shown in Table 6-14 to Table 6-16. According to these results, all the three strategies correctly identify all of the nine working conditions. IMM-EKF has difficulties in identifying the major leakage, and the four combined faults (1. the minor leakage combined with minor friction, 2. the minor leakage combined with major friction, 3. the major leakage combined with minor friction, and 4. the major leakage combined with major friction) by having its correct mode probabilities lower than 45%. The performances of IMM-SVSF (VBL) and IMM-SVSF (FBL) were better by having the correct mode probabilities over 60%. Note that, the mode probability values listed in the confusion matrices are mean values of the results in each test. Although the IMM-SVSF (FBL) failed to correctly detect major leakage working condition during the 6^{th} and 7^{th} seconds in Figure 6-26, its aggregated capability

of correctly detecting this condition over the entire 10 seconds was high as listed in Table 6-16.

Table 6-14: IMM-EKF performance with unfiltered measurement

IMM-EKF (Mode probability)		Operating condition								
		Normal	Minor Leakage	Major Leakage	Minor Friction	Major Friction	Min. L. Min. F.	Min. L. Maj. F.	Maj. L. Min. F.	Maj. L. Maj. F.
Model condition	Normal	**77.45%**	7.41%	8.93%	1.80%	0.34%	1.72%	0.34%	1.67%	0.34%
	Minor Leakage	6.83%	**54.79%**	15.08%	4.79%	1.73%	7.11%	1.91%	5.85%	1.91%
	Major Leakage	3.85%	6.88%	**38.50%**	3.91%	3.19%	8.99%	5.64%	20.83%	8.21%
	Minor Friction	3.69%	3.79%	2.72%	**67.23%**	1.29%	10.23%	1.33%	8.38%	1.34%
	Major Friction	2.75%	1.79%	1.64%	3.31%	**64.98%**	2.61%	11.51%	2.67%	8.73%
	Min. L. Min. F.	4.57%	9.11%	8.54%	7.30%	4.50%	**39.62%**	6.70%	13.55%	6.10%
	Min. L. Maj. F.	3.27%	4.85%	4.17%	5.71%	8.34%	10.11%	**42.20%**	8.47%	12.89%
	Maj. L. Min. F.	3.44%	5.43%	14.52%	3.62%	3.72%	8.03%	8.01%	**36.91%**	16.32%
	Maj. L. Maj. F.	3.10%	4.45%	9.73%	3.16%	3.62%	6.06%	7.99%	18.55%	**43.34%**

Table 6-15: IMM-SVSF (VBL) performance with unfiltered measurement

IMM-SVSF (VBL) (Mode probability)		**Operating condition**								
		Normal	Minor Leakage	Major Leakage	Minor Friction	Major Friction	Min. L. Min. F.	Min. L. Maj. F.	Maj. L. Min. F.	Maj. L. Maj. F.
Model condition	Normal	**78.18%**	11.67%	10.07%	0.03%	0.00%	0.03%	0.00%	0.03%	0.00%
	Minor Leakage	13.88%	**69.63%**	15.80%	0.24%	0.02%	0.20%	0.02%	0.20%	0.02%
	Major Leakage	12.19%	15.55%	**65.85%**	1.58%	0.24%	1.78%	0.24%	2.34%	0.24%
	Minor Friction	1.39%	1.38%	1.49%	**67.78%**	0.08%	17.36%	0.07%	10.39%	0.06%
	Major Friction	1.11%	1.56%	1.73%	2.24%	**64.88%**	1.64%	10.30%	0.89%	15.64%
	Min. L. Min. F.	1.61%	2.24%	1.96%	8.53%	0.17%	**71.65%**	0.17%	13.50%	0.17%
	Min. L. Maj. F.	1.16%	1.10%	1.09%	1.35%	5.87%	2.44%	**77.49%**	2.33%	7.17%
	Maj. L. Min. F.	4.32%	4.71%	8.25%	7.35%	0.83%	10.31%	0.86%	**62.48%**	0.88%
	Maj. L. Maj. F.	1.98%	1.94%	2.83%	2.61%	4.75%	3.15%	7.71%	9.99%	**65.05%**

Table 6-16: IMM-SVSF (FBL) performance with unfiltered measurement

IMM-SVSF (FBL) (Mode probability)		**Operating condition**								
		Normal	Minor Leakage	Major Leakage	Minor Friction	Major Friction	Min. L. Min. F.	Min. L. Maj. F.	Maj. L. Min. F.	Maj. L. Maj. F.
Model condition	Normal	**86.41%**	5.80%	6.50%	0.39%	0.04%	0.41%	0.04%	0.36%	0.04%
	Minor Leakage	4.78%	**76.94%**	11.11%	1.61%	0.35%	2.24%	0.37%	2.21%	0.37%
	Major Leakage	2.46%	4.97%	**60.76%**	2.20%	1.26%	4.39%	1.86%	19.74%	2.36%
	Minor Friction	3.09%	1.58%	1.09%	**79.54%**	0.23%	7.63%	0.23%	6.38%	0.24%
	Major Friction	2.73%	1.36%	0.64%	2.79%	**74.95%**	1.24%	8.03%	1.85%	6.42%
	Min. L. Min. F.	2.68%	4.90%	4.07%	5.06%	1.45%	**68.23%**	1.81%	9.93%	1.88%
	Min. L. Maj. F.	1.47%	2.87%	1.49%	3.03%	7.23%	4.02%	**68.03%**	4.69%	7.16%
	Maj. L. Min. F.	2.14%	3.85%	7.61%	2.46%	2.02%	5.62%	3.59%	**67.02%**	5.69%
	Maj. L. Maj. F.	1.76%	2.94%	3.55%	2.27%	2.50%	4.03%	5.08%	17.16%	**60.71%**

6.2.2 Varying Amplitude Test with Filtered Measurement

Filtered measurements were fed to the three strategies for better fault detection performance. The test results are shown in Figure 6-33 to Figure 6-41. Note that the mode probabilities of the incorrect modes were small compared to the correct mode probabilities, and therefore only the correct mode probabilities are shown.

According to the results plotted in Figure 6-33, all of the three FDD strategies successfully detected normal mode with generally consistent and high (over 80%) normal mode probabilities.

The test for the other eight working conditions were similarly carried out and the results are shown in Figure 6-34 to Figure 6-41. All of the three fault detection strategies had improved probabilities of correctly detecting the fault conditions with filtered measurements. Only the IMM-SVSF (VBL) successfully detected the major leakage fault at all operating regions.

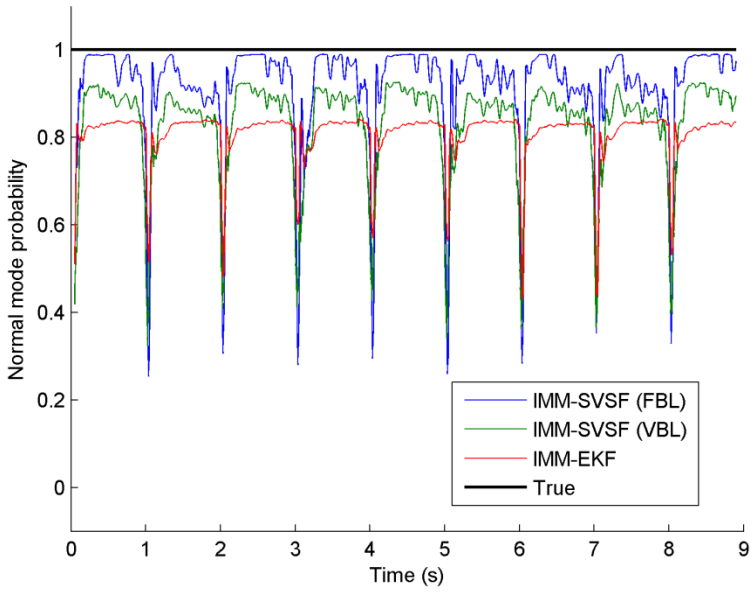

Note: EHA was operated under **normal condition**

Figure 6-33: Normal mode probability for the EHA fault detection and diagnosis experiment

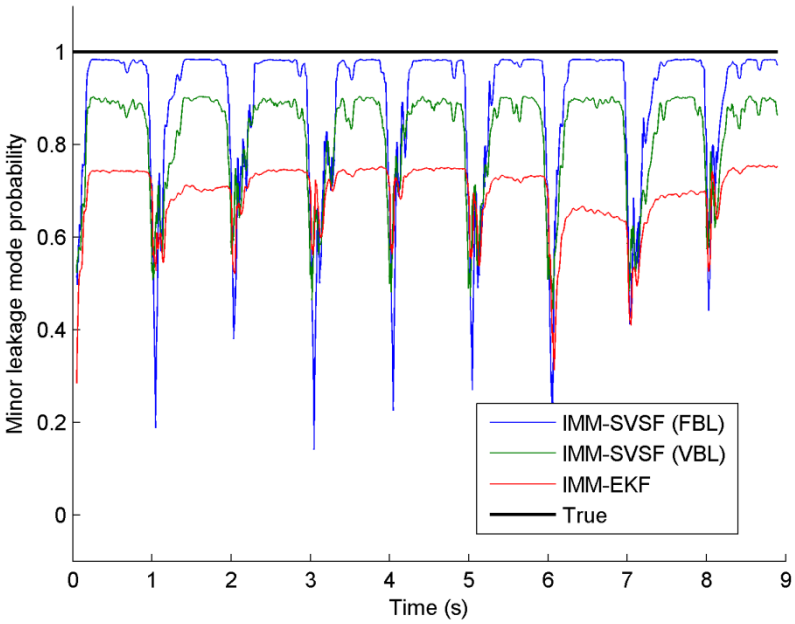

EHA was operated under **minor leakage condition**

Figure 6-34: Minor leakage mode probability for the EHA fault detection and diagnosis experiment

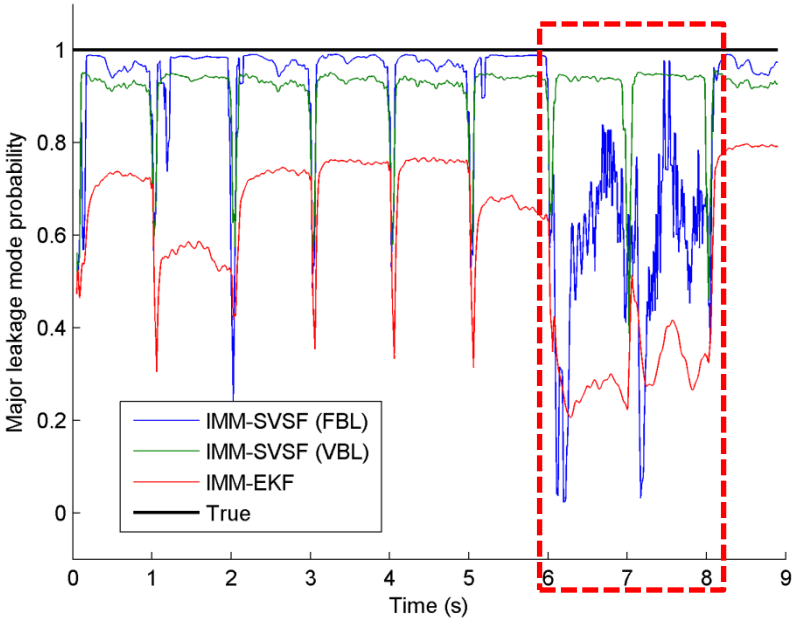

EHA was operated under **major leakage condition**

Figure 6-35: Major leakage mode probability for the EHA fault detection and diagnosis experiment

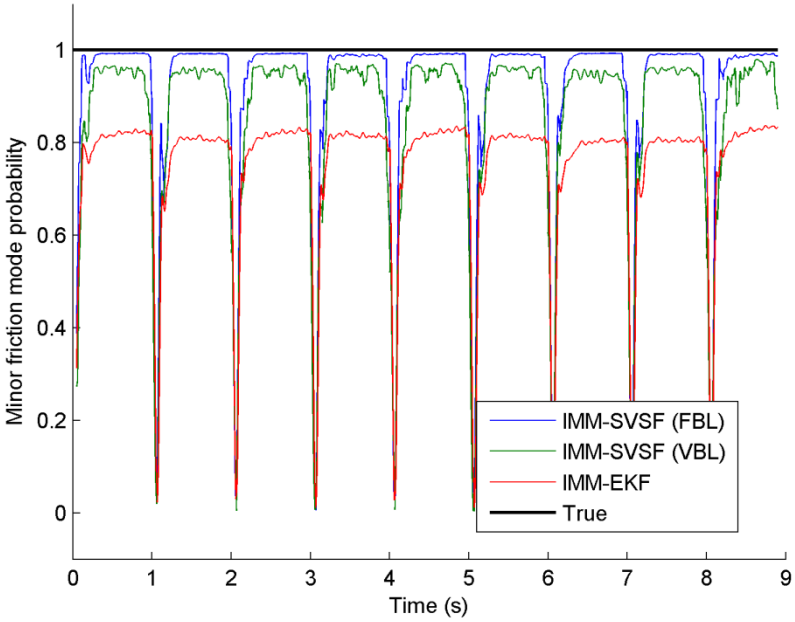

EHA was operated under **minor friction condition**

Figure 6-36: Minor friction mode probability for the EHA fault detection and diagnosis experiment

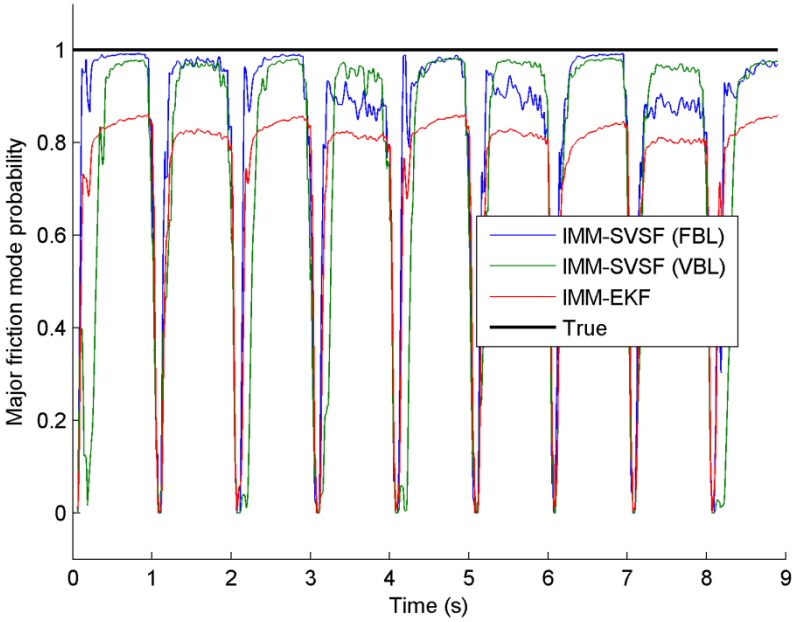

EHA was operated under **major friction condition**

Figure 6-37: Major friction mode probability for the EHA fault detection and diagnosis experiment

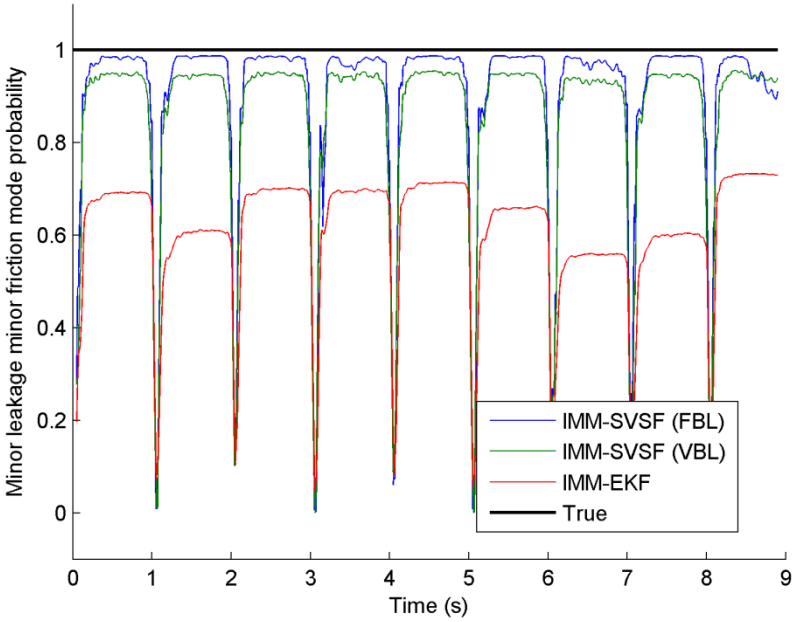

EHA was operated under **minor leakage minor friction condition**

Figure 6-38: Minor leakage minor friction mode probability for the EHA fault detection and diagnosis experiment

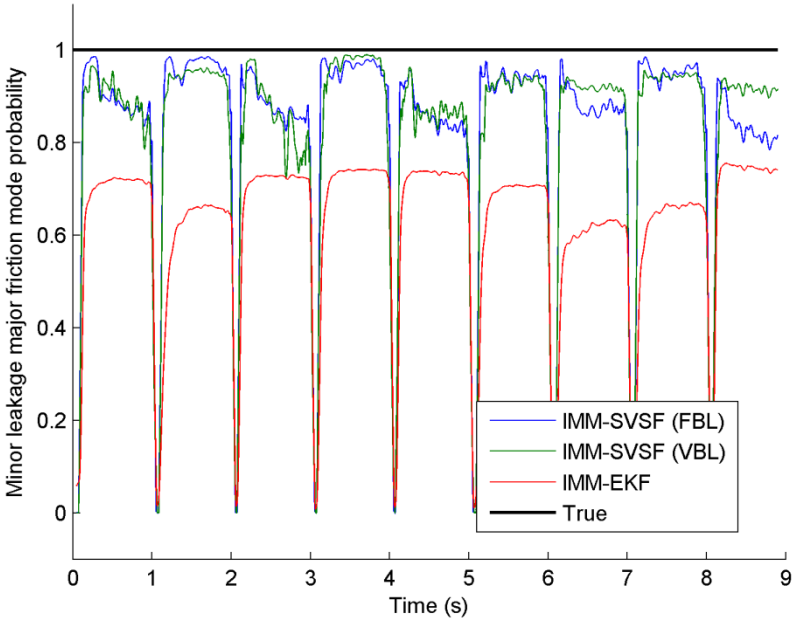

EHA was operated under **minor leakage major friction condition**

Figure 6-39: Minor leakage major friction mode probability for the EHA fault detection and diagnosis experiment

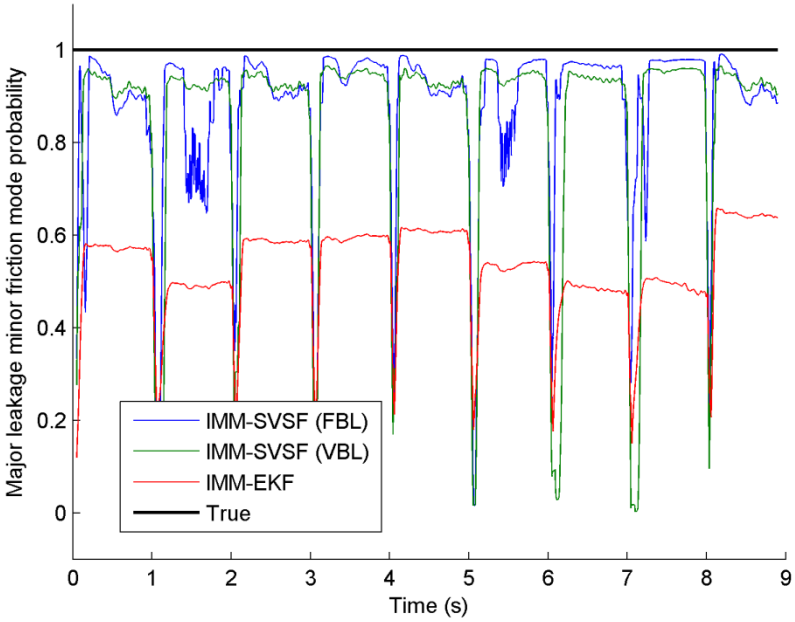

EHA was operated under **major leakage minor friction condition**

Figure 6-40: Major leakage minor friction mode probability for the EHA fault detection and diagnosis experiment

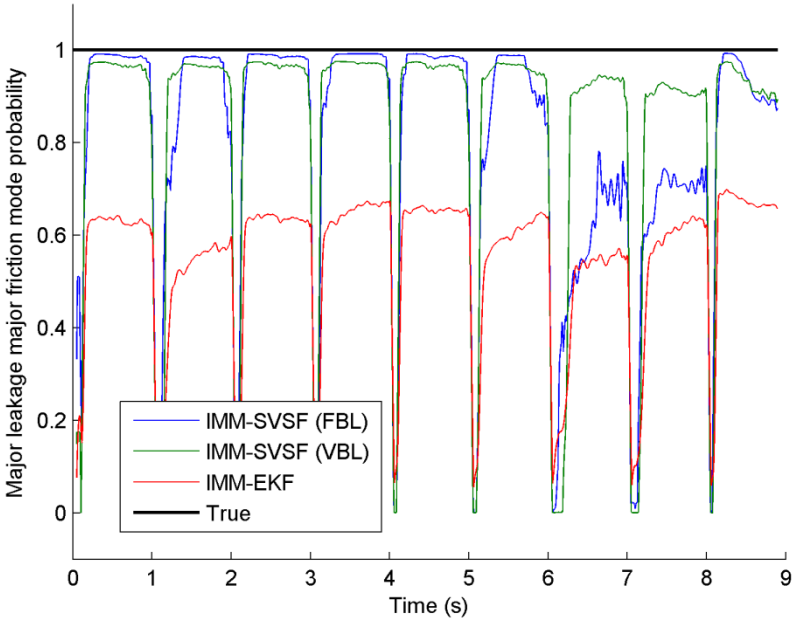

EHA was operated under **major leakage major friction condition**

Figure 6-41: Major leakage major friction mode probability for the EHA fault detection and diagnosis experiment

Table 6-17: IMM-EKF performance with filtered measurement

IMM-EKF (Mode probability)		Operating condition								
		Normal	Minor Leakage	Major Leakage	Minor Friction	Major Friction	Min. L. Min. F.	Min. L. Maj. F.	Maj. L. Min. F.	Maj. L. Maj. F.
Model condition	Normal	**80.79%**	6.60%	4.20%	2.62%	1.70%	2.66%	1.17%	3.47%	2.57%
	Minor Leakage	8.47%	**69.40%**	7.45%	1.84%	1.38%	5.37%	2.94%	5.38%	3.42%
	Major Leakage	9.47%	17.02%	**60.23%**	1.10%	0.94%	3.79%	1.47%	12.67%	6.42%
	Minor Friction	0.38%	1.68%	2.97%	**74.75%**	2.39%	7.33%	3.00%	3.86%	3.13%
	Major Friction	0.05%	0.37%	1.48%	0.24%	**72.65%**	1.60%	8.03%	2.64%	3.67%
	Min. L. Min. F.	0.38%	2.08%	5.38%	10.34%	1.73%	**60.78%**	4.34%	8.60%	5.32%
	Min. L. Maj. F.	0.05%	0.38%	2.04%	0.24%	10.28%	1.96%	**62.38%**	4.38%	8.18%
	Maj. L. Min. F.	0.37%	2.07%	13.86%	8.63%	1.32%	14.42%	4.42%	**52.78%**	12.59%
	Maj. L. Maj. F.	0.05%	0.39%	2.39%	0.25%	7.61%	2.08%	12.24%	6.22%	**54.69%**

Table 6-18: IMM-SVSF (VBL) performance with filtered measurement

IMM-SVSF (VBL) (Mode probability)		Operating condition								
		Normal	Minor Leakage	Major Leakage	Minor Friction	Major Friction	Min. L. Min. F.	Min. L. Maj. F.	Maj. L. Min. F.	Maj. L. Maj. F.
Model condition	Normal	**83.27%**	4.69%	2.87%	1.83%	1.05%	0.46%	0.28%	0.62%	0.43%
	Minor Leakage	6.61%	**81.97%**	4.95%	0.87%	1.14%	2.39%	1.53%	1.18%	0.66%
	Major Leakage	10.12%	13.34%	**91.25%**	1.12%	0.87%	1.70%	0.73%	7.71%	2.28%
	Minor Friction	0.00%	0.00%	0.10%	**84.87%**	2.28%	3.15%	0.29%	1.82%	0.23%
	Major Friction	0.00%	0.00%	0.00%	0.17%	**75.11%**	0.00%	4.80%	0.01%	0.93%
	Min. L. Min. F.	0.00%	0.00%	0.16%	6.55%	1.98%	**85.69%**	1.86%	4.13%	0.61%
	Min. L. Maj. F.	0.00%	0.00%	0.00%	0.24%	11.58%	0.00%	**82.49%**	0.01%	3.92%
	Maj. L. Min. F.	0.00%	0.00%	0.67%	4.17%	1.05%	6.60%	2.47%	**84.42%**	7.87%
	Maj. L. Maj. F.	0.00%	0.00%	0.00%	0.19%	4.95%	0.00%	5.55%	0.09%	**83.07%**

Table 6-19: IMM-SVSF (FBL) performance with filtered measurement

IMM-SVSF (FBL) (Mode probability)		**Operating condition**								
		Normal	Minor Leakage	Major Leakage	Minor Friction	Major Friction	Min. L. Min. F.	Min. L. Maj. F.	Maj. L. Min. F.	Maj. L. Maj. F.
Model condition	Normal	**91.09%**	2.07%	0.85%	1.97%	1.78%	0.24%	0.14%	0.55%	0.45%
	Minor Leakage	3.65%	**89.02%**	1.92%	1.38%	0.97%	1.98%	1.39%	0.96%	0.93%
	Major Leakage	3.70%	8.05%	**85.66%**	0.85%	1.15%	1.88%	0.82%	6.61%	4.00%
	Minor Friction	0.20%	0.25%	0.35%	**90.54%**	2.29%	1.63%	0.43%	0.87%	0.56%
	Major Friction	0.25%	0.05%	0.10%	0.13%	**82.72%**	0.01%	5.44%	0.08%	1.00%
	Min. L. Min. F.	0.11%	0.09%	0.35%	2.29%	1.66%	**89.62%**	2.14%	2.93%	0.83%
	Min. L. Maj. F.	0.62%	0.26%	0.02%	0.09%	5.22%	0.01%	**82.77%**	0.16%	2.16%
	Maj. L. Min. F.	0.16%	0.12%	10.57%	2.72%	0.99%	4.61%	2.27%	**87.19%**	10.54%
	Maj. L. Maj. F.	0.23%	0.09%	0.17%	0.02%	3.21%	0.01%	4.61%	0.65%	**79.53%**

The overall performances of the three strategies are shown by confusion matrices in Table 6-17 to Table 6-19. Compared to their implementations with unfiltered measurements, all the three strategies had better performances. The IMM-EKF had a poor FDD performance with the presence of major leakage and had generally a lower probability of correctly detecting the fault conditions (around or below 60%). Although both the IMM-SVSF strategies had comparable overall fault detection performances, the IMM-SVSF (VBL) was the only strategy that was consistently excellent for all nine working condition in all operation regions. Note that, although the IMM-SVSF (FBL) failed to detect major leakage during the 6^{th} and 7^{th} seconds in Figure 6-35 (corresponding to an operating region close to the actuator dead-zone), the aggregated probability of correctly detecting the major leakage condition was still high as provided in Table 6-19.

The IMM-EKF and the IMM-SVSF (FBL) identified most of the working conditions consistently and correctly, except for the major leakage. When the major leakage fault was present with a low input amplitude, both of these two strategies failed (during 6^{th} and 7^{th} seconds in Figure 6-35). The incorrect detection is believed to be caused by the uncertainties in the model due to dead-zone associated with the major leakage. On the other hand, the IMM-SVSF (VBL) successfully detected all conditions with consistently high correct mode probabilities at all operating regions. It showed excellent robustness to changes in operating conditions and modeling uncertainties.

6.3 Fault Detection and Diagnosis with Growing Leakage

In sections 6.1 and 6.2, the three fault detection strategies were tested with inputs having both fixed and varying amplitudes. The prototype was operating under nine predefined conditions. However, it is not practical to assume that the EHA would always run under these conditions. In fact, faults can result in changing conditions and grow in time. With this concern, a growing leakage fault was investigated in this section.

As described in Chapter 3, leakage was simulated by letting a certain amount of fluid to bypass the cylinder. The bypass flow rate was controlled by a throttling valve. The throttling valve opening was proportional to its control input. It was fully closed with a 10V input and fully open with a 0V input. In Chapter 3, the EHA was defined to be running under normal, minor leakage and major leakage conditions with throttling valve inputs of 10V, 2V, and 1.75V respectively. Another 10 throttling voltage inputs were chosen to simulate 10 extra levels of leakage dispersed evenly between 1.65V to 10V. With the motor angular velocity constant at $109.90\ rad/set$, each leakage condition was measured as:

$$Q_{leak} = A\dot{x}_{NC} - A\dot{x} \tag{6-9}$$

where $\dot{x}_{NC}$ is the actuator velocity of the EHA running under normal condition.

The leakage percentages were calculated as:

$$\%_{leak} = \frac{Q_{leak}}{A\dot{x}_{NC}} = 1 - \frac{\dot{x}}{\dot{x}_{NC}} \tag{6-10}$$

Table 6-20 lists the 13 leakage conditions with their corresponding velocities and percentage of leakage. The time interval for each leakage condition is listed in Table 6-20.

Table 6-20: Leakage conditions

Leakage voltage input (V)	Velocity mean $(^{m}/_{sec})$	Leakage percentage	Time segment (sec)	
10	0.0372	0.00%	0-2	Normal
2.2	0.0321	13.71%	2-4	
2.15	0.0303	18.55%	4-6	
2.1	0.0288	22.58%	6-8	
2.05	0.0266	28.49%	8-10	
2	0.0245	34.14%	10-12	Minor Leakage
1.95	0.0229	38.44%	12-14	
1.9	0.0207	44.35%	14-16	
1.85	0.0189	49.19%	16-18	
1.8	0.0169	54.57%	18-20	
1.75	0.0152	59.14%	20-22	Major Leakage
1.7	0.0135	63.71%	22-24	
1.65	0.0109	70.70%	24-26	

Sequential steps with amplitude of $\pm 109.90\, rad/sec$ as shown in Figure 6-42 were used as test input.

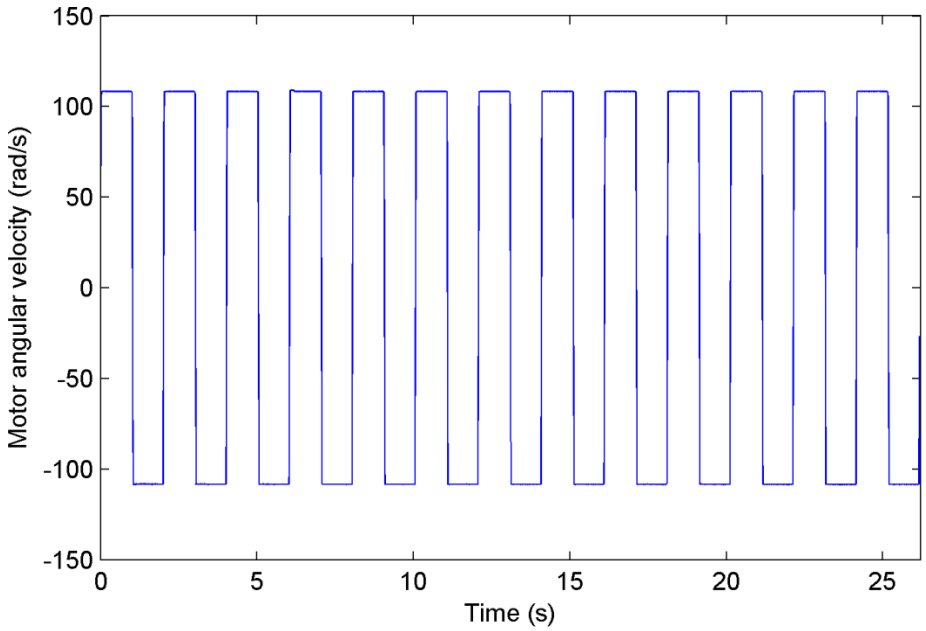

Figure 6-42: Gradual leakage test input

As shown in Figure 6-42, there were 13 cycles in total, each corresponding to one leakage condition in Table 6-20. In each cycle, the EHA was operated with its input as $109.90\ rad/sec$ for a second followed by an input as $-109.90\ rad/sec$ for another second. Filtered measurements shown in Figure 6-43 were used for all three strategies.

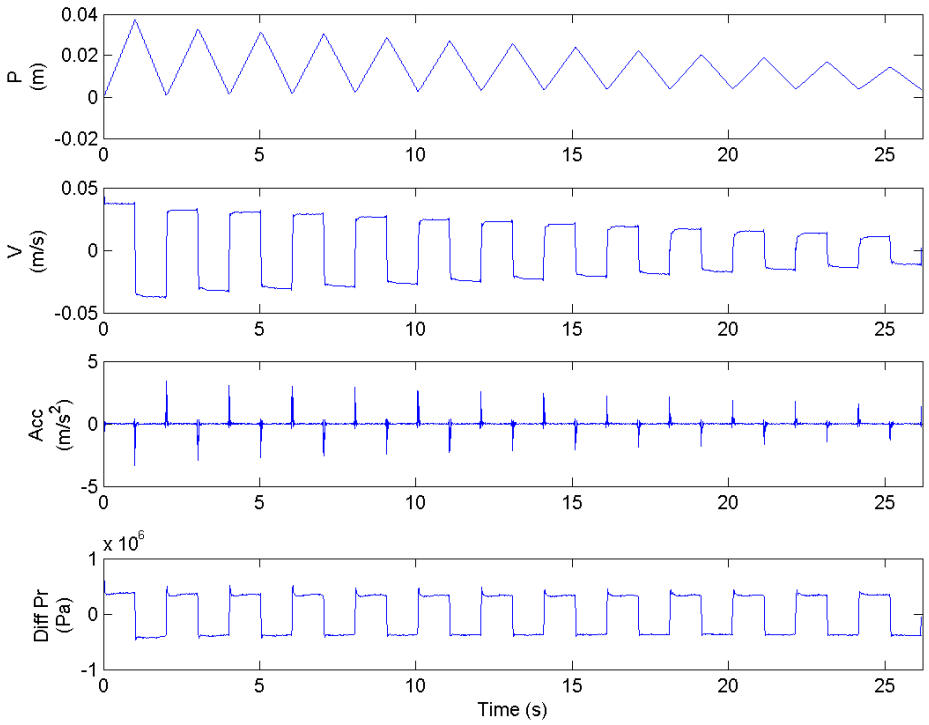

Figure 6-43: Measurement of EHA working with growing leakage

Figure 6-44 demonstrates mode probabilities resulting from the IMM-EKF. For better clarity, mean values of mode probabilities at each cycle were calculated. Since modes other than normal, minor leakage, and major leakage had probabilities close to zero, only probabilities of these three modes are shown.

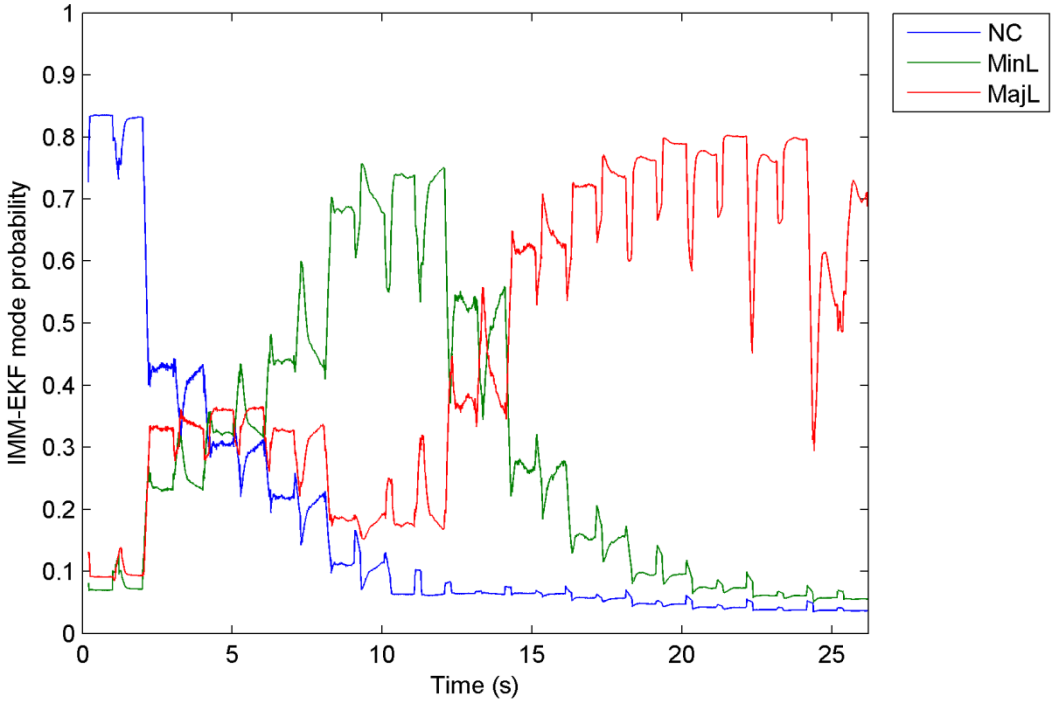

Figure 6-44: IMM-EKF mode probability with growing leakage

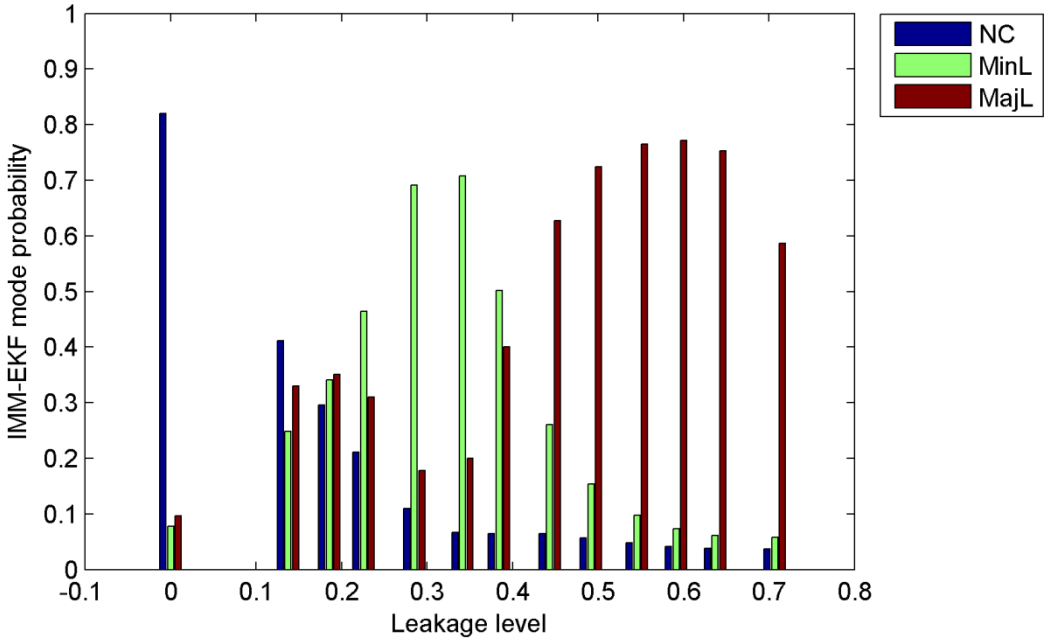

Figure 6-45: IMM-EKF mode probability mean with growing leakage

Figure 6-45 shows the mean value of the IMM-EKF aggregated mode probabilities at each leakage level. At the beginning, the system was operated normally, and the normal mode had the highest probability (blue). As the leakage was increased from 0% (Normal) to 34% (Min L), the normal mode probability decreased, and the probability of minor leakage mode (green) increased. The minor leakage mode had its peak probability at 34% leakage. When the leakage grew from 34% (Min L) to 70%, the minor leakage mode probability decreased and the major leakage mode probability moved up. The major leakage mode had its peak probability when the leakage grew to 59%. The probabilities changed from normal, to minor leakage, and then to major leakage correctly reflecting the growing leakage dynamic.

The IMM-SVSF (VBL) was implemented with the same filtered measurements and its results are plotted in Figure 6-45 andFigure 6-46.

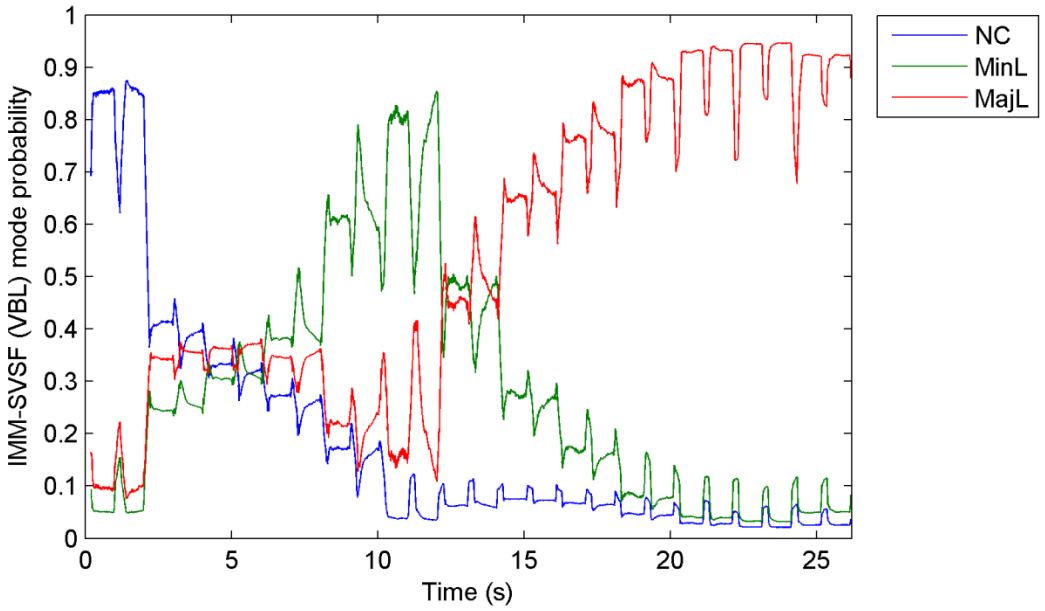

Figure 6-46: IMM-SVSF (VBL) mode probability with growing leakage

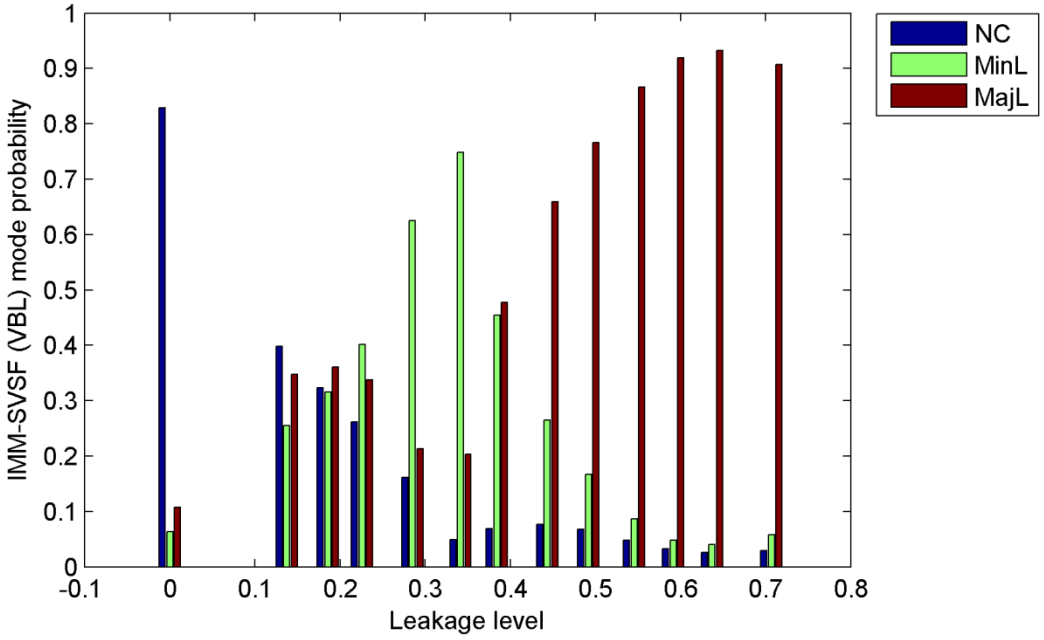

Figure 6-47: IMM-SVSF (VBL) mode probability mean with growing leakage

The IMM-SVSF (VBL) had a similar performance as IMM-EKF. The normal, minor leakage and major leakage modes had their peak probability values when the prototype was operated at corresponding conditions. Their probabilities changed gradually and correctly according to the change in the operating conditions.

IMM-SVSF (FBL) was implemented with the same filtered measurements and its results are plotted in Figure 6-48 and Figure 6-49.

Although the mode probability mean of IMM-SVSF (FBL) correctly reflected the growing leakage dynamic as in the previous two strategies in Figure 6-49, the FBL strategy mode probabilities contained significant amount of chattering when the EHA was not operated at pre-defined working conditions (Normal, Min L, and Maj L).

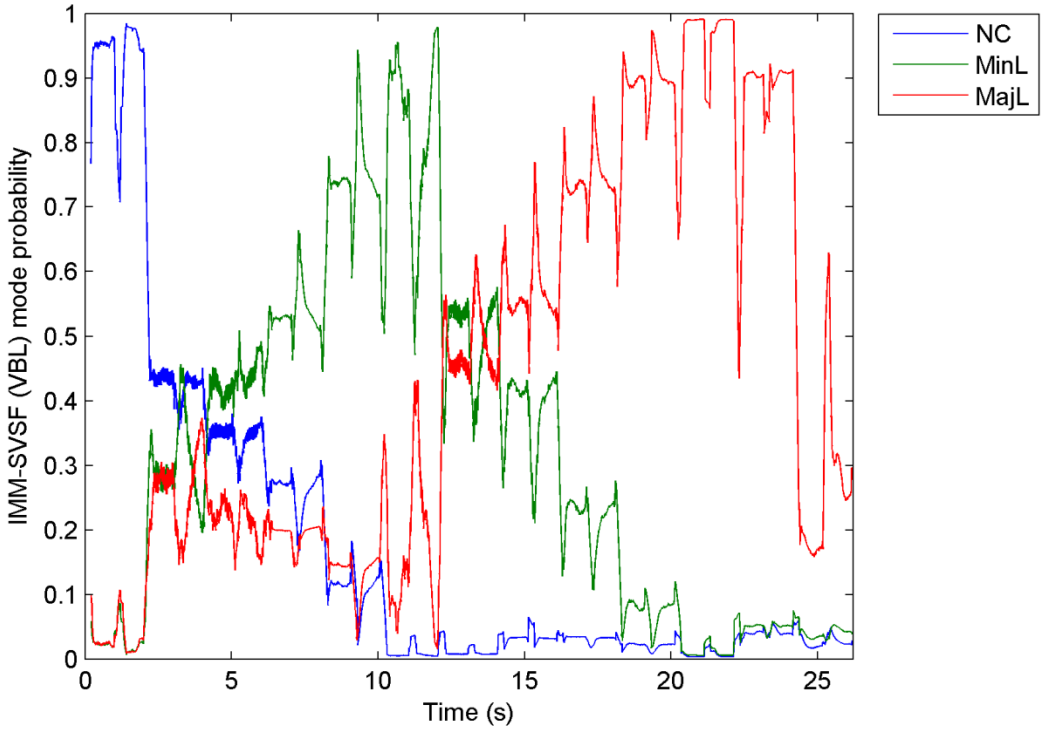

Figure 6-48: IMM-SVSF (FBL) mode probability with growing leakage

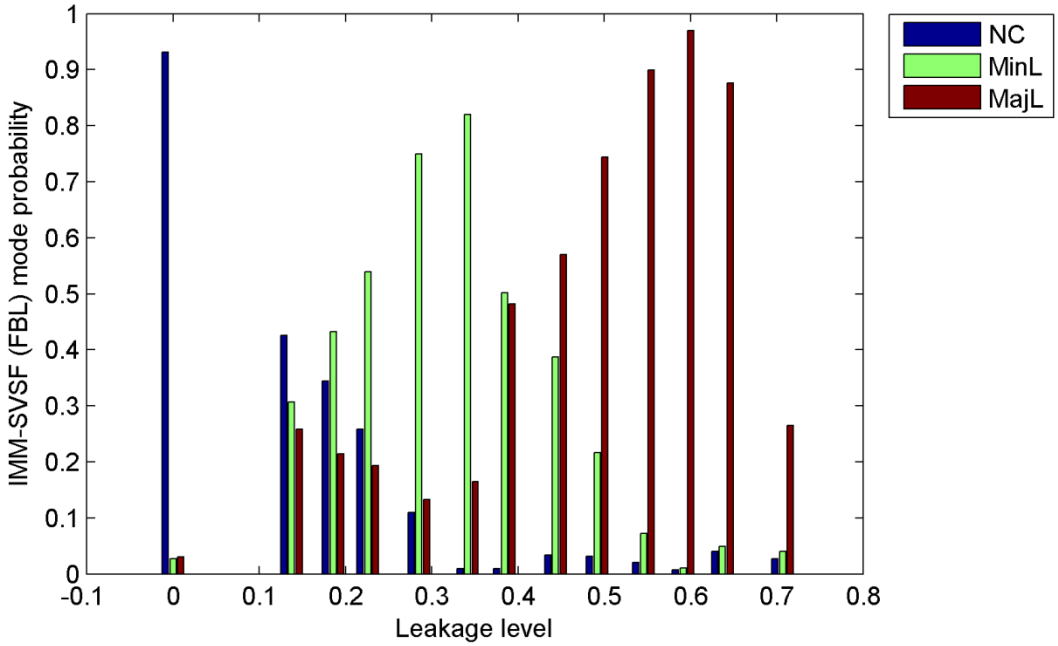

Figure 6-49: IMM-SVSF (FBL) mode probability mean with growing leakage

In this section, the EHA was operated with a growing leakage fault. All the three FDD strategies were tested with unmolded leakage conditions. Based on their mode probabilities, both the IMM-EKF and the IMM-SVSF (VBL) provided mode probabilities distributions that reflected the growing leakage fault. With the mode probability changing history, they were able to predict the growing leakage trend. Although the mode probability mean of IMM-SVSF (FBL) also captured the growing leakage, its result contained significant chattering when the prototype was not operated under modeled conditions.

6.4 Conclusion

Three fault detection and diagnosis (FDD) strategies, the IMM-EKF, IMM-SVSF (VBL) and IMM-SVSF (FBL) were implemented under three sets of tests on the EHA, and their performances were compared.

In test 1, sequential steps with fixed amplitude were used as input to the EHA prototype. The fault detection strategies were implemented with both unfiltered and filtered measurements. Their FDD and estimation performances were evaluated by using mode probabilities and estimation RMSE. All three strategies correctly detected all of the nine working conditions. The IMM-SVSF (FBL) provided the best FDD performance by having the highest correct mode probabilities. However, with a comparable detection performance, the IMM-SVSF (VBL) provided the best estimation performance amongst the three.

In test 2, sequential steps with varying amplitudes were used for testing the three strategies at different operation points. Both IMM-EKF and IMM-SVSF (FBL) identified most of the working conditions consistently and correctly with the exception of the major leakage fault. When the major leakage fault was present with low amplitude input both of these strategies failed to detect it. The miss-

diagnosis is believed to have been caused by the modeling uncertainties of dead-zone non-linearity due to the major leakage. On the other hand, the IMM-SVSF (VBL) successfully detected and diagnosed all nine conditions consistently and correctly with high mode probabilities for all operations. It showed excellent robustness to changing conditions and modeling uncertainties.

In test 3, the EHA was operated with growing leakage. All the three fault detection strategies were tested with unmolded leakage conditions. Based on their mode probabilities, both the IMM-EKF and the IMM-SVSF (VBL) had mode probability distributions that reflected a growing leakage dynamic. Although the aggregated mode probability distribution of the IMM-SVSF (FBL) also captured the growing leakage, it contained significant chattering in the unmolded range of the EHA operation.

Based on the test results, the IMM-SVSF (VBL) provided the best overall performance. It detected and diagnosed faults correctly with high mode probabilities with excellent robustness to modeling uncertainties. In addition, it was also able to detect slow growing leakage.

7 Conclusion and Future recommendation

7.1 Summary of research

The research objectives were the development of a fault detection and diagnosis (FDD) system and its application on an experimental Electro-hydrostatic actuation (EHA) system. After an investigation of fault detection strategies in Chapter 2, an estimation strategy based on the Interacting Multiple Model approach was chosen. The reason was that state estimation combined with IMM can be applied in real-time for online fault detection as well as diagnosis. The approach was applied on the EHA, but it is believed to be applicable to other systems.

The EHA prototype and its mechanism was studied and introduced in Chapter 4. Two common faults, internal leakage and friction, were simulated with throttling valves and auxiliary circuits. The internal leakage and friction effects were physically simulated and tested experimentally. Nine working conditions were defined and tested.

In Chapter 5, two types of models were obtained based on prior knowledge of the EHA. The first type was a physical model derived mathematically. Parameters in physical models have physical meanings and provide a mechanism for understanding the dynamic effects in the system. For comparison purposes, parametric models were also obtained through system identification. Parametric models can be very accurate and easy to obtain; however, the parameters cannot be explicitly linked to physical effects. Each type considered nine different operating conditions. After performing model validation, it was found that both physical and parametric models were accurate. However, the EHA was found to have numerous piece-wise linear regions according to the input amplitudes and therefore required a very large number of models for completely describing the system dynamic under the fault and operating condition considered in this research. Parametric models are not suitable for FDD due to the large number of

models needed and the resulting computation complexity. Furthermore, the physical model was able to provide an extra mechanism for understanding system dynamics. The physical model was chosen for EHA FDD.

Three fault detection and diagnosis strategies were proposed using model based filter, namely the IMM-EKF, the IMM-SVSF (VBL) and the IMM-SVSF (FBL). All of these three strategies were implemented on the EHA and their performances were compared using the three tests previously mentioned.

In test 1, step inputs with fixed amplitude were used. The FDD strategies were implemented with both unfiltered and filtered measurements. Their FDD and estimation performances were evaluated using mode probabilities and estimation RMSE. All three strategies correctly detected the system change and diagnosed all the nine working conditions. The IMM-SVSF (FBL) provided the best FDD performance by having the highest correct mode probabilities. The IMM-SVSF (VBL) closely followed, but provided the best estimation performance amongst the three.

In test 2, step inputs with varying amplitudes were used to test the three strategies at different operating regions. Both the IMM-EKF and the IMM-SVSF (FBL) correctly identified most of the fault conditions, except for the major leakage fault. The IMM-SVSF (VBL) was the only method successfully diagnosed all nine conditions with consistently high mode probabilities at all operation regions. It showed excellent robustness to changes in operation conditions and modeling uncertainties.

In test 3, the EHA was operated with growing leakage. All the three FDD strategies were tested with unmodeled leakage. Based on their mode probabilities both the IMM-EKF and the IMM-SVSF (VBL) successfully detected the growing leakage. Although the IMM-SVSF (FBL) also captured the growing leakage, it contained significant chattering.

Based on the tests results, the IMM-SVSF (VBL) is proved to be the best strategy amongst the three tested. It detected system changes and diagnosed faults correctly with high mode probabilities and was robust to modeling uncertainties. It also successfully tracked and detected a gradually increasing leakage fault.

7.2 Future recommendation

This thesis presented the development of a fault detection and diagnosis (FDD) system for Electro-hydrostatic actuation (EHA) systems. With the FDD, a significant amount of research remains.

The first recommendation involves a consideration of changing external load. In this research, the EHA was operated with constant external load. When the EHA is applied for flight surface control, a varying external load is seen due to changing drag and lift. A consideration of external load is important because it affects the differential pressure in the actuator.

The second recommendation involves the fault detection and diagnosis with a changing effective bulk modulus. The effective bulk modulus is a measure of the fluid compressibility and its value changes with the volume of trapped air. Since the volume of trapped air is unpredictable, the change in the effective bulk modulus becomes extremely difficult to measure experimentally. In this research, the Extend Kalman Filter (EKF) was used with the physical model to estimate the effective bulk modulus in Section 5.2.3. The effective bulk modulus estimation can be extended to include fault conditions and combined with the developed FDD system.

The third recommendation involves the application of the FDD for developing fault tolerant control strategies. In this research nine different working conditions were successfully detected and diagnosed. The results of this thesis provide a strong starting point for fault tolerant control of the EHA. The control of the

EHA with leakage and friction faults can become an excellent extension of this research.

8 Bibliography

[1] John Loughmiler. (2009, Dec.) Emerging Technologies: Distributed Electro-Hydraulic Systems. Document. [Online]. http://www.designnews.com/document.asp?doc_id=228724&dfpPParams=ind_182,aid_228724&dfpLayout=article

[2] Hunt T.M., "A Review of Condition Monitoring Techniques Applicable to Fulid Power Systems," in *7th Interational Fluid Power Symposium*, University of Bath, Sep. 1986, pp. 285-295.

[3] Kevin Ronald McCullough, "Design and Characterization of a Dual Electro-Hydrostatic Actuator," McMaster University, Hamilton, Master Thesis 2011.

[4] John Watton, *Modelling, Monitoring and Diagnostic Techniques for Fluid Power Systems*, 1st ed. UK: Springer-Verlag London Limited, 2007.

[5] "Spectroline - Leak detection kits for industrial applications," Advanced Eningeer Limited, Basingstoke, Catalog.

[6] Merrit H. E., *Hydraulic control system*. New York, United States: John Wiley & Sons, Inc, 1967.

[7] Venkat Venkatasubramanian, Raghunathan Rengaswamy, Kewen Yin, and

Surya N. Kavuri, "A review of process fault detecion and diagnosis Prat1: Quantitative model-based methods," *Computers and Chemical Engineering*, vol. 27, pp. 293-311, 2003.

[8] David G. Luenberger, "Observing the state of a linear system," *Military Electronics, IEEE transactions*, vol. 8, no. 2, pp. 74-80, April 1964.

[9] David G. Luenberger, "An introduction to observers," *IEEE transactions on Automatic control*, vol. AC-16, no. 6, pp. 596-602, December 1971.

[10] P. M. Frank and X. Ding, "Survey of robust residual generation and evaluation methods in observer-based fault detection systems," *Journal of Process Control*, vol. 7, no. 6, pp. 403-424, December 1997.

[11] Ron J. Patton, Paul M. Frank, and Robert N. Clarke, *Fault diagnosis in dynamic systems: theory and application*. New Jersey, USA: Prentice Hall, Inc, 1989.

[12] Abbas Emami-Naeini, Muhammad M. Akther, and Stephen M. Rock, "Effect of Model Uncertainty on Failure Detection: The Threshold Selector," *IEEE transactions on automatic control*, vol. 33, no. 12, pp. 1106-1115, December 1988.

[13] Lőrinc Márton and Andreas Varga, "Detection of Overload Generated Faults in Electro-Hydrostatic Actuators," in *19th Mediterranean Conference on Control and Automation*, Corfu, Greece, 2011.

[14] H. Khan, Serphin C. Abou, and N. Sepehri, "Nonlinear observer-based fault detection technique for electro-hydraulic servo-positioning system,"

Mechatronics, vol. 15, no. 9, pp. 1037-1059, Novermber 2005.

[15] M. Sibar, "Implementation of failure-detection system with adaptive observers," in *American Control Conference*, Haifa, Israel, 1983, pp. 1205-1211.

[16] Hong Wang, Zhen J. Huang, Steve Daley, "On the Use of Adaptive Updating Rules for Actuator and Sensor Fault Diagnosis," *Automatica*, vol. 33, no. 2, pp. 217-225, February 1997.

[17] R.E.Kalman, "A New Approach to Linear Filtering and Prediction Problems," *Journal of Basic Engineering, Transactions of ASME*, vol. 82, pp. 34-45, 1960.

[18] Mohinder S. Grewal and Angus P. Andrews, *Kalman Filtering - Theory and Practice Using Matlab*, 2nd ed. Toronto, Canada: John Wiley & Sons, Inc., 2001.

[19] D. Simon, *Optimal State Estimation: Kalman, H-infinity, and Nonlinear Approaches*.: Wiely Interscience, 2006.

[20] L.McGee and S.Schmidt, "Discovery of the Kalman Filter as a Practical Tool for Aerospace and Industry," NASA, Technical Memo 86847, 1985.

[21] S. A. Gadsden, "Smooth Variable Structure Filtering: Theory and Applications," Department of Mechanical Engineering, McMaster University, Hamilton, Ontario, Ph.D. Thesis 2011.

[22] Nori Okita and H.J. Sommer III, "A Novel Foot Slip Detection Algorithm Using Unscented Kalman Filter Innovation," in *2012 American Control*

Conference, Montreal, 2012, pp. 5163-5168.

[23] Mohammed Sepasi, *Fault Monitoring in Hydraulic Systems using Unscented Kalman Filter*. Vancouver, Canada / British Columbia: University of British Columbia, 2007.

[24] Mohammed Sepasi and Farrokh Sassani, "On-line Fault Diagnosis of Hydraulic System Using Unscented Kalman Filter," *International Journal of Contrl, Automation, and Systems*, vol. 8, no. 1, pp. 149-156, 2010.

[25] Y. A. Chinniah, "Fault Detection in the Electrohydraulic Actuator Using the Extended Kalman Filter," Department of Mechanical Engineering, University of Saskatchewan, Saskatoon, Saskatchewan, Ph.D. Thesis 2004.

[26] S. R. Habibi, "The Smooth Variable Structure Filter," *Proceedings of the IEEE*, vol. 95, no. 5, pp. 1026-1059, 2007.

[27] Greg Welch and Gary Bishop, *An Introduction to the Kalman Filter*. Chapel Hill, North Carolina: University of North Carolina at Chapel Hill.

[28] Xudong Wang and Vassilis L. Syrmos, "Fault detection, identification and estimation in the Electro-hydraulic actuator using EKF-based Multiple-Model estimation," in *16th Mediterranean Conference on Control and Automation*, Ajaccio, France, 2008, pp. 1693-1698.

[29] Youmin Zhang, and X. Rong Li, "Detection and Diagnosis of Sensor and Actuator Failure Using IMM Estimator," in *IEEE transactions on aerospace and electronic systems*, San Diego, 1998, pp. 1293-1313.

[30] Yaakov Bar-Shalom, X. Rong Li, and Thiagalingam Kirubarajan , *Estimation with Applications to Tracking and Navigation, Theory Algorithms and Software*. New York: Jonh Wiley & Sons, Inc, 2001.

[31] E. Mazor, A. Averbuch, Y. Bar-Shalom, and J. Dayan, "Interacting Multiple Model Methods in Target Tracking: Survey," *IEEE Ttransactions On Aerospace And Electronic Systems*, vol. 34, no. 1, pp. 103-123, January 1998.

[32] X. Rong Li and Vesselin P. Jilkov, "Survey of Maneuvering Target Tracking. Part V: Multiple-Model Methods," *IEEE transactions on aerospace and electronic system*, vol. 41, no. 4, pp. 1255-1321, October 2005.

[33] S.A. Gadsden, Y. Song, and S.R. Habibi, "Mathematical Modeling and Fault Detection and Diagnosis of an Electrohydrostatic Actuator," in *2012 American Control Conference*, Montreal, 2012, pp. 5152-5159.

[34] Charlotte Adams, "A380: 'More Electric' Aircraft," Avionics Today, Magzine October 2001. [Online]. http://www.aviationtoday.com/av/commercial/A380-More-Electric-Aircraft_12874.html

[35] Moog Inc. (2012) System Integrator for Lockheed Martin F-35. [Online]. http://www.moog.com/markets/aircraft/military-aircraft/fighter-trainer/system-integrator-for-lockheed-martin-f-35/

[36] Fagor Automation S. Coop, "Fagor Linear and Rotary Encoders," Fagor Automation S. Coop, Spain, Manual.

[37] Measurement Specialties, "M5100 Heavy Industrial Pressure Transducer," Measurement Specialties, Hampton, Manual.

[38] S. R. Habibi and A. Goldenberg, "Design of a New High-Performance Electrohydrostatic Actuator," *IEEE/ASME Transactions on Mechatronics*, vol. 5, no. 2, pp. 158-164, June 2000.

[39] HydraForce, "Proportional Valve Controller -DIN Coil Mount-," HydraForce, Lincolnshire, Manual 2011. [Online]. http://www.hydraforce.com/electro/Elec-pdf/3-422-1.pdf

[40] Walter Igers and Thomas Papatheodorou, "Fluid-power efficiency on the rise," *Machine Design*, vol. 82, no. 20, pp. 42-45, Nov. 2010.

[41] Xuan Bo Tran, Nur Hafizah, and Hideki Yanada, "Modeling of dynamic friction behaviors of hydraulic cylinders," *Mechatronics*, vol. 22, no. 1, pp. 65-75, February 2012.

[42] L. Ljung, *System Identification: Wiley Encyclopedia of Electrical and Electronics Engineering*. New York, U.S.A.: Wiley & Sons, Inc., 1999.

[43] W. Borutzky, B. Barnard, and J. Thoma, "An orifice flow model for laminar and turbulent conditions," *Simulation modeling practice and theory*, vol. 10, no. 3-4, pp. 141-152, Novermber 2002.

[44] Saeid Habibi, "Lecture 6, System Identification Part 1," McMaster University, Hamilton, Lecture 2010.

[45] Saeid Habibi, "Lecture 7, System Identification Part 2," McMaster

University, Hamilton, Lecture 2010.

[46] R. K. Mehra, "On the Identification of Variances and Adaptive Kalman Filtering," *IEEE Transactions on Automatic Control*, vol. AC-15, no. 2, pp. 175-184, Apirl 1970.

[47] R. T. Morein and P. Kalata, "A Polynomial Algorithm for Noise Identification in Linear System," in *5th IEEE International Symposium on Intelligent Control*, 1990, pp. 595-600.

[48] J. Dunik and M. Simandl, "Estimation of State and Measurement Noise Covariance Matrices by Multi-Step Prediction," in *17th World Congress, International Federation of Automatic Control*, Seoul, Korea, 2008, pp. 3689-3694.

[49] S. R. Habibi, "System Identification: Part 1," McMaster University, Hamilton, Ontario, Graduate Mechatronics Course Lecture 2010.

[50] HydraForce, "SP08-25, Spool, 2-Way, Normally Open," HydraForce, Lincolnshire, Manual 2011. [Online]. http://www.hydraforce.com/proport/Prop-pdf/2-028-1.pdf

[51] "Chapter 6 - Flight Control System," Politecnico Di Milano - Dipartmento Ingegneria Aerospaziale, Milan, Lecture 2004.

[52] Federal Aviation Administration. (2012, January) Japan Airline Flight 123, Boeing 747-SR100, JA8119. [Online]. http://accidents-ll.faa.gov/ll_main.cfm?TabID=2&LifeCycleID=3&LLID=16